Controls of Foreland-Deformation Patterns in the Orogen-Foreland Shortening System

---

Univerrsität - Dissertation

zur Erlangung des akademischen Grades
"doctor rerum naturalium"
(Dr. rer. nat.)
in der Wissenschaftsdisziplin "Geophysik"

eingereicht an der
Mathematisch-Naturwissenschaftlichen Fakultät
Institut für Geowissenschaften
der Universität Potsdam
und
außeruniversitäres Institut GFZ Geoforschungszentrum

von

Sibiao Liu

Potsdam, 01. Oktober 2019

Erstbetreuer: Prof. Dr. Stephan V. Sobolev

Zweitbetreuer: apl. Prof. Dr. Frank Krüger

Mentor: Dr. Andrey Y. Babeyko

Gutachter: Prof. Dr. Boris Kaus
Prof. Dr. Laura Giambiagi

Published online at the
Institutional Repository of the University of Potsdam:
https://doi.org/10.25932/publishup-44573
https://nbn-resolving.org/urn:nbn:de:kobv:517-opus4-445730

Abstract

Mountains contain all fantastic natural scenery on the surface of the Earth. The mountain-building process, known as orogenesis, is driven by plate tectonics. An outstanding example is the Andes in South America, characterized by significant differences between the central part and the rest. The Altiplano-Puna plateau, the second-highest plateau on our planet, exists in the Central Andes. This plateau exhibits a pronounced North-South segmentation in the style and magnitude of deformation. In the northern Altiplano segment, there is more than 300 km of tectonic shortening which started during the Eocene. A full thin-skinned thrust wedge located in the eastern flank of the plateau indicates simple-shear shortening mode. In contrast, the southern Puna undergoes approximate half shortening of the Altiplano - and the shortening started later. The tectonic style in the Puna foreland switches to the thick-skinned, which is an expression of pure-shear shortening. Previous studies suggest an intimate connection between this deformation diversity and the lithospheric structure. However, how to quantify this relationship and what controls the foreland-deformation patterns is not yet well understood.

In this work carried out in the framework of STRATEGY project, high-resolution 2D and 3D thermomechanical models are developed that systematically investigate controls of the orogen-foreland deformation patterns in general. The models are then applied to study the evolution of foreland deformation and surface topography in the Altiplano-Puna plateau.

Generic orogen-foreland shortening models demonstrated that three factors control the foreland-deformation patterns: (i) strength difference in the upper lithosphere between orogen and its foreland, rather than strength difference in the entire lithosphere; (ii) orogenic gravitational potential energy (GPE) controlled by its crustal thickness and lithospheric thickness, and (iii) the strength and thickness of foreland sediments. Pure-shear shortening occurs when the upper lithospheric strength of the orogen is higher or similar to that of the foreland and the orogenic crust is not much thicker than the foreland crust (relatively low GPE of the orogen). Simple-shear occurs if the orogen has a much thicker crust (a high GPE) and is thus significantly weaker than the foreland. A fully thick-skinned structure forms in the pure-shear deformation mode while the fully thin-skinned or thin- & thick-skinned mixed structures can develop in foreland if thick and mechanically weak sediments are present in the simple-shear shortening foreland. In addition, these models successfully reproduce realistic foreland-deformation types in the Central Andes, the Laramide province, and the Canadian Cordillera.

Regarding the Altiplano-Puna plateau case, more constraints (magnitude of shortening, subduction-induced mantle flow, and surface topography) are applied to geodynamic models. 2D model results reproduce foreland deformation and demonstrate first-order fit of surface topography in both segments of the plateau. Modeling suggests that before the start of 120 km shortening (at ca. 10 Ma), the plateau crust in the Altiplano segment underlain by a thin mantle lithosphere lid was much thicker and moderately denser than the foreland crust overlain by thick, mechanically weak Paleozoic sediments. In contrast, the Puna segment contained a thick plateau crust but thinner than the Altiplano crust and has no plateau lithospheric lid or no weak foreland sediments. The subduction-induced mantle flow below plateau controls the fault-dipping direction on the western edge of the Puna foreland. The modeled basal shear zone at a depth of ~45 km coincides with the observed seismogenic depth zone in NW Argentina broken foreland. The 3D models of the Altiplano-Puna plateau and its foreland including model using data-derived lithospheric structures performed in cooperation with another STRATEGY project, reproduce similar features as high-resolution 2D models. The models suggest that higher shortening rate at the Altiplano foreland is related to the mechanically easier simple-shear shortening in presence of thick and mechanically weak sediments. Lower shortening rate in the Puna foreland is likely accommodated in the forearc by the slab retreat.

Zusammenfasung

Gebirge sind ausgezeichnete Zeugen vergangener und aktiver Deformations- und Erosionsprozesse. Der Gebirgsbildungsprozess, auch als Orogenese bezeichnet, kann erfolgreich mit dem plattentektonischen Paradigma erklärt werden und umfasst sogenannte kollisionale und nicht-kollisionale Gebirge, die entweder an Subduktionszonen oder an kontinentalen Kollisionszonen gebildet werden. Eine Typlokalität känozoischer, nicht-kollisionaler Gebirgsbildung sind die Anden in Südamerika, eine bedeutende orografische Barriere mit einer Länge von etwa 7000 km, hoher Topographie, einer Rinne mit mehreren Kilometern Tiefe und schließlich undeformierte und deformierte Vorlandregionen. Die Anden zeichnen sich durch eine strukturelle und topographische Besonderheit aus, denn in den Zentralanden erstreckt sich das durchschnittlich 3.7-km-hohe Anden-Plateau (Altiplano-Puna) von Peru über Bolivien bis nach Nordwest-Argentinien - nach Tibet ist dies das zweithöchste Plateau der Erde. Dieses Plateau weist eine ausgeprägte Differenzierung in Nord-Süd-Richtung auf, vor allem hinsichtlich des Stils und des Ausmaßes der Verformung. Im nördlichen Altiplano-Segment gibt es Hinweise auf mehr als 300 km tektonische Verkürzung, die bereits im Eozän begann. An der Ostflanke des Plateaus befindet sich ein sedimentärer Schubkeil, der den subandinen Vorland-Überschiebungsgürtel, die Sierras Subandinas, umfasst. Dies deutet auf einen „Simple shear"-Modus hin. Im Gegensatz dazu weist das südliche Anden-Plateau (Puna) nur die Hälfte der im Norden beobachteten Verkürzungswerte auf, und die Verkürzung beginnt offenbar später. Im Gegensatz zum subandinen Überschiebungsgürtel weist auch die Vorlandregion einen komplett unterschiedlichen Deformationsstil auf, der durch die räumlich und zeitlich disparate Heraushebung von Kristallinblöcken gekennzeichnet ist. Frühere Studien legen einen engen Zusammenhang zwischen dieser Art der Verformung und der Lithosphärenstruktur nahe. Wie man diese Beziehung quantifiziert und welche Prozesse letztlich die Vorland-Deformationsmuster steuern, ist jedoch noch nicht ausreichend bekannt.

Aufgrund dieser Ausgangslage zum Verständnis orogener Prozesse benutze ich in dieser Studie hochauflösende thermomechanische 2D- und 3D-Modelle, die systematisch die Kontrolle der Deformationsmuster im Vorland des Orogens untersuchen und modellhaft wiedergeben. Die Modelle werden insbesondere angewendet, um die Entwicklung der Vorlanddeformation und der Topographie im Altiplano-Puna-Plateau sowie in den angrenzenden Gebieten zu untersuchen.

Generische Modelle zur Verkürzung des Orogens zeigen, dass vor allem drei Faktoren die Deformationsmuster des Vorlands steuern: (i) Unterschiede in der Festigkeit in der oberen Lithosphäre zwischen Orogen und dem Vorland und nicht Festigkeit in der gesamten Lithosphäre; (ii) die gravitationsbezogene potentielle Energie (GPE) des Orogens, die durch die Krusten- und Lithosphärenmächtigkeit gesteuert wird; und (iii) die mechanischen Eigenschaften und Mächtigkeiten von Vorlandsedimenten. „Pure-Shear"-Verkürzung (reine Scherung) tritt dann auf, wenn die Mächtigkeit der oberen Lithosphäre des Orogens größer ist als die der Vorlandregion (d.h. relativ niedrige GPE des Orogens). „Simple-shear"-Einengung (einfache Scherung) tritt auf, wenn das Orogen eine mächtigere Kruste (hohe GPE) als das Vorland besitzt. Ein kristallininvolviertes zerbrochenes Vorland (thick-skinned) entwickelt sich dabei als Folge von „pure-shear"-Deformation, während sich Vorland-Überschiebungsgürtel oder im Übergangsbereich zum zerbrochenen Vorland Mischstrukturen durch „simple-shear"-Prozesse bilden; Voraussetzung ist aber, dass entsprechende Sedimentmächtigkeiten in den Vorlandregionen existieren. Interessanterweise reproduzieren diese Modelle erfolgreich realistische Vorlandverformungstypen der Zentralanden, der Laramiden von Nordamerika oder die der kanadischen Kordillere.

Hinsichtlich des Altiplano-Puna-Plateaus gelten für geodynamische Modelle mehr Einschränkungen (z.B. Größenordnung der Verkürzung, subduktionsinduzierte Mantelströmung und Oberflächentopographie). 2D-Modellergebnisse reproduzieren die Vorland-Deformation sehr gut und zeigen eine Anpassung erster Ordnung hinsichtlich der Oberflächentopographie beider Plateauregionen. Die Modellierung deutet darauf hin, dass die Plateaukruste im Altiplano-Segment, die von einer dünnen Mantellithosphäre (mantle lid) unterlagert wird, vor dem Beginn der 120 km betragenden Verkürzung vor etwa 10 Millionen Jahren viel mächtiger und geringfügig dichter war als die Vorlandkruste. Im Gegensatz dazu war das Puna-Segment durch eine geringere Krustenmächtigkeit verglichen mit der Kruste des Altiplano charakterisiert; diese Region weist allerdings auch keinen sogenannten „mantle lid" sowie keine mechanisch schwachen Vorlandsedimente auf. Die subduktionsinduzierte Mantelströmung unterhalb des Plateaus steuert die Einfallsrichtung von Störungssystemen am westlichen Rand des Puna-Vorlandes. Eine modellierte basale Scherzone in etwa 45 km Tiefe fällt mit der beobachteten seismogenen Zone im nordwestargentinischen Vorland zusammen. Die 3D-Modelle des Altiplano-Puna-Plateaus und seines Vorlandes, einschließlich eines aus verschiedenen Datensätzen im StRATEGy-Projekt generierten Lithosphärenmodells, reproduzieren ähnliche Merkmale wie hochauflösende 2D-Modelle. Die Modelle deuten allesamt auf eine höhere Verkürzungsrate im Altiplano-Vorland hin, die durch „Simple-shear"-

Deformationsprozesse in Regionen mit mächtigen Sedimentbecken erreicht werden. Die geringeren Verkürzungsbeträge im Puna-Vorland werden dagegen wahrscheinlich durch das Zurückweichen der Subduktionszone im Forearc-Bereich ausgeglichen.

Table of Contents

1. Introduction 8

1.1 Orogen-foreland system 8

1.2 Orogenic foreland deformation patterns 9

1.3 Central Andean foreland deformation 12

1.4 Open questions in understanding the orogen-foreland shortening system 15

1.5 Thesis objectives 16

1.6 Thesis structure 17

References 19

2. Methodology 26

2.1 Modeling approach 26

2.2 Governing equations in computational geodynamics 31

2.3 Constitutive laws in computational geodynamics 32

2.4 Scalability test 36

2.5 Brittle thrust wedges benchmark 39

References 43

3. Controls of foreland-deformation patterns in the orogen-foreland shortening system: Insights from high-resolution numerical models 47

Abstract 47

3.1 Introduction 48

3.2 Numerical model description 50

3.2.1 Method and model geometry 50

3.2.2 Material properties and boundary conditions 52

3.3 Model results 54

3.3.1 Reference model 54

3.3.2 Variations in orogenic and foreland lithospheric structures 56

3.4 Discussion 60

3.4.1 Lithospheric strength analysis 60

3.4.2 Structural controls on the shortening mode and the deformation structure in the foreland 63

3.4.3 Applications to natural orogen-foreland systems 64
3.5 Conclusions 69
Appendix A: Geodynamic governing equations and yield strength envelope 70
References 73

4. Applying constraints of surface topography, shortening magnitude and mantle flow under the plateau on geodynamic simulations of the foreland deformation in the Altiplano-Puna plateau 81

Abstract 81
4.1 Introduction 83
4.2 Numerical model description 91
4.2.1 Model geometry 91
4.2.2 Material properties and boundary conditions 92
4.3 Numerical results 94
4.3.1 Reference model 94
4.3.2 The effect of mantle flow on the foreland deformation 96
4.3.3 Preferred model for the Altiplano plateau foreland system 99
4.3.4 Preferred model for the Puna plateau foreland system 100
4.4 Discussion and conclusions 102
4.4.1 Summary of model results 102
4.4.2 Fitting of deformation patterns together with surface topography in the Altiplano-Puna plateau and its foreland 104
References 106

5. Cenozoic foreland-deformation diversity in the Altiplano-Puna plateau: Insights from 3D geodynamic modeling of the plateau-foreland shortening system 113

Abstract 113
5.1 Introduction 114
5.2 Model description 114
5.2.1 Model approach and setup 114
5.2.2 Material properties and boundary conditions 115
5.3 Results 117
5.3.1 Same amounts of shortening on segments of the Altiplano and the Puna 118
5.3.2 Different amounts of shortening on segments of the Altiplano and the Puna 120

5.4 Discussion 123
5.5 Conclusions 125
References 126

6. 3D data-derived lithospheric structure of the Central Andes and its implications for deformation: Insights from gravity and geodynamic modeling 130
Abstract 130
6.1 Introduction 131
6.2 Geodynamic model description 132
6.3 Results 135
6.3.1 Gravity-constrained model 135
6.3.2 Geodynamic modeling 135
6.4 Discussion 138
6.5 Conclusions 139
References 140

7. Conclusions and future work 143
7.1 Conclusions 143
7.2 Future work 144
7.2.1 Influence of sediment stratification on the foreland deformation of the Altiplano-Puna plateau 144
7.2.2 Orogen-foreland shortening models with western subduction dynamics in the Central Andes 145
7.2.3 Surface processes and phase transition in the geodynamic simulation 146
7.2.4 Data assimilation function in the geodynamic simulation 147
References 148

List of Figures

1.1 The 3D cartoon of the orogen-foreland system with subduction processes..…….……9
1.2 Cartoons showing the deformation patterns.....….....……..……...10
1.3 Global distribution of some orogenic belts with foreland deformation structures…….11
1.4 Schematic diagrams of four different deformation patterns……...12
1.5 Evolution map of the Central Andes with the foreland deformation patterns in the Altiplano-Puna plateau……...14

2.1 Numerical libraries of PETSc (from PETSc manual)……...…….27
2.2 The fully-staggered finite-difference grid layout.……...……28
2.3 A numerical model example by using the ASPECT code (from Gassmöller et al., 2016).……...…….…….……..……...……...……30
2.4 The logarithm of effective non-linear viscosity (eta) for the dry olivine on the differential stress-temperature map (from Popov and Sobolev, 2008)……..34
2.5 A sketch of lithospheric structure from top sedimentary layer to bottom lithospheric mantle.……...……...……...……...……36
2.6 Scaling performances of LaMEM and ASPECT on HLRN....……...……38
2.7 The numerical model of a stable sand wedge.……...…….41
2.8 The numerical model of an unstable subcritical wedge.……...……..42

3.1 Initial model geometry with thermal-mechanical boundary conditions…….51
3.2 Reference model M1……...……...……...……54
3.3 Model behaviors for variations in crustal thickness, lithospheric thickness, sediment thickness and sediment friction coefficient.……...……..……...55
3.4 Foreland deformation patterns in Models M2-M13 with different individual factor after 100 km shortening……...……...……...57
3.5 Foreland deformation patterns in Models M14-M23 with the combination of multiple factors…….....60
3.6 Foreland deformation patterns with or without weak foreland sediments……...62
3.7 Numerical models with application to the case of the Central Andes……..……65
3.8 Numerical models with application to the case of the southern Canadian Rocky Mountains……...…...……...……..67

A.1 The list of strength profiles with different initial lithospheric structures (60-200 km) and crustal structures (36km, 50 km, 60 km).……..……..72

4.1 Schematic map of South America (from Stern, 2004).……..……84
4.2 Surface topography of the Altiplano-Puna plateau-foreland system.……..……..87
4.3 Present-day topography, thickness of the crust, thickness of the sedimentary layer in the Central Andes.……..……..……..……..……89
4.4 Initial model setup, including forelands of the Altiplano plateau and the Puna plateau….94
4.5 Reference model R1…….……..……..……..….95
4.6 Surface topography of the reference model R1 after 100 km shortening.……96
4.7 A numerical example showing the effect of mantle flow on the foreland shortening mode..……..……..……..……97
4.8 The effect of mantle flow on the foreland deformation pattern in the Puna case.……98
4.9 Altiplano plateau-foreland model after 120 km shortening.……..……99
4.10 Modeled surface topography of the Altiplano plateau and its foreland after 120 km shortening.……..……..……..……100
4.11 Puna plateau-foreland model after 60 km shortening.……..…….101
4.12 Modeled surface topography of the Puna plateau and its foreland after 60 km shortening.……..……..……..……102

5.1 Initial 3D model setup applied to the Altiplano-Puna case.……..……...115
5.2 Initial temperature field and viscosity field of each phase's lithosphere applied to the 3D Altiplano-Puna case.……..……..……..……117
5.3 3D numerical model of the Altiplano-Puna plateau-foreland system after 200 km shortening.……..……..……..……119
5.4 Three cross-sections of model deformation in Figure 5.3……120
5.5 3D numerical model of the Altiplano-Puna plateau-foreland system with different shortening magnitudes at the Altiplano and Puna sections.…….……122
5.6 The external driving force necessary to drive shortening at a constant bulk rate in the model S1……..……..……..……....124

6.1 Elevation map of South America showing the location of the gravity modeling region and the geodynamic modeling region.……..……..……...131

6.2 Initial setup of the 3D data-derived geodynamic model. …….....…….133
6.3 Cross-sections of the model, locations are depicted in Figure 1. ……...…….136
6.4 Deformation (i.e., the 2nd invariant of the strain rate) field of the geodynamic model after 3.3 km shortening…….……137

7.1 A 2D numerical model including the plateau-foreland shortening system and western oceanic plate subduction process after 3.5 Myr.……...……...……....146

List of Tables

3.1 Material properties in the numerical models..……...……..……....53

4.1 List of models showing parameter variations tested in this section…….….103

5.1 Material properties in the 3D numerical models……..……...…...……116

6.1 Thermo-mechanical properties used in the geodynamic model……....134

Chapter 1

Introduction

"Mountains are the beginning and the end of all natural scenery."

John Ruskin

1.1 Orogen-foreland system

Orogenesis, also known as the mountain-building process, creates numerous fantastic mountain ranges on Earth, and is one of the most prominent features of modern plate tectonics. This process is driven by convergent (subduction) plate boundaries or continental collision (Dewey & Bird, 1970; Condie, 1997), where horizontal forces make horizontal crustal shortening and vertical crustal thickening of the continental plate. Isostatic compensation of the thickened crust then uplifts the plate and forms the orogenic belt.

From the plate tectonics perspective, one tectonic environment that provides the driving force is the continental margin arc-trench system. In this system, an oceanic plate at the convergent margin subducts into the deep mantle below the overriding continental plate, under certain conditions resulting in shortening of the upper plate and thus the formation of an orogenic belt (Figure 1.1). Such orogens may undergo deformation over a protracted period of time. The Andes in South America and the Western Cordillera in North America are classical orogens representing this tectonic type. Another convergent tectonic environment is continental collision that may be either of continent-arc or continent-continent type. In the continent-arc collision, the continental plate subducts below the oceanic plate with a volcanic arc. This collisional type occurs in Taiwan and at the north edge of Australia. At the destructive boundary of the continent-continent collision, two continental plates meet and then collide with each other. The best modern examples of the collisional orogen are the Himalayas in Asia and the Alps in Europe.

Most active orogenic belts are flanked by neighboring foreland basins, which are defined as the elongated trough located between the compressional orogen and the stable craton (Beaumont, 1981; Molnar & Lyon-Caen, 1988; DeCelles & Giles, 1996). These basins are the result of

geodynamic processes associated with adjacent orogenic belts. In the orogen-foreland system, the foreland lithosphere mechanically couples with the orogenic wedge, to form a series of intraplate compressional features, such as folding and faulting, associated with metamorphism, erosion, and sedimentation (e.g., Ziegler et al., 1995; Ziegler et al., 2002). Furthermore, the compressional intraplate deformation varies spatiotemporally due to strength variations of the lithosphere under the orogen and its foreland (Ziegler et al., 1995).

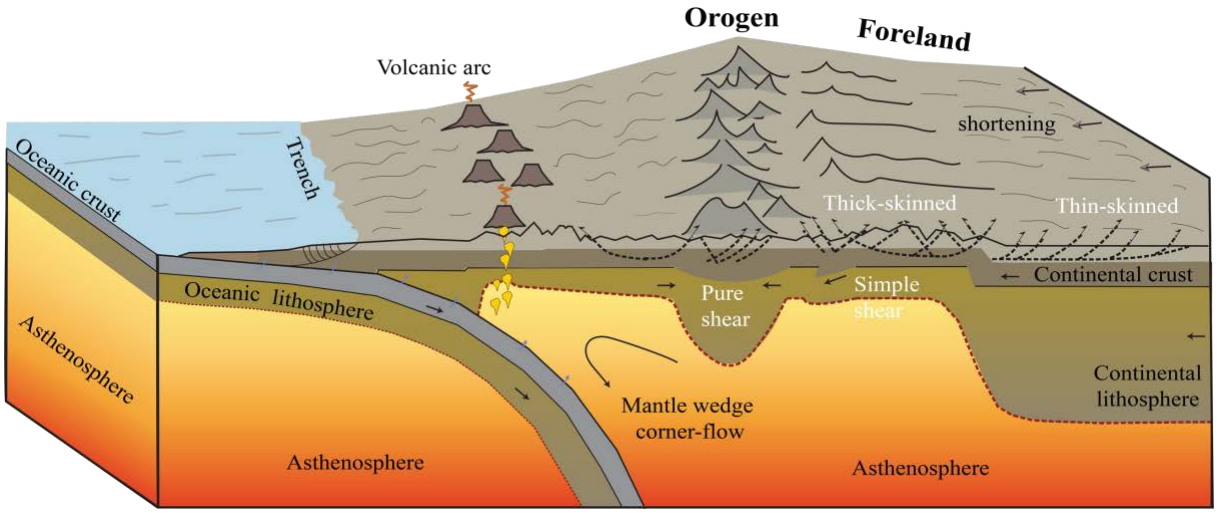

Figure 1.1. The 3D cartoon of the orogen-foreland system with subduction process. During shortening from the left side boundary, the system can undergo simple- or pure-shear shortening and form a thin- or thick-skinned structure.

1.2 Orogenic foreland deformation patterns

In contractional orogenic belts, plate compression between the orogen and its foreland can be divided into vertically distributed (pure-shear) and underthrusting (simple-shear) crustal strain styles. Pure-shear shortening is common in the intraplate collision, where the foreland plate squeezes horizontally towards the orogen, and the entire crustal shortening occurs in the vertical column of rocks (Figure 1.2a). The style of simple-shear shortening is characterized by the process of foreland underthrusting. As rocks in the foreland crust are destructed under shortening, a downward detachment fault is formed. The foreland crust underthrusts along the thrust fault and intrudes into the orogenic lithosphere (Figure 1.2c).

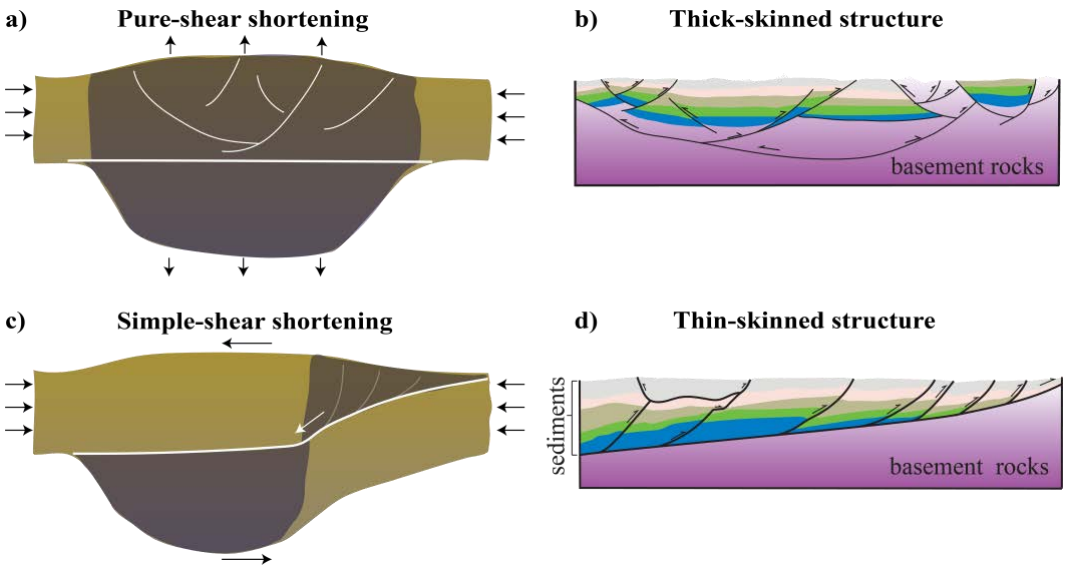

Figure 1.2. Cartoons showing the deformation patterns. **a)** is pure-shear shortening and **c)** is simple-shear shortening, modified from Allmendinger & Gubbels (1996). **b)** is thick-skinned tectonics and **d)** is thin-skinned tectonics.

In the orogen-foreland shortening system, the crustal-scale deformation in foreland fold-and-thrust belts (FTBs) commonly includes shallow thin-skinned and deep thick-skinned structures (Wiltschko & Dorr, 1983; Pfiffner, 2006). These two tectonic types are first described by the critically tapered wedge model (Davis et al., 1983; Dahlen, 1990). The thin-skinned tectonics is characterized by a deformed thrust zone in the sedimentary cover detached from the underlying undeformed basement along a shallow-dipping décollement (Figure 1.2d). This shallow structural style supposes a large-scale shortening and duplication of the sedimentary sequence. Conversely, typically a smaller amount of crustal shortening exists in the region where the crystalline basement is involved in the deformation (thick-skinned tectonic style; Figure 1.2b).

Figure 1.3 shows a global distribution of some well-known orogenic belts with different foreland deformation structures. Some, like the Pyrenees, the Atlas, the Puna segment of the Central Andes, and the Laramide province, exhibit a fully thick-skinned structural style (e.g., DeCelles, 2004; Harfi et al., 2006; Kay & Coira, 2009; Lagabrielle et al., 2010; Yonkee & Weil, 2015). A fully thin-skinned tectonics exits mainly in the Americas such as Central Appalachians, Sevier belt, Canadian Cordillera, and the Altiplano segment of the Andes (e.g., Gwinn, 1964; Price, 1981; Allmendinger & Gubbels, 1996; Kley, 1996; Yonkee & Weil, 2015). In natural orogen-foreland systems, the two structural styles are not mutually exclusive and may occur

coevally. Many foreland regions of orogenic belts, such as Alps, Himalayas, southern Central Andes, Taiwan, and Zagros, exhibit both thin- and thick-skinned structural patterns (e.g., Jordan & Allmendinger, 1986; Lacombe & Mouthereau, 2002; Frederic Mouthereau et al., 2002; Yin, 2006; Oveisi et al., 2009; Pfiffner, 2016, 2017).

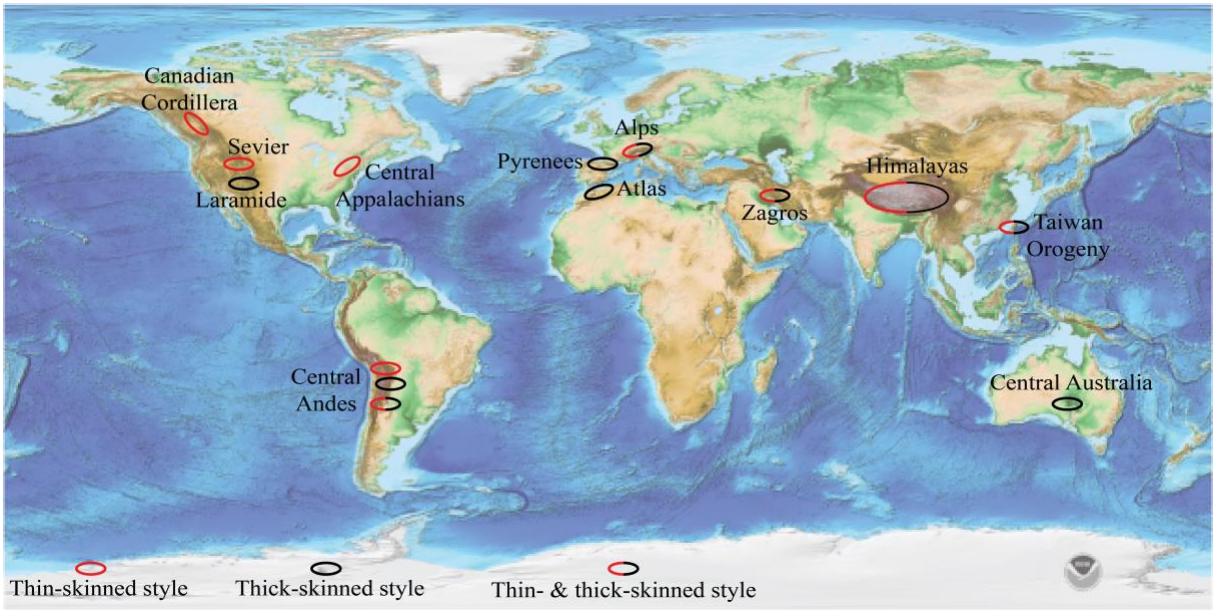

Figure 1.3. Global distribution of some orogenic belts with foreland deformation structures. Data sources: ETOPO1; Gwinn, 1964; Price, 1981; Teyssier, 1985; DeCelles et al., 2001; Mouthereau et al., 2002; Harfi et al., 2006; DeCelles, 2004; Yin, 2006; Kay & Coira, 2009; Oveisi et al., 2009; Lagabrielle et al., 2010; Pfiffner, 2016; Yonkee & Weil, 2015; Pfiffner, 2017.

In this study, we consider four groups of the deformation patterns (i.e., shortening modes and structural styles) (Figure 1.4) and more details are given in Chapter 3 below. The first one is the pattern of pure-shear shortening with fully thick-skinned tectonics, where both the sedimentary cover and underlying basement in the upper felsic crust are vertically shortened and deformed (Figure 1.4a). In another three deformation groups, the foreland crusts all underthrust below the orogenic crust (i.e., simple-shear), but the tectonic style is different. If the thin- and thick-skinned deformation take place coevally in the foreland, the deformation style can either be thick-skinned dominated or thin- & thick-skinned mixed. We consider the deformation to be thick-skinned dominated when the portion of thick-skinned shortening is more than 80-90% of total foreland shortening (e.g., compare the length of the solid line with the length of dashed line in Figure 1.4b). When more thin-skinned shortening (>10-20%) forms,

the tectonic style is defined as a mixture of thin- & thick-skinned tectonics (Figure 1.4c). Lastly, if the deformation is localized only in the sedimentary layer, then a fully thin-skinned thrust zone forms in the foreland (Figure 1.4d).

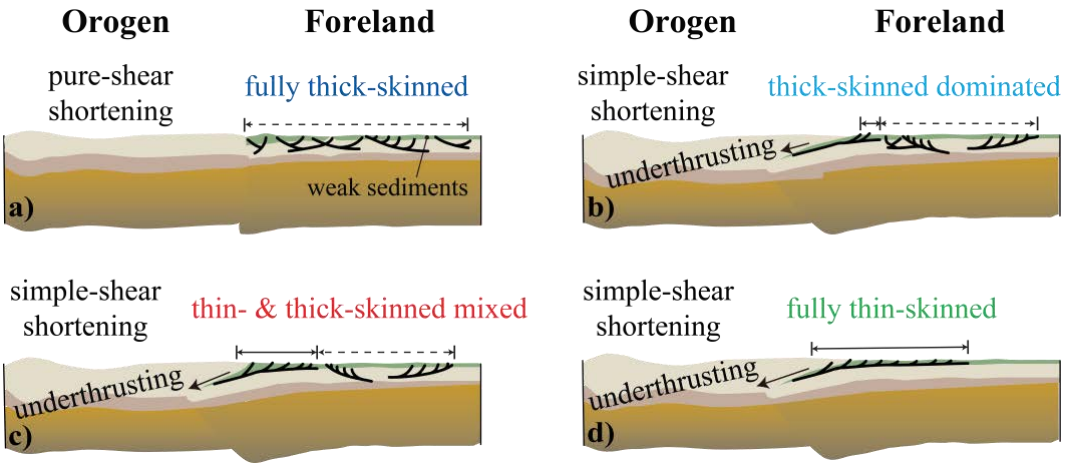

Figure 1.4. Schematic diagrams of four different deformation patterns: **a)** pure-shear shortening with fully thick-skinned structure, **b)** simple-shear shortening with thick-skinned dominated, **c)** thin- & thick-skinned mixed, and **d)** fully thin-skinned. The simple-shear mode is characterized by the foreland underthrusting process.

1.3 Central Andean foreland deformation

The Central Andes of western South America, known as the largest non-collisional continental orogeny around the globe, is an outstanding natural laboratory to study the orogen-foreland deformation system and understand the tectonic process behind. It is strikingly different from the Northern and Southern Andes. For instance, a large amount of shortening (more than 300 km) during the late Cenozoic is accommodated in the Central Andes (Figure 4.3 in Chapter 4; Horton, 2018), which resulted in an unusually thick felsic crust under the plateau (Isacks, 1988; Allmendinger et al., 1997; Kley et al., 1999; Beck & Zandt, 2002; Yuan et al., 2002). By contrast, the magnitude of shortening is much less in the Northern and Southern Andes (Kley & Monaldi, 1998; Horton, 2018). The tectonic shortening also started much later in the Southern Andes than in the Central Andes (Vietor & Echtler, 2006).

Another dramatic feature of the Central Andes is the existence of the second-highest plateau (after Tibet) in the world with an average elevation of ~4 km. The plateau developed along more than 15,000 km length of the convergent continental margin during continuous subduction

of the Nazca plate below the South America plate. In the entire Andes, this is the only plateau of such height. In addition to this first-order difference between central and side parts of the Andes, the plateau can be divided into the Altiplano segment of Peru and Bolivia in the north and the Argentine Puna in the south (Figure 1.5). The two segments differ in topography, magmatism, and lithospheric structure, as well as in the conditions of continental plateau formation (Allmendinger & Gubbels, 1996; Allmendinger et al., 1997).

The degrees and styles of deformation in the foreland FTBs of the two plateau segments exhibit a notable along-strike variation (Figure 1.5). These belts were well-developed by the late Neogene, where the deformation migrated from the western Central Andes toward its eastern side foreland (e.g., Kley & Monaldi, 1998). North of 23-24°S, in the Altiplano segment of the Central Andes, the tectonic shortening started during the Eocene; its accumulated magnitude is more than 300 km (Figure 4.3 in Chapter 4; Oncken et al., 2006; Horton, 2018). About 40% of this shortening took place in the last 10 Ma when the foreland started to deform. In contrast, the southern Puna segment underwent approximately half of the Altiplano shortening and the shortening started later. A ~250-km-wide zone of fully thick-skinned thrust exists in the eastern foreland of the Altiplano Plateau and the East Cordillera, which is an expression of simple-shear shortening. This tectonic style changes to the thick-skinned tectonics in the Santa Barbara System indicating the pure-shear mode (Figure 1.5).

The process of pure- or simple-shear shortening and the way thin-skinned and thick-skinned related structures interact are not yet well understood. Previous studies suggest an intimate connection between the diversity of foreland-deformation and both shallow and deep lithospheric structures and processes (e.g., Allmendinger & Gubbels, 1996; Babeyko et al., 2006; Pfiffner, 2006). For example, the along-strike differentiation of foreland-deformation coincides with the strength variation of the orogenic lithosphere and of the foreland lithosphere in the two plateau segments of the Central Andes (Allmendinger & Gubbels, 1996; Kley et al., 1999; Whitman et al., 1996). The exceptional thick felsic crust under the plateau possibly contributes to the foreland-deformation diversity (e.g., Beck et al., 1996; Yuan et al., 2000; Beck & Zandt, 2002; Schurr et al., 2006).

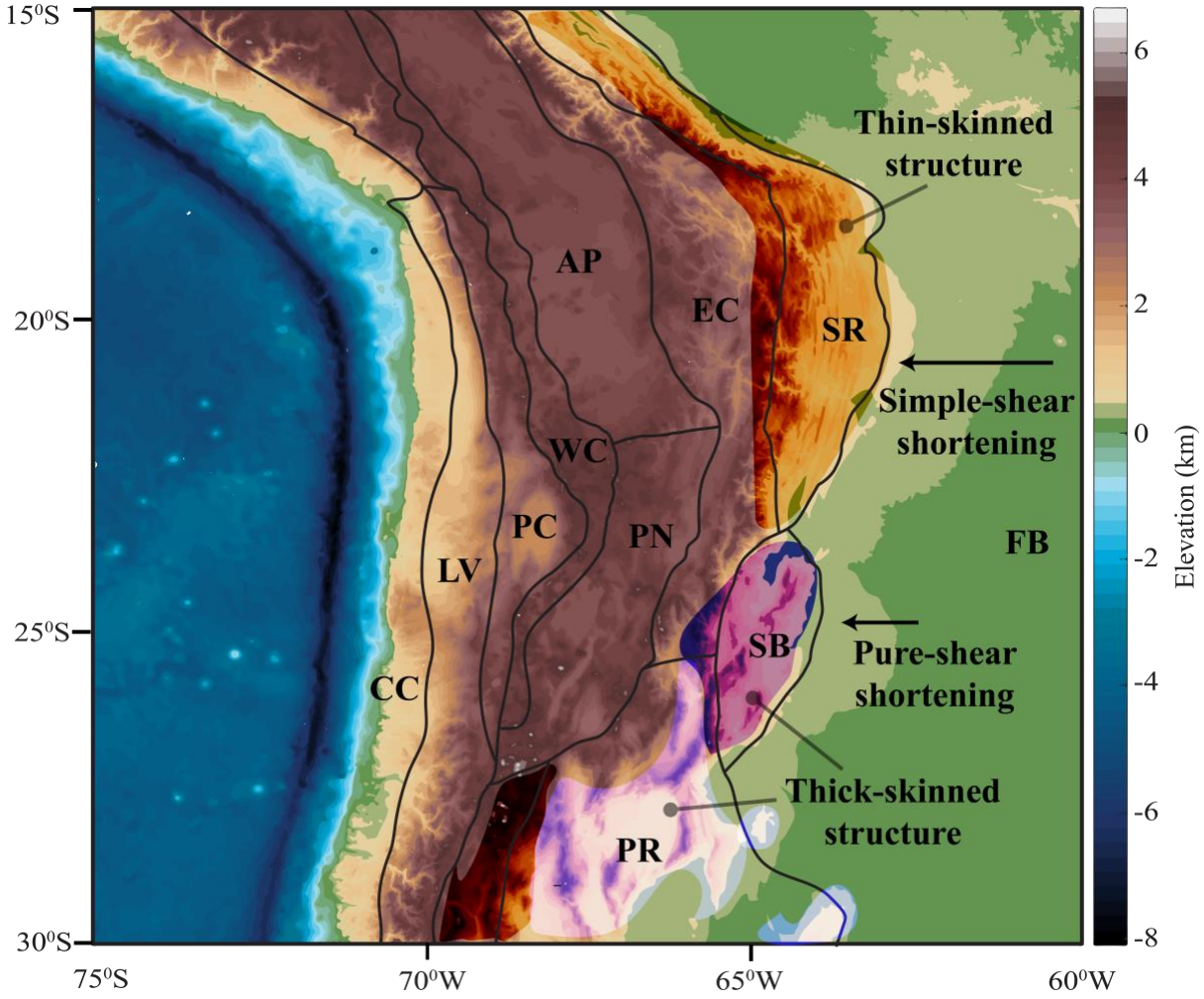

Figure 1.5. Evolution map of the Central Andes with the foreland deformation patterns (thin- or thick-skinned structure and simple- or pure-shear shortening) in the Altiplano-Puna plateau. The different morphotectonic units are modified from Jordan et al. (1983) and Ibarra et al. (2019). CC: Coastal Cordillera; LV: Longitudinal Valley; PC: Chilean Precordillera; WC: Western Cordillera; AP: Altiplano; PN: Puna; EC: Eastern Cordillera; SR: Subandean Ranges; SB: Santa Barbara System; PR: Pampean Ranges; FB: Chaco-Paran. Foreland basin. The foreland structural modes are modified from Kay & Coira (2009).

Allmendinger & Gubbels (1996) also noticed the N-S depletion of the Paleozoic sedimentary basins and Pearson et al. (2013) discussed the different spatial distribution of Mesozoic rift basins in the foreland, both of which implied a possible correlation between the distribution of pre-Cenozoic sediments and the deformation patterns. Babeyko & Sobolev (2005) and Babeyko et al (2006) demonstrated that a drop in the mechanical strength of the foreland sediments east of the Altiplano plateau may results in the switch from pure- to simple-shear mode and the formation of the Subandean FTBs. In short, the inherited lithospheric strengths (e.g.,

Allmendinger & Gubbels, 1996; Mouthereau et al., 2013) and pre-orogenic upper-crustal architecture (e.g., Allmendinger & Gubbels, 1996; Babeyko & Sobolev, 2005; Pearson et al., 2013) possibly control the along-strike segmentation of the Central Andean foreland.

The suggested hypotheses reflect the complexity of the deformation processes in the orogen-foreland shortening system. Large-scale numerical thermomechanical modeling provides a valuable tool for testing such hypotheses and quantifying the tectonic processes by applying continuum mechanics to evaluate force balance, mass transport, and heat transfer in the orogens and their forelands (e.g., Babeyko & Sobolev, 2005; Beaumont et al., 2006; Gerya & Stöckhert, 2006; Jammes & Huismans, 2012). Constrained by numerous geological, geophysical, and geochemical observations, the geodynamic models can be applied to the temporal correlation between tectonic shortening and processes that possibly contribute to the deformation of the orogen-foreland system.

1.4 Open questions in understanding the orogen-foreland shortening system

Understanding orogenic processes associated with plate tectonics and the deformation of the orogen-foreland system has been one of the long-term goals for the solid earth scientific community. In this study, high-resolution 2D and 3D numerical models are developed to quantitatively explore 1) the nature of lithospheric strength change and sediment weakening in the foreland, and 2) how the foreland deformation evolves due to the variation of strength in both the orogen and its foreland. In particular, specific research and technique problems concerning the numerical study of the orogen-foreland system remain:

- **No generic orogen-foreland shortening model.** To this date, there are no generic numerical models of the orogen-foreland shortening system that systematically study and quantify the relationship between lithospheric strength and foreland-deformation patterns. Previous models mainly focus on either a specific natural case (e.g., Babeyko & Sobolev, 2005; Nilfouroushan et al., 2013) or only internal crustal strength change (e.g., Jammes & Huismans, 2012). Since the lithospheric strength is different from one orogen to another, it is worth exploring how the strength variation controls foreland-deformation patterns through numerical modeling of a generic orogen-foreland system.

- **Low model resolution.** Current thermomechanical models of foreland deformation (e.g. Babeyko et al., 2006) have relatively low resolution (grid size of more than 1 km in the upper crust). However, the sedimentary cover is more than ten times thinner than the underlying lithosphere (e.g., Laske et al., 2013). Therefore, it is necessary to increase the model resolution to ensure the track of deformation in the sedimentary layer. Recent progress in numerical modeling process allows for an extension of this research by implementing not only higher-resolution 2D models but also 3D lithosphere-scale models.

- **More constraints on orogen-foreland models required.** Since orogenesis, such as that in the Andes, is strongly related to the subduction process, the effect of subduction dynamics on the tectonic shortening and deformation structures should also be involved in the orogen-foreland contractional models. In addition, what is the surface response (e.g., topography) of the shortening model and could the modeled surface feature fit observation of a natural orogen-foreland system?

- **3D aspects of the orogen-foreland system are poorly investigated.** What are the 3D behaviors of the orogen-foreland model during shortening, as many natural cases (e.g., Central Andes, Zagros) are 3D systems? For example, in the Central Andes, how could the foreland-deformation pattern longitudinally switch from simple-shear shortening with a thin-skinned thrust zone in the Altiplano foreland to pure-shear shortening accompanied by the thick-skinned structure?

1.5 Thesis objectives

The overall aim of this thesis is to explore what controls foreland-deformation patterns in the orogen-foreland shortening system. This thesis is motivated by the observed along-strike segmentation of foreland-deformation in an outstanding natural laboratory, which are the Central Andes in South America. A key question about Andean orogeny is why the foreland of the same plateau of the Central Andes deforms in different ways and intensities. The objectives are:

a) to systematically study controls of the deformation patterns in the orogenic foreland by creating generic orogen-foreland shortening models;

b) to investigate the foreland-deformation diversity, surface topography evolution, and mantle flow below the plateau by applying 2D and 3D geodynamic modeling of the Altiplano and Puna segments of the Central Andes;
c) to explore deformation of the orogen and its foreland by using a 3D data-derived lithospheric structure of the Central Andes.

1.6 Thesis structure

This thesis consists of introduction chapter (Chapter1), methodology chapter (Chapter 2), summary and outlook chapter (Chapter 7) and four main research chapters (Chapters 3-6) having their own abstract, introduction, methods, results, discussion, and conclusions sections. More details concerning Chapters 2-7 are presented below:

- **Chapter 2** reviews the methodology, including numerical modeling approach, governing equations, constitutive laws, the scaling test and benchmark of the two most advanced geodynamic codes LaMEM and ASPECT used in the thesis.

- **Chapter 3** investigates the relationship between the lithospheric structure of the orogen-foreland system and the foreland-deformation styles. In particular, high-resolution 2D generic orogen-foreland compressional models test the effects of different factors, such as crustal thickness, lithospheric thickness, and mechanical strength and thickness of foreland sediments, on foreland-deformation patterns. Model results are compared with four natural orogen-foreland examples in North America and South America. *This work is under revision in Tectonics as Liu, S., Sobolev, S.V., and Babeyko, A.Y. (2019), "Controls of the Foreland Deformation Pattern in Orogen-Foreland Shortening System: Constraints from High-Resolution Numerical Models".*

- **Chapter 4** focuses on the plateau-foreland shortening system of the Central Andes. Constraints of the surface topography, subduction-induced mantle flow under the plateau, and different magnitude of shortening are applied to high-resolution 2D models of both the Altiplano and Puna segments. Two preferred models for each segment, which best fit the observations of the tectonic patterns and surface elevation, are presented.

- **Chapter 5** extends the 2D numerical models of the shortening system in the Altiplano-Puna plateau developed in Chapters 3 and 4 to 3D. The 3D model aims to quantify the foreland deformation patterns in both the Altiplano plateau and the Puna plateau in one model and to explore the key factors controlling lateral N-S variation of deformation types.

- **Chapter 6** studies the deformation evolution in the Central Andes through the 3D data-derived geodynamic models, with the lithospheric structures of the plateau and its foreland derived from a new density model that integrates geological and geophysical data. *This work has been published as Ibarra, F., Liu, S., Meeßen, C., Prezzi, C. B., Bott, J., Scheck-Wenderoth, M., Sobolev, S., Strecker, M.R. (2019), "3D data-derived lithospheric structure of the Central Andes and its implications for deformation: insights from gravity and geodynamic modelling", Tectonophysics, 766, 453–468. https://doi.org/10.1016/j.tecto.2019.06.025.*

- **Chapter 7** summarizes the findings of the above chapters and provides suggestions for future work.

References

Allmendinger, R. W., & Gubbels, T. (1996). Pure and simple shear plateau uplift, Altiplano-Puna, Argentina and Bolivia. Tectonophysics, 259(1), 1–13. https://doi.org/10.1016/0040-1951(96)00024-8

Allmendinger, R. W., Teresa E. Jordan, Suzanne M. Kay, & Isacks, and B. L. (1997). The Evolution of the Altiplano-Puna plateau of the Central Andes. Annual Review of Earth and Planetary Sciences, 25(1), 139–174. https://doi.org/10.1146/annurev.earth.25.1.139

Babeyko, A. Y., & Sobolev, S. V. (2005). Quantifying different modes of the late Cenozoic shortening in the central Andes. Geology, 33(8), 621–624. https://doi.org/10.1130/G21126AR.1

Babeyko, A. Y., Sobolev, S. V., Vietor, T., Oncken, O., & Trumbull, R. B. (2006). Numerical Study of Weakening Processes in the Central Andean Back-Arc. In O. Oncken, G. Chong, G. Franz, P. Giese, H.-J. Götze, V. A. Ramos, et al. (Eds.), The Andes (pp. 495–512). Springer Berlin Heidelberg. Retrieved from http://link.springer.com/10.1007/978-3-540-48684-8_24

Beaumont, C., Nguyen, M. H., Jamieson, R. A., & Ellis, S. (2006). Crustal flow modes in large hot orogens. Geological Society, London, Special Publications, 268(1), 91–145. https://doi.org/10.1144/GSL.SP.2006.268.01.05

Beaumont, Christopher. (1981). Foreland basins. Geophysical Journal of the Royal Astronomical Society, 65(2), 291–329. https://doi.org/10.1111/j.1365-246X.1981.tb02715.x

Beck, S. L., & Zandt, G. (2002). The nature of orogenic crust in the central Andes: NATURE OF OROGENIC CRUST. Journal of Geophysical Research: Solid Earth, 107(B10), ESE 7-1-ESE 7-16. https://doi.org/10.1029/2000JB000124

Beck, S. L., Zandt, G., Myers, S. C., Wallace, T. C., Silver, P. G., & Drake, L. (1996). Crustal-thickness variations in the central Andes. Geology, 24(5), 407–410.

Condie, K. C. (1997). Plate Tectonics and Crustal Evolution. Elsevier. https://doi.org/10.1016/B978-0-7506-3386-4.X5000-9

Dahlen, F. A. (1990). Critical Taper Model of Fold-And-Thrust Belts and Accretionary Wedges. Annual Review of Earth and Planetary Sciences, 18(1), 55–99. https://doi.org/10.1146/annurev.ea.18.050190.000415

Davis, D., Suppe, J., & Dahlen, F. A. (1983). Mechanics of fold-and-thrust belts and accretionary wedges. Journal of Geophysical Research: Solid Earth, 88(B2), 1153–1172. https://doi.org/10.1029/JB088iB02p01153

DeCelles, P. G. (2004). Late Jurassic to Eocene evolution of the Cordilleran thrust belt and foreland basin system, western U.S.A. American Journal of Science, 304(2), 105–168. https://doi.org/10.2475/ajs.304.2.105

DeCelles, Peter G., & Giles, K. A. (1996). Foreland basin systems. Basin Research, 8(2), 105–123. https://doi.org/10.1046/j.1365-2117.1996.01491.x

DeCelles, Peter G., Robinson, D. M., Quade, J., Ojha, T. P., Garzione, C. N., Copeland, P., & Upreti, B. N. (2001). Stratigraphy, structure, and tectonic evolution of the Himalayan fold-thrust belt in western Nepal. Tectonics, 20(4), 487–509. https://doi.org/10.1029/2000TC001226

Dewey, J. F., & Bird, J. M. (1970). Mountain belts and the new global tectonics. Journal of Geophysical Research (1896-1977), 75(14), 2625–2647. https://doi.org/10.1029/JB075i014p02625

El Harfi, A., Guiraud, M., & Lang, J. (2006). Deep-rooted “thick skinned” model for the High Atlas Mountains (Morocco). Implications for the structural inheritance of the southern Tethys passive margin. Journal of Structural Geology, 28(11), 1958–1976. https://doi.org/10.1016/j.jsg.2006.08.011

Gerya, T., & Stöckhert, B. (2006). Two-dimensional numerical modeling of tectonic and metamorphic histories at active continental margins. International Journal of Earth Sciences, 95(2), 250–274. https://doi.org/10.1007/s00531-005-0035-9

Gwinn, V. E. (1964). Thin-Skinned Tectonics in the Plateau and Northwestern Valley and Ridge Provinces of the Central Appalachians. GSA Bulletin, 75(9), 863–900. https://doi.org/10.1130/0016-7606(1964)75[863:TTITPA]2.0.CO;2

Horton, B. K. (2018). Tectonic Regimes of the Central and Southern Andes: Responses to Variations in Plate Coupling During Subduction. Tectonics, 37(2), 402–429. https://doi.org/10.1002/2017TC004624

Ibarra, F., Liu, S., Meeßen, C., Prezzi, C. B., Bott, J., Scheck-Wenderoth, M., et al. (2019). 3D data-derived lithospheric structure of the Central Andes and its implications for deformation: Insights from gravity and geodynamic modelling. Tectonophysics, 766, 453–468. https://doi.org/10.1016/j.tecto.2019.06.025

Isacks, B. L. (1988). Uplift of the Central Andean Plateau and bending of the Bolivian Orocline. Journal of Geophysical Research: Solid Earth, 93(B4), 3211–3231. https://doi.org/10.1029/JB093iB04p03211

Jammes, S., & Huismans, R. S. (2012). Structural styles of mountain building: Controls of lithospheric rheologic stratification and extensional inheritance: CRUSTAL STRENGTH AND MOUNTAIN BUILDING. Journal of Geophysical Research: Solid Earth, 117(B10). https://doi.org/10.1029/2012JB009376

Jordan, T. E., & Allmendinger, R. W. (1986). The Sierras Pampeanas of Argentina; a modern analogue of Rocky Mountain foreland deformation. American Journal of Science, 286(10), 737–764. https://doi.org/10.2475/ajs.286.10.737

Jordan, T. E., Isacks, B. L., Allmendinger, R. W., Brewer, J. A., Ramos, V. A., & Ando, C. J. (1983). Andean tectonics related to geometry of subducted Nazca plate. GSA Bulletin, 94(3), 341–361. https://doi.org/10.1130/0016-7606(1983)94<341:ATRTGO>2.0.CO;2

Kay, S. M., & Coira, B. L. (2009). Shallowing and steepening subduction zones, continental lithospheric loss, magmatism, and crustal flow under the Central Andean Altiplano-Puna plateau. Geological Society of America Memoirs, 204, 229–259. https://doi.org/10.1130/2009.1204(11)

Kley, J., Monaldi, C. R., & Salfity, J. A. (1999). Along-strike segmentation of the Andean foreland: causes and consequences. Tectonophysics, 301(1–2), 75–94. https://doi.org/10.1016/S0040-1951(98)90223-2

Kley, Jonas. (1996). Transition from basement-involved to thin-skinned thrusting in the Cordillera Oriental of southern Bolivia. Tectonics, 15(4), 763–775. https://doi.org/10.1029/95TC03868

Kley, Jonas, & Monaldi, C. R. (1998). Tectonic shortening and crustal thickness in the Central Andes: How good is the correlation? Geology, 26(8), 723–726. https://doi.org/10.1130/0091-7613(1998)026<0723:TSACTI>2.3.CO;2

Lacombe, O., & Mouthereau, F. (2002). Basement-involved shortening and deep detachment tectonics in forelands of orogens: Insights from recent collision belts (Taiwan, Western Alps, Pyrenees). Tectonics, 21(4), 12–1. https://doi.org/10.1029/2001TC901018

Lagabrielle, Y., Labaume, P., & Blanquat, M. de S. (2010). Mantle exhumation, crustal denudation, and gravity tectonics during Cretaceous rifting in the Pyrenean realm (SW Europe): Insights from the geological setting of the lherzolite bodies. Tectonics, 29(4). https://doi.org/10.1029/2009TC002588

Laske, G., Masters, T. G., Ma, Z., & Pasyanos, M. E. (2013). Update on CRUST1.0: A 1-degree Global Model of Earth's Crust.

Molnar, P., & Lyon-Caen, H. (1988). Some simple physical aspects of the support, structure, and evolution of mountain belts. In Geological Society of America Special Papers (Vol. 218, pp. 179–208). Geological Society of America. https://doi.org/10.1130/SPE218-p179

Mouthereau, Frederic, DEFFONTAINES, B., Lacombe, O., & Angelier, J. (2002). Variations along the strike of the Taiwan thrust belt: Basement control on structural style, wedge geometry, and kinematics (Vol. 358). https://doi.org/10.1130/0-8137-2358-2.31

Mouthereau, Frédéric, Watts, A. B., & Burov, E. (2013). Structure of orogenic belts controlled by lithosphere age. Nature Geoscience, 6(9), 785–789. https://doi.org/10.1038/ngeo1902

Nilfouroushan, F., Pysklywec, R., Cruden, A., & Koyi, H. (2013). Thermal-mechanical modeling of salt-based mountain belts with pre-existing basement faults: Application to the Zagros fold and thrust belt, southwest Iran. Tectonics, 32(5), 1212–1226. https://doi.org/10.1002/tect.20075

Oncken, O., Hindle, D., Kley, J., Elger, K., Victor, P., & Schemmann, K. (2006). Deformation of the Central Andean Upper Plate System — Facts, Fiction, and Constraints for Plateau Models. In O. Oncken, G. Chong, G. Franz, P. Giese, H.-J. Götze, V. A. Ramos, et al. (Eds.), The Andes (pp. 3–27). Springer Berlin Heidelberg. https://doi.org/10.1007/978-3-540-48684-8_1

Oveisi, B., Lavé, J., Van Der Beek, P., Carcaillet, J., Benedetti, L., & Aubourg, C. (2009). Thick- and thin-skinned deformation rates in the central Zagros simple folded zone (Iran) indicated by displacement of geomorphic surfaces. Geophysical Journal International, 176(2), 627–654. https://doi.org/10.1111/j.1365-246X.2008.04002.x

Pearson, D. M., Kapp, P., DeCelles, P. G., Reiners, P. W., Gehrels, G. E., Ducea, M. N., & Pullen, A. (2013). Influence of pre-Andean crustal structure on Cenozoic thrust belt kinematics and shortening magnitude: Northwestern Argentina. Geosphere, 9(6), 1766–1782. https://doi.org/10.1130/GES00923.1

Pfiffner, O. A. (2006). Thick-skinned and thin-skinned styles of continental contraction. In Special Paper 414: Styles of Continental Contraction (Vol. 414, pp. 153–177). Geological Society of America. https://doi.org/10.1130/2006.2414(09)

Pfiffner, O. A. (2016). Basement-involved thin-skinned and thick-skinned tectonics in the Alps. Geological Magazine, 153(5–6), 1085–1109. https://doi.org/10.1017/S0016756815001090

Pfiffner, O. A. (2017). Thick-Skinned and Thin-Skinned Tectonics: A Global Perspective. Geosciences, 7(3), 71. https://doi.org/10.3390/geosciences7030071

Price, R. A. (1981). The Cordilleran foreland thrust and fold belt in the southern Canadian Rocky Mountains. Geological Society, London, Special Publications, 9(1), 427–448. https://doi.org/10.1144/GSL.SP.1981.009.01.39

Schurr, B., Rietbrock, A., Asch, G., Kind, R., & Oncken, O. (2006). Evidence for lithospheric detachment in the central Andes from local earthquake tomography. Tectonophysics, 415(1–4), 203–223. https://doi.org/10.1016/j.tecto.2005.12.007

Teyssier, C. (1985). A crustal thrust system in an intracratonic tectonic environment. Journal of Structural Geology, 7(6), 689–700. https://doi.org/10.1016/0191-8141(85)90144-0

Vietor, T., & Echtler, H. (2006). Episodic Neogene Southward Growth of the Andean Subduction Orogen between 30°S and 40°S — Plate Motions, Mantle Flow, Climate, and Upper-Plate Structure. In O. Oncken, G. Chong, G. Franz, P. Giese, H.-J. Götze, V. A. Ramos, et al. (Eds.), The Andes (pp. 375–400). Springer Berlin Heidelberg. https://doi.org/10.1007/978-3-540-48684-8_18

Whitman, D., Isacks, B. L., & Kay, S. M. (1996). Lithospheric structure and along-strike segmentation of the Central Andean Plateau: seismic Q, magmatism, flexure, topography and tectonics. Tectonophysics, 259(1–3), 29–40. https://doi.org/10.1016/0040-1951(95)00130-1

Wiltschko, D. V., & Dorr, J. A. (1983). Timing of Deformation in Overthrust Belt and Foreland of Idaho, Wyoming, and Utah. AAPG Bulletin, 67(8), 1304–1322.

Yin, A. (2006). Cenozoic tectonic evolution of the Himalayan orogen as constrained by along-strike variation of structural geometry, exhumation history, and foreland sedimentation. Earth-Science Reviews, 76(1), 1–131. https://doi.org/10.1016/j.earscirev.2005.05.004

Yonkee, W. A., & Weil, A. B. (2015). Tectonic evolution of the Sevier and Laramide belts within the North American Cordillera orogenic system. Earth-Science Reviews, 150, 531–593. https://doi.org/10.1016/j.earscirev.2015.08.001

Yuan, X., Sobolev, S. V., Kind, R., Oncken, O., Bock, G., Asch, G., et al. (2000). Subduction and collision processes in the Central Andes constrained by converted seismic phases. Nature, 408(6815), 958–961. https://doi.org/10.1038/35050073

Yuan, X., Sobolev, S. V., & Kind, R. (2002). Moho topography in the central Andes and its geodynamic implications. Earth and Planetary Science Letters, 199(3–4), 389–402. https://doi.org/10.1016/S0012-821X(02)00589-7

Ziegler, P.A., Berotti, G., & Cloetingh, S. (2002). Dynamic processes controlling foreland development – the role of mechanical (de)coupling of orogenic wedges and forelands. EGU Stephan Mueller Special Publication Series, 1, 17–56.

Ziegler, Peter A., Cloetingh, S., & van Wees, J.-D. (1995). Dynamics of intra-plate compressional deformation: the Alpine foreland and other examples. Tectonophysics, 252(1), 7–59. https://doi.org/10.1016/0040-1951(95)00102-6

Chapter 2

Methodology

2.1 Modeling approach

In this study I use two currently most advanced open-source geodynamic codes to study intraplate compression and subduction dynamics. The first code LaMEM (Lithosphere and Mantle Evolution Model, Kaus et al., 2016), written in C++, is developed by the Geophysics and Geodynamic group at the Institut für Geowissenschaften at Johannes Gutenberg Universität Mainz. This code has been employed to study several thermomechanical geodynamic problems, such as folding and faulting, oceanic subduction and continental collision, mountain building and plateau formation (e.g., Lechmann et al., 2011; Pusok & Kaus, 2015; Ibarra et al., 2019). I also use another code ASPECT (Advanced Solver for Problems in Earth's ConvecTion, Bangerth et al., 2017) to develop the subduction model with crustal deformation on the overriding plate, and apply it to the plateau-foreland system of the Central Andes.

LaMEM includes several advanced numerical features. Firstly, it is built on top of PETSc (Portable, Extensible Toolkit for Scientific computation) so that it can achieve scalability on massively parallel machines. PETSc is a library storing data structures and routines for the scalable (parallel) solution of partial differential equations (Balay et al., 2019). The library provides a distributed array (DMDA) as well as a range of linear (KSP) and non-linear (SNES) iterative solvers for both linear and non-linear rheologies on complete MPI-based parallelization (Figure 2.1).

Secondly, the code uses a fully finite-difference staggered grid (FDStag) method to solve geodynamic conservation equations. In this method, several types of nodal points, at which different variables (e.g., velocity, pressure, temperature, density, viscosity) are defined, exist in the staggered mesh (Figure 2.2). One important feature of this method is that computation using fully staggered grids is the most convenient way to solve finite-difference geodynamic problems with strongly variable viscosity (Gerya, 2010). Another feature is that it provides a low-order but stable discretization for (almost) incompressible fluid flow (Kaus et al., 2016).

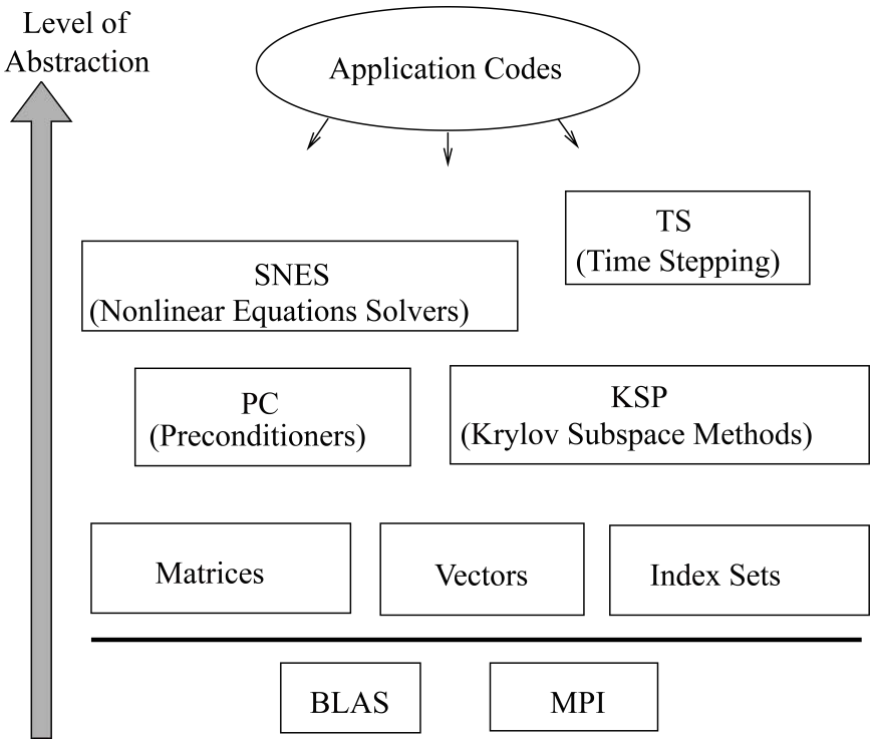

Figure 2.1. Numerical libraries of PETSc, showing the increasing level of abstraction, modified from PETSc manual. This hierarchical organization of the library enables users to employ the most appropriate solver for a particular problem.

Thirdly, the Marker-And-Cell (MAC) method is applied to follow the trail of material properties distributed on a large number of Lagrangian markers, and the marker advection along with a given/computed velocity field in the immobile, Eulerian grid. Fourthly, a combination of a fourth-order Runge-Kutta advection scheme with a conservative velocity interpolation method is used to prevent spurious clustering of the material markers. When calculating the effective strain rate on the markers, the rigid-body rotation part requires the correction of elastic history stresses from the last time step. Another requirement is the interpolation of these stresses on the edge and cell control volumes using the distance-based averaging (Figure 2.2). This code also allows the creation of complex input model geometries by using polygonal meshes with geometric mesh refinement. The refinement ensures the high resolution of the small concentrated region in a large-scale numerical model (e.g., crustal deformation localization in the upper mantle-scale shortening model in this study).

One of the most challenging issues in general geodynamic simulations with strongly non-linear rheology, particularly in large-size 3D models, is the slow convergence of iterations. Since the problem size of the model is large (i.e., solving millions to billions of non-linear equations), a

precise solution is challenging to achieve, and the simulation may diverge. LaMEM provides several multigrid (MG) solvers (e.g., Galerkin GMG, AMG) to speed up this convergence. In the MG method, the same equations are solved in parallel on several grids with different resolution and exchanged information between these grids. Thus, it makes the number of iteration cycles independent of the number of grid points. MG is exceptionally efficient for some simple cases such as solving the Poisson equation and increases convergence rate by several orders of magnitude (Gerya, 2010). Another way to facilitate convergence is to minimize the numerical diffusion by decreasing the magnitude of the time step to satisfy the time limitation condition (Gerya, 2010). At this stage, the material displacement should not be more than one grid step per one-time step. This ensures the stability of the numerical solution.

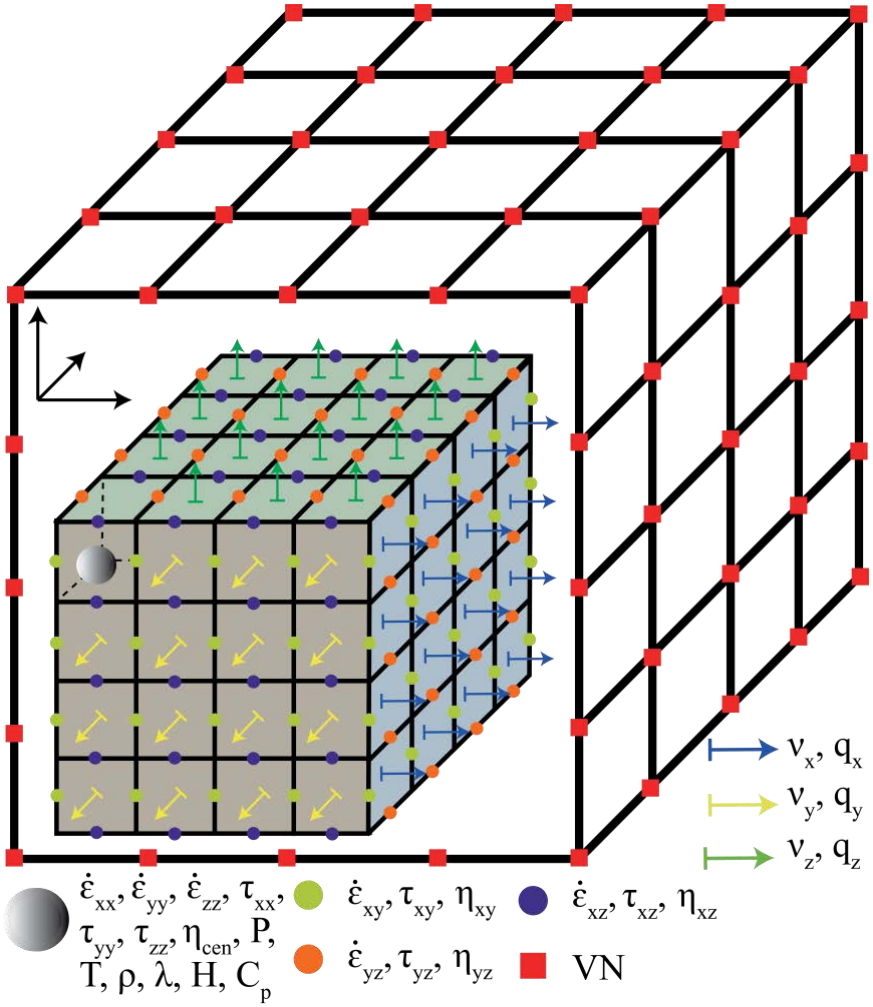

Figure 2.2. The fully-staggered finite-difference grid layout, illustrating the discretization of variables (velocity, temperature, pressure, composition, viscosity, heat flow, etc.). VN is a visualization node.

The open-source code ASPECT, also written in C++, is primarily designed to solve the equations for thermally driven convection and long-term tectonic deformation (Figure 2.3). It is spearheaded by computational scientists at Colorado State University and Clemson University (Kronbichler et al., 2012; Bangerth et al., 2017), who have integrated the development efforts of more than fifty researchers with different geoscience backgrounds worldwide. It has been employed to not only study global-scale mantle convection and plate tectonics problems (e.g., Dannberg & Gassmöller, 2018; Bredow & Steinberger, 2018; Steinberger et al., 2019), but also to explore regional-scale subduction dynamics and surface process problems (e.g., Austermann et al., 2017; Glerum et al., 2018). This finite-element code is built on the DEAL.II library (for finite elements, geometries, meshes, etc.) and indirectly uses Trilinos (for scalable and parallel linear algebra) and P4EST (for the handling of parallel meshes) MG solvers. These libraries are well tested and widely used by a large user community. ASPECT implements modern numerical methods and sophisticated algorithms that efficiently manage CPU and memory resources.

There are several advanced numerical features in ASPECT. One notable feature is that it is designed to be an extensible code, which uses both a plugin architecture and a set of options to replace or extend specific components of the program. For instance, realistic material properties (e.g., rheology, temperature, density), the geometry, and boundary conditions can be replaced at the beginning of the model run. Another unique characteristic is the implementation of fully adaptive mesh refinement, which enables small local objects to be resolved in the flow field - such as faults and shear zones - without having to refine the mesh for the whole model. Unlike the fully staggered discretization, which applies in the finite-difference code LaMEM, it is not easy to choose the discretization way in finite-element, especially for solving the Boussinesq problem. The finite elements chosen for velocity and pressure need to satisfy the usual compatibility condition for saddle point problems. To avoid this difficulty and obtain an accurate discretization, the code uses pressure stabilization schemes for low-order discretization, although the high-order method can offer more reliability and more accuracy with fewer unknowns.

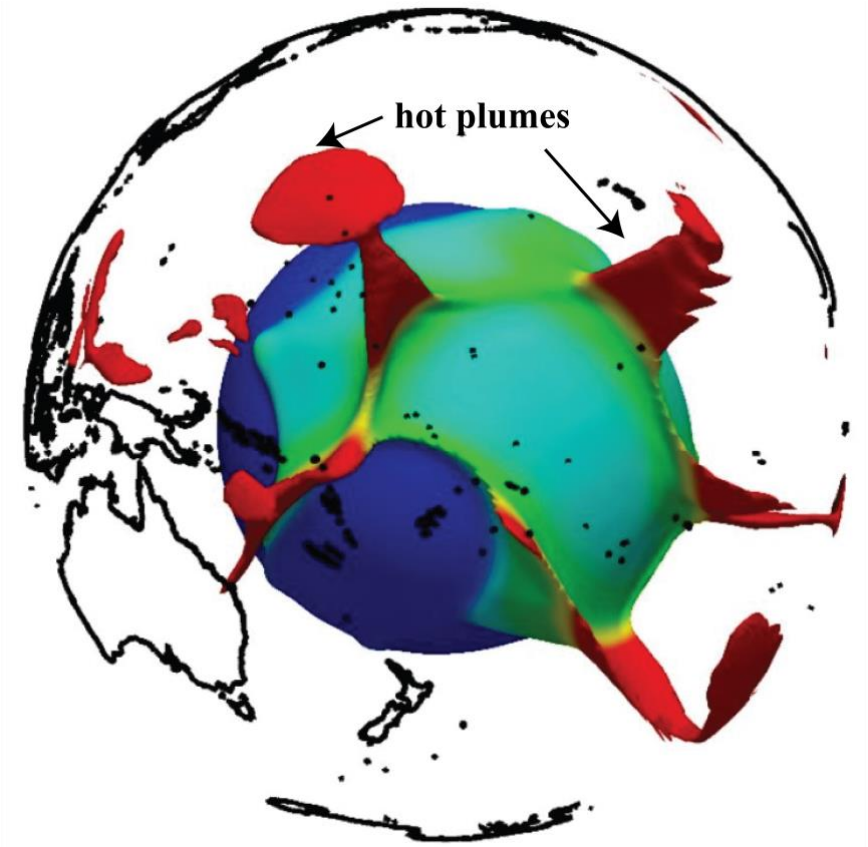

Figure 2.3. A numerical model example using the ASPECT code, developed by Gassmöller et al. (2016). The hot material rises as plumes (red) mostly from the margins of the chemically dense piles (green).

The ASPECT code can stabilize the solution of highly advection-dominated temperature equation by using a nonlinear artificial diffusion method. An efficient solution strategy in ASPECT, particularly important for the large 3D problems, is based on a block triangular preconditioner utilizing an algebraic multigrid, which provides an optimal solution for equations with hundreds of millions of unknowns. The code also has a nearly perfect performance in highly parallelized simulations (see the section of scalability test).

The surface boundary condition is critical to explore surface deformation, which is physically defined by the deformed surface elements in geodynamic simulations. Hence, the top boundary condition should be stress-free (i.e., both shear and normal stresses at the top boundary should be zero), allowing the surface to be deformed. Many geodynamic codes, including LaMEM, use the "sticky air" approximation on the top boundary to approximate free surface (e.g., Schmeling et al., 2008; Gerya, 2010; Kaus et al., 2010; Crameri et al., 2012). In this approximation, there is a soft buoyant layer with a low-viscosity and a low-density “air” above

the free surface. This layer decouples the free surface from the boundary. A free-slip condition is typically used for the top boundary, though an open boundary could be a better choice (Hillebrand et al., 2014). Another option is to use a real free surface so that the surface point can be deformed. With this setup, materials can flow in and out of the free surface. Both the pure free surface condition and sticky air condition with free-slip or open traction boundary can be implemented in ASPECT (Rose et al., 2017).

Although an exact free surface boundary condition more closely matches the real condition in geodynamic modeling, a frequent remeshing of the deformable mesh is required to avoid ill-conditioned elements. As a result, it takes more computing resources to implement this remeshing. In more complex geodynamic simulations, the free surface condition can increase the unstable property of simulation and results in a "sloshing" or "drunken sailor" instability (Kaus et al., 2010; Duretz et al., 2011). For example, if there is a significant amount of surface deformation, then the mesh at the top will be strongly distorted, which prevents the iteration from converging. Both LaMEM and ASPECT employ the free surface stabilization approach (Kaus et al., 2010) to stabilize the simulation and increase its time step.

2.2 Governing equations in computational geodynamics

Many geodynamic problems can be described by partial differential equations (PDEs) and boundary conditions in the model domain. In computational geodynamics, three conservation equations of momentum (Equation 1), mass (Equation 2) and energy (Equation 3) below, which are all PDEs with more than one independent variable, are considered to govern material deformation in subduction models:

$$\frac{\partial \sigma_{ij}}{\partial x_j} + \rho g_i = 0 \tag{1}$$

$$\frac{1}{K}\frac{DP}{Dt} - \alpha \frac{DT}{Dt} + \frac{\partial v_i}{\partial x_i} = 0 \tag{2}$$

$$\rho C_p \frac{DT}{Dt} = \frac{\partial}{\partial x_i}\left(k \frac{\partial T}{\partial x_i}\right) + H \tag{3}$$

where *i, j* represent spatial directions following Einstein summation convention, $x_{i,j}$ is the Cartesian coordinate, $\sigma_{ij} = \tau_{ij} - P\delta_{ij} = 2\eta\dot{\varepsilon}_{ij} - P\delta_{ij}$ is the Cauchy stress tensor with τ_{ij} deviatoric stress tensor, P pressure, δ_{ij} Kronecker delta (1 for $i=j$ and 0 otherwise), η the

viscosity, $\dot{\varepsilon}_{ij} = \frac{1}{2}\left(\frac{\partial v_i}{\partial x_j} + \frac{\partial v_j}{\partial x_i}\right)$ deviatoric strain rate tensor, ρ is the density, g_i is the gravitational acceleration vector, $v_{i,j}$ is the velocity, D/Dt is the material time derivative, K is bulk modulus, α is the thermal expansion coefficient, C_p is the specific heat, k is the thermal conductivity, and H is volumetric heat source. The heat source includes radiogenic heating due to the radioactive decay in the interior of the Earth, shear heating assuming that dissipated mechanical energy is converted to heat, adiabatic heating due to the material compression, and latent heat from material phase transition. If the material is assumed to be incompressible (i.e., the density of material does not change through time) and neglect thermal diffusion, the continuity equation is simplified as $\frac{\partial v_i}{\partial x_i} = 0$.

The volumetric heat source in the code LaMEM includes only shear heating, controlled by the efficiency parameter $0 \leq \chi \geq 1$, and the radiogenic heat A:

$$H = \chi \tau_{ij}\left(\dot{\varepsilon}_{ij}^{v} + \dot{\varepsilon}_{ij}^{p}\right) + \rho A \qquad (4)$$

Where $\dot{\varepsilon}_{ij}^{v}$, $\dot{\varepsilon}_{ij}^{p}$ are viscous and plastic strain-rate deviators, which can be calculated by $\dot{\varepsilon}_{II}^{v\ or\ p}\frac{\tau_{ij}}{\tau_{II}}$. The subscript II denotes the square root of the second invariant of a corresponding tensor. For example, the second invariant of the deviatoric strain rate $\dot{\varepsilon}_{II} = \sqrt{\frac{1}{2}\dot{\varepsilon}_{ij}\dot{\varepsilon}_{ij}}$.

2.3 Constitutive laws in computational geodynamics

Rocky rheology characterizes deformation behavior of the rock subjected to applied stress. It depends on several rock properties, such as temperature, pressure, stress, grain size, melt, or fluid content. Our Earth is composed of solid rocks that have spatial-temporal behavior. On the short length and time scales, the rock behaves as a rigid solid. When the length and time scale are longer, it begins to behave more in a fluid way that can flow. The property that describes how rocks flow is viscosity, and it can indicate the strength of the material. The mathematical description of the rock rheology is given by the stress-strain rate constitutive equation. In geodynamics, rocks commonly include three rheologies: elasticity, viscosity, and plasticity. The elasto-visco-plastic constitutive equation is given by:

$$\dot{\varepsilon}_{ij} = \dot{\varepsilon}_{ij}^{e} + \dot{\varepsilon}_{ij}^{v} + \dot{\varepsilon}_{ij}^{p} \qquad (5)$$

where $\dot{\varepsilon}_{ij}^{e}$ is the elastic strain-rate deviator, and equal to $\frac{\frac{\partial \tau_{ij}}{\partial t} + \tau_{ik}\omega_{kj} - \tau_{kj}\omega_{ik}}{2G}$, the spin tensor $\omega_{ij} = \frac{1}{2}\left(\frac{\partial v_i}{\partial x_j} + \frac{\partial v_j}{\partial x_i}\right)$, G is the elastic shear modulus.

Elastic deformation. Rocks behave elastically in a relatively short time-scale and under low temperature and pressure. An elastic material (like a spring) is deformed under a compressional force and recover to its original shape once removing the force. The elastic behavior can be described by Hooke's law, which states the proportionality of stress and strain. In this geodynamics simulation, we use the relationship between the deviatoric stress and the deviatoric strain (ε_{ij}) as:

$$\tau_{ij} = 2G\varepsilon_{ij} \tag{6}$$

Viscous creep. Generally, the dominant mechanism of rock deformation in the Earth's crust and mantle is the solid-state creep, which is the ability of crystalline substances to deform irreversibly under applied stresses. The significant creep types are known as diffusion creep, dislocation creep, and Peierls creep (Figure 2.4). The magnitude of the viscous creep strain rate is calculated by the sum of each component (Popov & Sobolev, 2008; Kaus et al., 2016):

$$\dot{\varepsilon}_{II}^{v} = \dot{\varepsilon}_{diff} + \dot{\varepsilon}_{disl} + \dot{\varepsilon}_{peir} \tag{7}$$

The migration of crystalline defects through the lattice of a crystal subjected to applied stresses causes diffusion creep. As a result of this diffusion, the crystalline solids suffer the bulk rock deformation. The diffusion creep deformation can be described by the relationship between the strain rate $\dot{\varepsilon}$ and deviatoric stress τ:

$$\dot{\varepsilon}_{diff} = A_{diff}\tau r^{-m} exp\left(-\frac{E+PV}{RT}\right) \tag{8}$$

Where A_{diff} is a prefactor which is independent of stress but depends on grain size (r), pressure, temperature, oxygen, and water fugacity (Hirth & Kohlstedt, 2003). m is the grain size exponent. In this equation, the strain rate is linearly dependent on stress, and thus resulting in Newtonian rheology.

Dislocation creep results from the movement of imperfections in the crystalline material, known as dislocation, through the crystal lattice of the material. This kind of creep is characterized by a non-linear (non-Newtonian) relationship between the strain rate and deviatoric stress:

$$\dot{\varepsilon}_{disl} = A_{disl}\tau^{n} exp\ (-\frac{E+PV}{nRT}) \qquad (9)$$

Where A_{disl} is a coefficient depending on temperature, pressure, oxygen, and water fugacity, and n is the stress exponent.

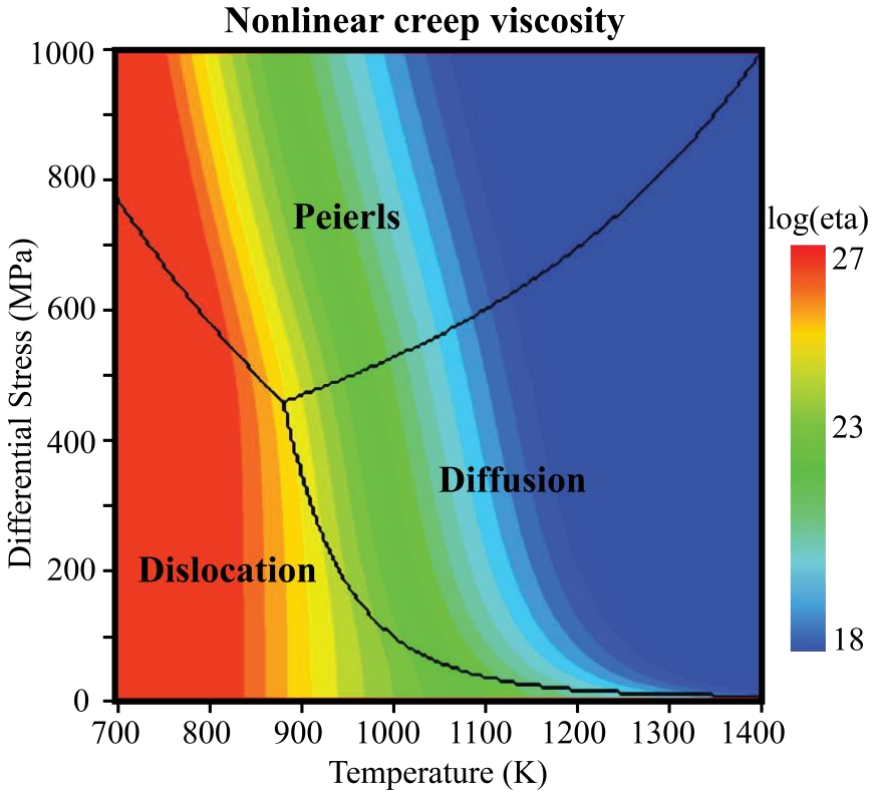

Figure 2.4. The logarithm of effective non-linear viscosity (eta) for the dry olivine on the differential stress-temperature map, modified from Popov and Sobolev (2008). Solid black lines separate three different creep mechanisms that produce the largest strain rate. Viscosity ranges between $10^{18}$and 10^{27} Pa s.

At high stresses and low temperature, the Peierls creep mechanism will take over from the dislocation creep mechanism. The constitutive relationship in the Peierls mechanism for the exponential flow law is commonly represented as (Katayama & Karato, 2008):

$$\dot{\varepsilon}_{peir} = A_{peir}\tau_{II}^2 exp\left[-\frac{E+PV}{RT}\left(1-\left(\frac{\tau_{II}}{\tau_{peir}}\right)^p\right)^q\right] \quad (10)$$

where A_{peir} is a prefactor, R is the gas constant, $E + PV$ is the activation enthalpy, τ_{peir} is the Peierls stress, p and q are non-dimensional exponents that depend on the geometry of kinks.

The creep rheologies are often calibrated from experimental data (Hirth & Kohlstedt, 2003; Katayama & Karato, 2008; Karato, 2010). Figure 2.5 shows a general lithospheric structure and laboratory-derived flow laws using four different phases in our numerical models. In order to be consistent with the experimental parameters in numerical modeling, materials deform viscously with an effective viscosity (η_{eff}) given by:

$$\eta_{eff} = \frac{1}{2B^{1/n}}\dot{\varepsilon}_{II}^{\frac{(1-n)}{n}} exp\left(\frac{E+PV}{nRT}\right) \quad (11)$$

where $B = FAh^m$ is the material constant, h is grain size, A, n, m, E, V are the pre-exponential viscosity parameter, stress exponent, grain size exponent, activation energy and activation volume, respectively from laboratory experiments. The stress exponent is 1 for diffusion creep, and greater than 1 in case of dislocation creep (Equations 8 and 9). The grain size exponent is 0 for dislocation creep as it is grain size-dependent. In contrast, the value is negative in diffusion creep due to the increase of strain rate with decreasing grain size. The dimensionless coefficient F depends on the type of experiment: uniaxial compression experiment or simple shear experiment. F is obtained as $2^{(n-1)/n}3^{(n+1)/2n}$ in the first type. In the latter experiment, F equals to $2^{(1-2n)/n}$.

Plastic deformation. Rocks experience a plastic failure once the applied stress exceeds the shear stress limit, which is known as Byerlee's law (Byerlee, 1978). Like viscous deformation, plastic yielding is irreversible. In our numerical method, the material performs the frictional-plastic deformation when the deviatoric stress exceeds the plastic yield stress, which follows a pressure-dependent Drucker-Prager yield criterion. Then the magnitude of the plastic strain rate is determined from:

$$\tau_{II} \leq \tau_Y = P\ sin\ sin\ \varphi + C_0\ cos\ cos\ \varphi \quad (12)$$

where φ is the internal friction angle, and C_0 is the cohesion. In ASPECT, the Drucker Prager yield surface is the same as the Mohr-Coulomb surface in 2D. If φ = 0 (i.e., no pressure dependence) in 2D, then these criteria revert to the von Mises criterion (Thieulot, 2011). In 3D the yield criterion changes to:

$$\tau_Y = \frac{6C_0 coscos\,\varphi}{\sqrt{3}(3+sinsin\,\varphi)} + \frac{2Psinsin\,\varphi}{\sqrt{3}(3+sinsin\,\varphi)} \quad (13)$$

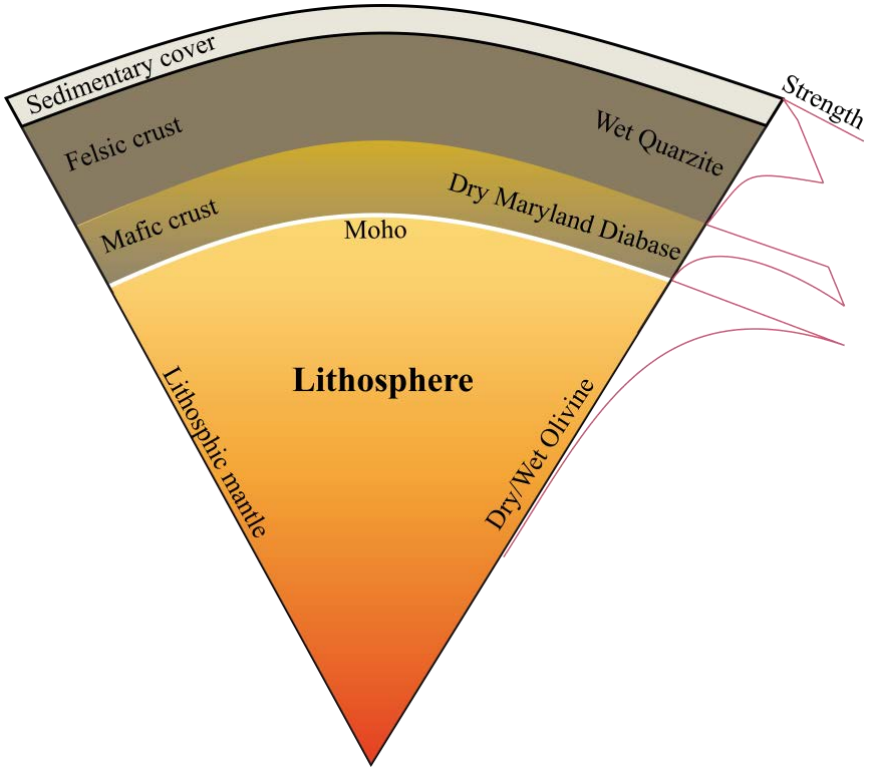

Figure 2.5. A sketch of lithospheric structure from top sedimentary layer to bottom lithospheric mantle. Different laboratory-derived flow laws are used for each phase.

2.4 Scalability test

We performed several tests to verify the parallel scalability of LaMEM and ASPECT on HLRN (North-German Supercomputer Alliance) and both codes perform almost perfect scaling behavior. The LaMEM model can run on a variety of machines ranging from laptops to a massively parallel cluster with thousands of processors. In the test running on HLRN, the amount of processors increases to the computing limit 6144. The same test is also done using another supercomputer center JUQUEEN by using up to 458,752 processors with more than 15 billion grid points (Kaus et al., 2016). The LaMEM code calls the Matlab software

(www.mathworks.com/products/matlab/) to create the geometry and initial temperature field of the model. Visualization of models uses the ParaView software (www.paraview.org).

Figure 2.6 illustrates the parallel scaling test of the two codes on HLRN for the application of simplified subduction model. This test model is 3,000 km long and 400 km wide and includes the oceanic plate and upper mantle with the sticky air on the top (Figure 2.6a). The black line is the ideal parallel line, and the number 1-6 represents the number of velocity degree of freedoms (vDOFs) increasing from 65,000 to 66,000,000 by a factor of 4. The largest size of the model is > 18 million cells with half billion markers on 6144 cores since this is the maximum number of computing nodes we can use on HLRN. It demonstrates excellent scaling behavior, and the scalability improves with problem size, where the colored line approaches the linear black line. The shortest simulation time in each model depends on the problem size. Each core of the node on HLRN can achieve its peak value for solving the nonlinear equations in LaMEM when the problem size is more than 1.1 million grid points in Figure 2.6b.

I also test ASPECT for scaling with MPI implementation on HLRN (Figure 2.5c). ASPECT also scales well up to the maximum number of cores we used in the given setting. Based on the test, we estimate that if 30,000 - 300,000 DOFs are used, the calculations scale up almost linearly. The highest tested resolution showed excellent scaling up to 6144 cores or 256 nodes. Further details about the code scaling test, also for single parts of the code, are presented in Kronbichler et al., (2012).

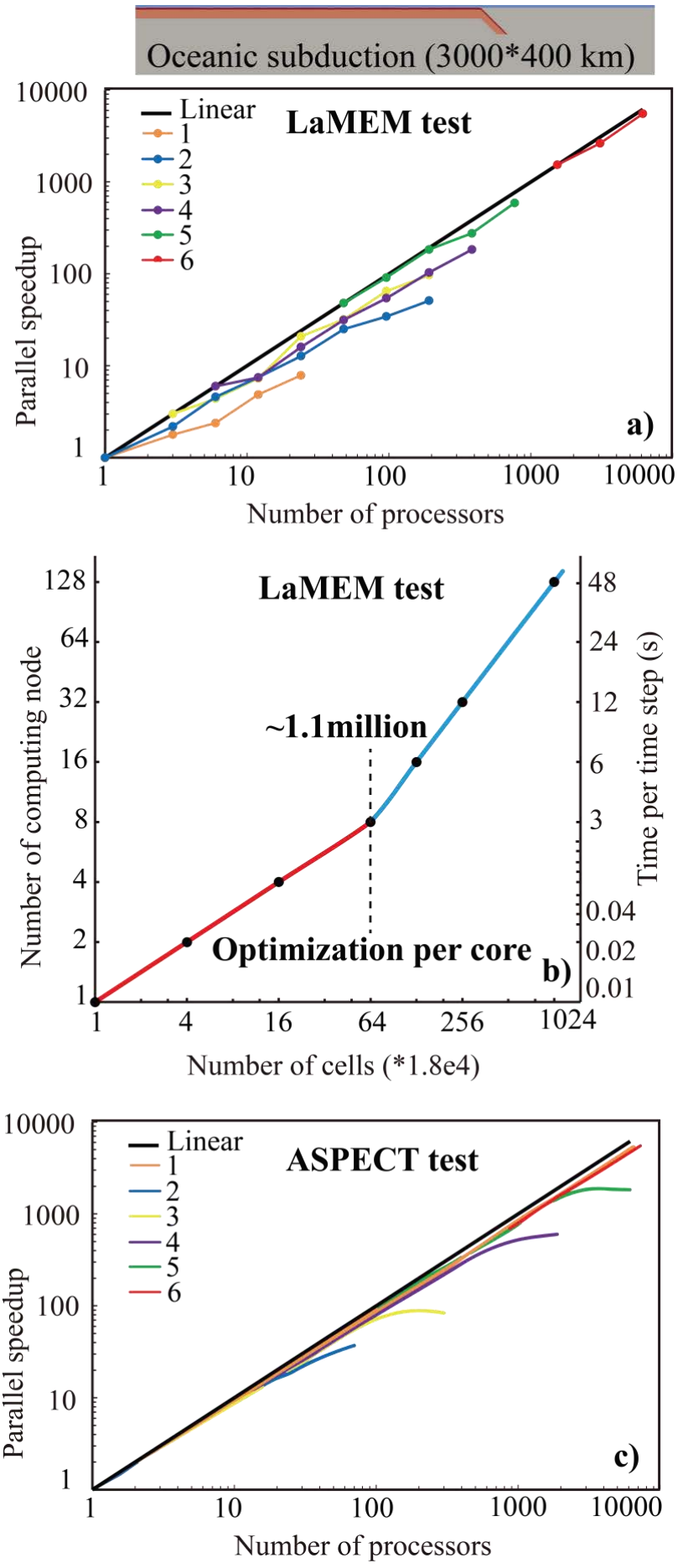
Oceanic subduction (3000*400 km)
LaMEM test
Linear
1
2
3
4
5
6
Parallel speedup
Number of processors
a)
LaMEM test
~1.1million
Optimization per core
b)
Number of computing node
Time per time step (s)
Number of cells (*1.8e4)
ASPECT test
c)

Figure 2.6. Scaling performances of LaMEM and ASPECT on HLRN. **a)** shows a parallel speedup to the lowest processors for LaMEM. The number of velocity DOFs ranges from 6.5e4 (1) to 6.6e7 (6). **b)** shows that the optimal number of computing nodes provides the shortest execution time for different problem sizes for LaMEM. **c)** shows a parallel speedup to the lowest processors for ASPECT.

2.5 Brittle thrust wedges benchmark

Thrusting of the brittle crust by applying compressive forces can lead to large deformation. The process is difficult to simulate because the rheology of the cold, brittle crust is substantially more complicated than that of the hot, ductile rocks in the mantle. At the same time, brittle deformation can be well visualized using simple "sandbox" experiments in which a number of layers of differently-colored sand are compressed or stretched. One can then observe examples of the patterns in the figures of analog models in Bangerth et al. (2017). Buiter et al. (2016) compare sandbox analog and numerical experiments. The numerical benchmark presented here aims to prove that the wedge models computed using ASPECT code are consistent with the results of other codes and with the analytical wedge theory solutions. In particular, we attempt to reproduce the numerical simulations of stable wedge experiment 1 (Figure 2.7) and unstable wedge experiment 2 (Figure 2.8) with the same model setups in this paper.

Several model sets of prescribed material behavior are required to simulate the brittle thrust formation successfully. For example, the behavior of plastic strain-weakening, with the internal angle of friction diminishing between total finite strain invariant values of 0.5 and 1.0, is prescribed to mimic the softening from peak to stable dynamic strength which correlates with sand dilation. The reason why uses this weaning is that the sand performs plastic yielding at the beginning of shortening due to the non-viscous property, even if the material in the numerical model has a visco-plastic rheology. The boundary 2-mm-thin layers (bound) sit on both the bottom of the domain and between the sand and rigid indenter block. The rigid block approximates a movable wall with a constant velocity of 2.5 cm/hour on the right-hand side boundary to drive the deformation in the sand layers. The boundary between the rigid block and boundary layers produces a sharp velocity discontinuity that localizes brittle deformation. For the top boundary condition, zero traction (“open”) and a sticky air layer is used to approximate a free surface. Additional testing revealed that using a real free surface leads to significant mesh distortion and associated numerical instabilities.

Accurate solver convergence is always challenging to achieve in numerical thrust wedge models with a high spatial resolution (ca. 1 mm node spacing here) and a significant viscosity contrast. Several parameters should be considered carefully to constrain the convergence. Firstly, the nonlinear and linear solver tolerances should be sufficiently strict to avoid numerical instabilities. Secondly, the discontinuous Galerkin method can be used to ensure that the discontinuous composition bound-preserving limiter produces sharp interfaces between compositional layers. Lastly, the harmonic averaging scheme (e.g., Glerum et al., 2018) for material and viscosity is required to achieve reasonable convergence behavior.

Experiment 1 tests whether model wedges in the stable domain of critical taper theory remain stable when translated horizontally. A quartz sand wedge, with a horizontal base and a surface slope of 20 degrees, is pushed 4 cm horizontally by inward movement of a mobile wall, at the right boundary, with a velocity of 2.5 cm/hour (Figure 2.7). A thin layer separates the sand and boundary, which ensures minimum coupling between the wedge and bounding box during translation. A sticky air layer above the wedge is used to ensure that the purely plastic material does not undergo any deformation during translation.

Experiment 2 tests how an unstable subcritical wedge deforms to reach the critical taper solution. In this experiment, horizontal layers of sand undergo 10 cm shortening by inward movement of a movable wall with a velocity of 2.5 cm/hour (Figure 2.8). Model results show the generation of thrust wedge near the mobile wall through a combination of mainly in-sequence forward and backward thrusting. The strain field (Figure 2.7c) highlights several incipient shear zones that do not always accumulate enough offset to become visible in the material field. The pressure field of the model (Figure 2.7d) remains more or less lithostatic, with lower pressure values in (incipient) shear zones.

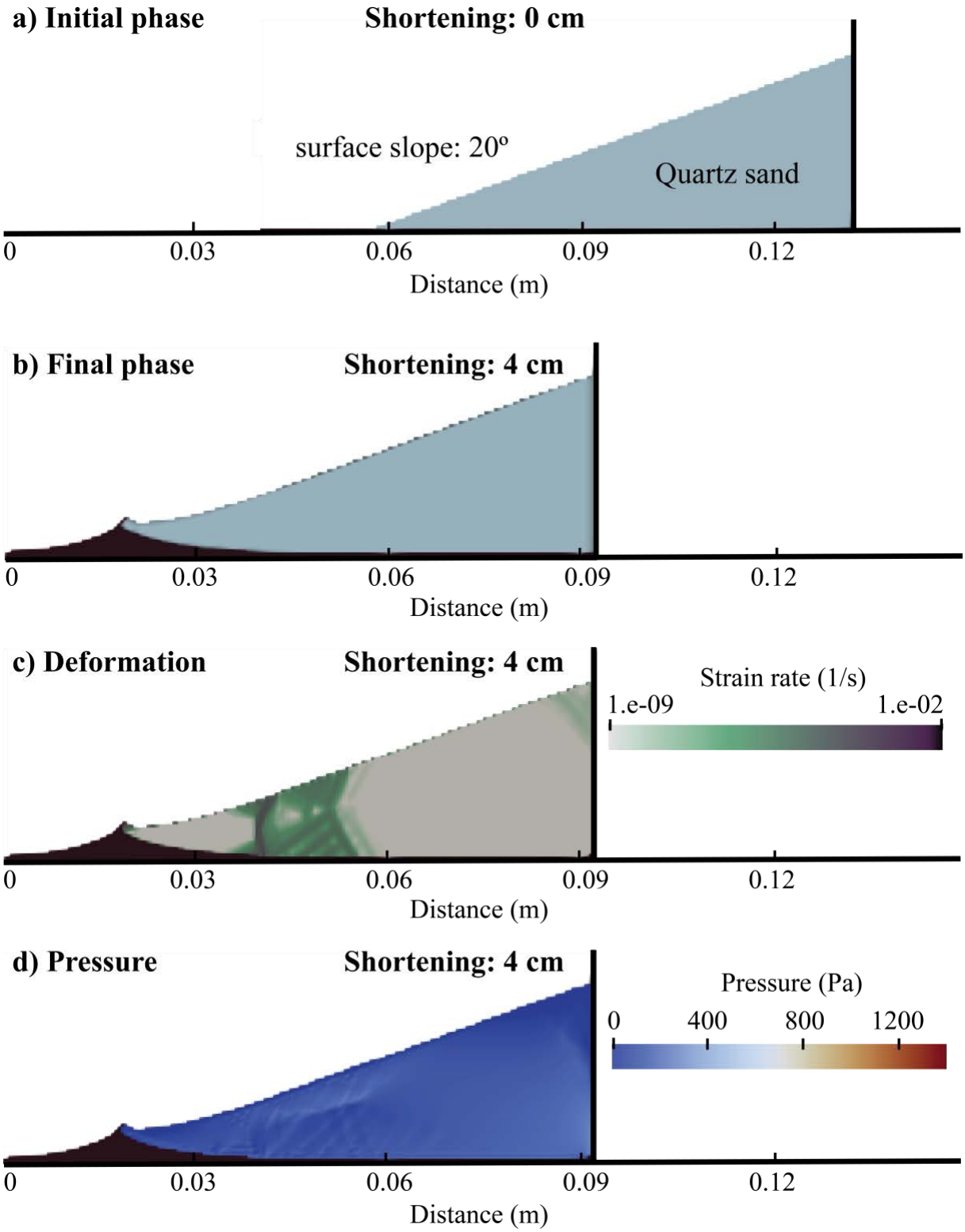

Figure 2.7. The numerical model of a stable sand wedge. **a)** Initial model setup. **b-d)** Final material field, strain rate field, and pressure field after 4 cm of translation.

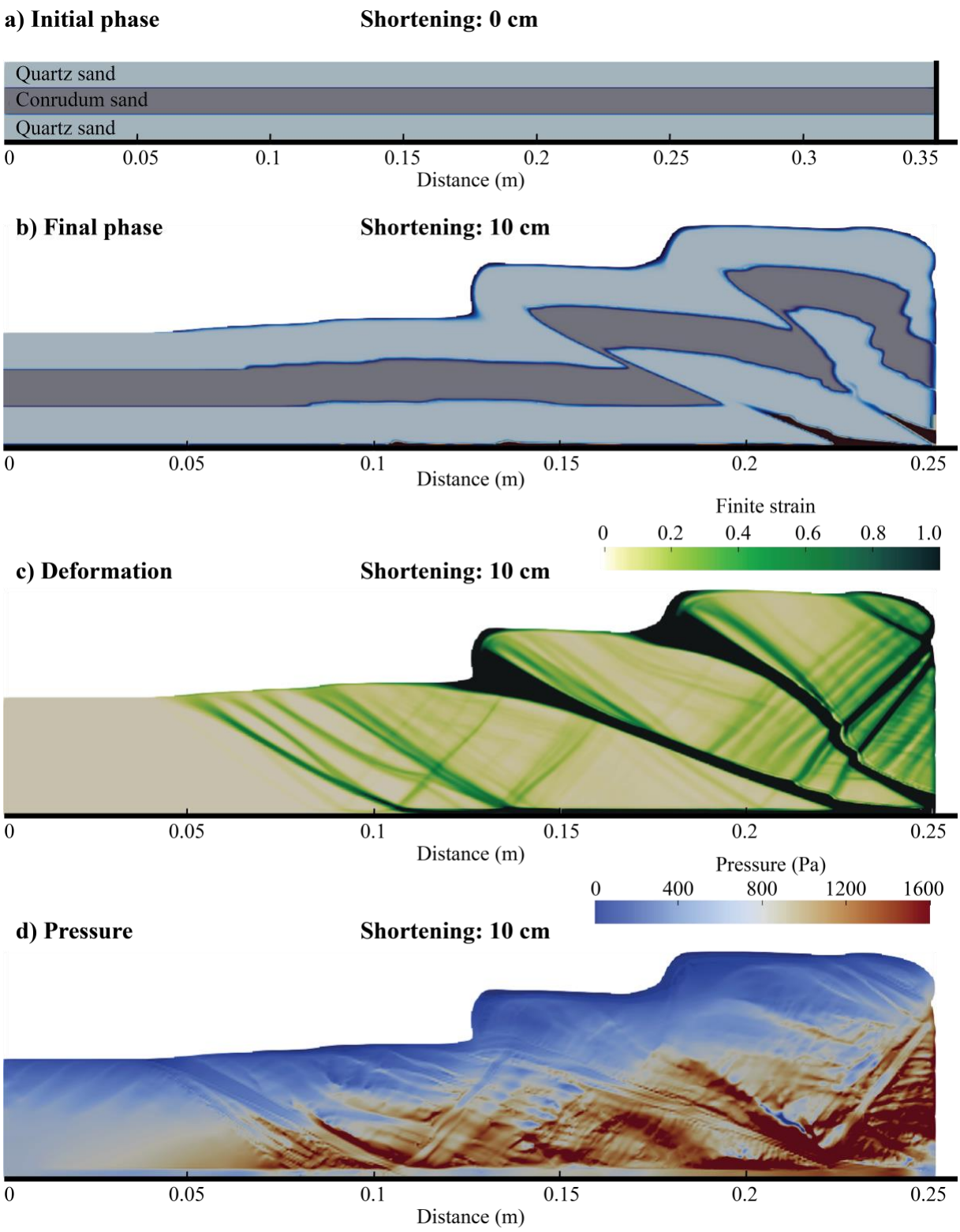

Figure 2.8. The numerical model of an unstable subcritical wedge. **a)** Initial model setup. **b-d)** Final material field, finite strain field, and pressure field of sands after 10 cm shortening.

References

Austermann, J., Mitrovica, J. X., Huybers, P., & Rovere, A. (2017). Detection of a dynamic topography signal in last interglacial sea-level records. *Science Advances*, *3*(7), e1700457. https://doi.org/10.1126/sciadv.1700457

Balay, S., Abhyankar, S., Adams, M., Brown, J., Brune, P., Buschelman, K., et al. (2019). *PETSc users manual* (No. ANL-95/11-Revision 3.11). Argonne National Laboratory. Retrieved from https://www.mcs.anl.gov/petsc

Bangerth, W., Dannberg, J., Gassmöller, R., Heister, T., & others. (2017). ASPECT: Advanced Solver for Probelms in Earth's ConvecTion, User Manual. *Figshare*. https://doi.org/doi.org/10.6084/m9.figshare.4865333.v2

Bredow, E., & Steinberger, B. (2018). Variable Melt Production Rate of the Kerguelen HotSpot Due To Long-Term Plume-Ridge Interaction. *Geophysical Research Letters*, *45*(1), 126–136. https://doi.org/10.1002/2017GL075822

Buiter, S. J. H., Schreurs, G., Albertz, M., Gerya, T. V., Kaus, B., Landry, W., et al. (2016). Benchmarking numerical models of brittle thrust wedges. *Journal of Structural Geology*, *92*, 140–177. https://doi.org/10.1016/j.jsg.2016.03.003

Byerlee, J. (1978). Friction of rocks. *Pure and Applied Geophysics*, *116*(4–5), 615–626. https://doi.org/10.1007/BF00876528

Crameri, F., Schmeling, H., Golabek, G. J., Duretz, T., Orendt, R., Buiter, S. J. H., et al. (2012). A comparison of numerical surface topography calculations in geodynamic modelling: an evaluation of the 'sticky air' method. *Geophysical Journal International*, *189*(1), 38–54. https://doi.org/10.1111/j.1365-246X.2012.05388.x

Dannberg, J., & Gassmöller, R. (2018). Chemical trends in ocean islands explained by plume–slab interaction. *Proceedings of the National Academy of Sciences*, *115*(17), 4351–4356. https://doi.org/10.1073/pnas.1714125115

Duretz, T., May, D. A., Gerya, T. V., & Tackley, P. J. (2011). Discretization errors and free surface stabilization in the finite difference and marker-in-cell method for applied geodynamics: A numerical study. *Geochemistry, Geophysics, Geosystems*, *12*(7), Q07004. https://doi.org/10.1029/2011GC003567

Gassmöller, R., Dannberg, J., Bredow, E., Steinberger, B., & Torsvik, T. H. (2016). Major influence of plume-ridge interaction, lithosphere thickness variations, and global mantle flow on hotspot volcanism—The example of Tristan. *Geochemistry, Geophysics, Geosystems*, *17*(4), 1454–1479. https://doi.org/10.1002/2015GC006177

Gerya, T. (2010). *Introduction to numerical geodynamic modelling*. Cambridge, UK; New York: Cambridge University Press. Retrieved from http://dx.doi.org/10.1017/CBO9780511809101

Glerum, A., Thieulot, C., Fraters, M., Blom, C., & Spakman, W. (2018). Nonlinear viscoplasticity in ASPECT: benchmarking and applications to subduction. *Solid Earth*, *9*(2), 267–294. https://doi.org/10.5194/se-9-267-2018

Hillebrand, B., Thieulot, C., Geenen, T., van den Berg, A. P., & Spakman, W. (2014). Using the level set method in geodynamical modeling of multi-material flows and Earth's free surface. *Solid Earth*, *5*(2), 1087–1098. https://doi.org/10.5194/se-5-1087-2014

Hirth, G., & Kohlstedt, D. (2003). Rheology of the upper mantle and the mantle wedge: A view from the experimentalists. *Washington DC American Geophysical Union Geophysical Monograph Series*, *138*, 83–105. https://doi.org/10.1029/138GM06

Ibarra, F., Liu, S., Meeßen, C., Prezzi, C. B., Bott, J., Scheck-Wenderoth, M., et al. (2019). 3D data-derived lithospheric structure of the Central Andes and its implications for deformation: Insights from gravity and geodynamic modelling. *Tectonophysics*, *766*, 453–468. https://doi.org/10.1016/j.tecto.2019.06.025

Karato, S. (2010). Rheology of the Earth's mantle: A historical review. *Gondwana Research*, *18*(1), 17–45. https://doi.org/10.1016/j.gr.2010.03.004

Katayama, I., & Karato, S. (2008). Low-temperature, high-stress deformation of olivine under water-saturated conditions. *Physics of the Earth and Planetary Interiors*, *168*(3), 125–133. https://doi.org/10.1016/j.pepi.2008.05.019

Kaus, B. J. P., Mühlhaus, H., & May, D. A. (2010). A stabilization algorithm for geodynamic numerical simulations with a free surface. *Physics of the Earth and Planetary Interiors*, *181*(1–2), 12–20. https://doi.org/10.1016/j.pepi.2010.04.007

Kaus, B. J. P., Popov, A. A., Baumann, T. S., Pusok, A. E., Bauville, A., Fernandez, N., & Collignon, M. (2016). Forward and inverse modelling of lithospheric deformation on geological timescales. *NIC Symposium 2016 - Proceedings*, *48*, 299–307.

Kronbichler, M., Heister, T., & Bangerth, W. (2012). High accuracy mantle convection simulation through modern numerical methods. *Geophysical Journal International*, *191*(1), 12–29. https://doi.org/10.1111/j.1365-246X.2012.05609.x

Lechmann, S. M., May, D. A., Kaus, B. J. P., & Schmalholz, S. M. (2011). Comparing thin-sheet models with 3-D multilayer models for continental collision. *Geophysical Journal International*, *187*(1), 10–33. https://doi.org/10.1111/j.1365-246X.2011.05164.x

Popov, A. A., & Sobolev, S. V. (2008). SLIM3D: A tool for three-dimensional thermomechanical modeling of lithospheric deformation with elasto-visco-plastic rheology. *Physics of the Earth and Planetary Interiors*, *171*(1), 55–75. https://doi.org/10.1016/j.pepi.2008.03.007

Pusok, A. E., & Kaus, B. J. P. (2015). Development of topography in 3-D continental-collision models. *Geochemistry, Geophysics, Geosystems*, *16*(5), 1378–1400. https://doi.org/10.1002/2015GC005732

Rose, I., Buffett, B., & Heister, T. (2017). Stability and accuracy of free surface time integration in viscous flows. *Physics of the Earth and Planetary Interiors*, *262*, 90–100. https://doi.org/10.1016/j.pepi.2016.11.007

Schmeling, H., Babeyko, A. Y., Enns, A., Faccenna, C., Funiciello, F., Gerya, T., et al. (2008). A benchmark comparison of spontaneous subduction models—Towards a free surface.

Physics of the Earth and Planetary Interiors, *171*(1–4), 198–223. https://doi.org/10.1016/j.pepi.2008.06.028

Steinberger, B., Bredow, E., Lebedev, S., Schaeffer, A., & Torsvik, T. H. (2019). Widespread volcanism in the Greenland–North Atlantic region explained by the Iceland plume. *Nature Geoscience*, *12*(1), 61. https://doi.org/10.1038/s41561-018-0251-0

Thieulot, C. (2011). FANTOM: Two- and three-dimensional numerical modelling of creeping flows for the solution of geological problems. *Physics of the Earth and Planetary Interiors*, *188*(1), 47–68. https://doi.org/10.1016/j.pepi.2011.06.011

Chapter 3

Controls of foreland-deformation patterns in the orogen-foreland shortening system: Insights from high-resolution numerical models

A version of this chapter was submitted to the journal *Tectonics* and is under revision as Liu, S., Sobolev, S.V., and Babeyko, A.Y., Controls of foreland-deformation patterns in the orogen-foreland shortening system: Insights from high-resolution numerical models.

Abstract

Controls in the deformation pattern (shortening mode and deformation structure) of orogenic forelands during tectonic shortening remain poorly understood. Here, we use high-resolution 2D thermomechanical models to demonstrate that the orogenic crustal thickness and the foreland lithospheric thickness control the tectonic shortening mode in the foreland. Pure-shear shortening occurs when the orogenic crust is not thicker than the foreland crust or when it is thick but the foreland lithosphere is thin (< 70-80 km, as in the Puna foreland case). Simple-shear shortening, characterized by the foreland underthrusting beneath the orogen, takes place when the orogenic crust is much thicker than the foreland crust. The thickened orogenic crust causes the orogen to have high gravitational potential energy that prevents deformation in the orogen and forces shortening in the foreland, while the weak orogenic lithosphere allows the foreland lithosphere to underthrust beneath the orogen. Our models reproduce fully thick-skinned, fully thin-skinned, and intermediate deformation structures. The first structure forms in a pure-shear deformation mode, whereas the others require a simple-shear mode and the presence of thick (>~4 km) sediments that are mechanically weak (friction coefficient < ~0.05) before or are weakened rapidly during the deformation. Fully thin-skinned structures in the foreland, as in the Sub-Andean Ranges, form in thick and weak sediments and require the strength of the orogenic upper lithosphere to be less than about one-third of that of the foreland upper lithosphere. Our models successfully reproduce foreland-deformation patterns in the Central and South Andes and the Laramide province.

3.1 Introduction

Foreland deformation zones adjacent to the orogen constitute one of the main deformation features in the orogen-foreland shortening system. Pure-shear and simple-shear are two common shortening modes in these belts. Pure-shear shortening is characterized by a vertically quasi-homogeneous thickening of the foreland crust, while the foreland lithosphere underthrusts beneath the orogen along a low-angle detachment fault in the simple-shear mode. During shortening, the crustal-scale deformation in foreland deformation belts forms either shallow thin-skinned or deeper thick-skinned structures (e.g., Lacombe & Bellahsen, 2016; Pfiffner, 2017). In the former, the shortened rocks overlie an almost undeformed basement along a shallow basal décollement fault, while the basement is deformed above a deep crustal detachment zone in the latter (Dahlen, 1990).

In natural orogen-foreland systems, a number of regional studies have demonstrated the existence of these two types of structure in the foreland area (e.g., Figure 1.3), for example, in the Central-Southern Andes (e.g., Ramos et al., 2004; Babeyko et al., 2006; Giambiagi et al., 2011; Mescua et al., 2016), Southern Canadian Rockies (e.g., Price, 1981; Stockmal et al., 2007), Laramide Rocky Mountains (e.g., DeCelles, 2004; Yonkee & Weil, 2015), Taiwan and Alps (e.g., Lacombe & Mouthereau, 2002; Lacombe & Bellahsen, 2016).

The transition between the two shortening modes and the way thin-skinned and thick-skinned structures interact are unclear. Previous studies have attempted to quantify some of the relationships between shallow and deep lithospheric structures and processes; these studies suggested that the deformation pattern (i.e., shortening mode and deformation structure) are related to the reduction of lithospheric strength (e.g., Babeyko & Sobolev, 2005; Babeyko et al., 2006). In particular, Babeyko et al. (2006) demonstrated that drop of the mechanical strength of foreland sediments east of the Altiplano plateau is responsible for the switch of the shortening mode from pure-shear to simple-shear, as well as for the formation of the Subandean Ranges.

However, the exact nature of lithospheric strength variation and sediment weakening affecting the evolution of foreland deformation is still not well understood. These studies reveal the necessary conditions specifically for foreland deformation of the Altiplano-Puna plateau, characterized by thin lithosphere and thick plateau crust. In other regions, such as the Laramide

orogen or the Southern Canadian Rocky Mountains, however, the orogenic crust is not much thicker than the foreland crust (e.g., Bird, 1984; Currie, 2016). Therefore, the question of whether these conditions can be applied to explain the deformation pattern in other foreland areas is significant and remains open. The above-cited models also did not explore further details of foreland-deformation features (e.g., the fault direction) due to the lack of necessary numerical resolution at that time. Recent progress in numerical modeling techniques allows for an extension of this research to higher-resolution lithospheric models, which is the subject of the current study.

The long-term strength of the continental lithosphere is primarily controlled by its composition and temperature, which strongly depend on depth, i.e., the lithospheric thickness and the crustal thickness. A thicker lithosphere is colder and stronger due to its smaller temperature gradient (e.g., Kohlstedt et al., 1995). The crust is rheologically weaker than the mantle, and hence the entire lithospheric strength decreases when the crust is thickened. Composition, fluid content (degree of hydration), magmatism, and thermal/structural inheritance also influence the strength (e.g., Kohlstedt et al., 1995; Burov & Watt, 2006; Burov, 2011; Tesauro et al., 2013). The foreland lithosphere in the upper plate of an orogenic subduction-dominated system can be weakened by a high degree of hydration or a hot thermal structure due to the subduction dynamics. For example, the foreland area of the Puna plateau is hotter and weaker than the north Altiplano foreland (Whitman et al., 1996). In this study, we focus on the orogen-foreland compressional system and, thus neglect the subducting plate as well as the effect of its subduction dynamics on the long-term lithospheric strength in the upper plate.

Another critical factor, the sediment strength, should be considered separately from the lithospheric strength. On the one hand, although the sedimentary layer covering the foreland can be as thick as 8 km or more (Laske et al., 2013), it constitutes less than 10% of continental lithosphere. Therefore, the change of sediment strength has little effect on the entire lithospheric strength. On the other hand, the mechanically weakened sedimentary layer may form a weak zone in the boundary between the orogen and its foreland during shortening, which is critical to the initiation of foreland underthrusting (Babeyko & Sobolev, 2005). Therefore, a high-resolution model is required to ensure that the deformation in such a thin sedimentary layer is tracked correctly.

The friction coefficient is the most important property in determining the mechanical strength of sediments; the sediment is weaker if its friction coefficient is lower. The friction coefficient

has a wide range of values, from > 0.8 to < 0.05, depending on temperature, composition, pore-fluid pressure, and asperities along the fault surface (Hassani et al., 1997). For example, laboratory experiments indicate that the value can be as low as 0.1 if sedimentary rocks contain sufficient clay minerals such as montmorillonite or vermiculite (Byerlee, 1978). Heat-flow data suggest that the value ranges between 0.074 and 0.127 for different subduction zones (Gao & Wang, 2014). Previous geodynamic models constrain this range between 0.05 and 0.015 (Sobolev et al., 2006). A reduction in the friction coefficient can decrease the yield strength of the rock, accelerating its failure. The physical nature of potential frictional weakening in foreland sediments remains controversial. The weakening may be the result of high pore-fluid pressure (lowering the effective confining stress) due to rapid hydrocarbon generation (Cobbold et al., 2004 and reference therein), an increase in precipitation (e.g., Strecker et al., 2007), or compaction under strong compression in the foreland (e.g., Babeyko & Sobolev, 2005). Since we are concerned with the development of deformation patterns in the orogen-foreland system, the exact origin of the sediment friction drop is not discussed here.

In this study, we first examine how different factors (i.e., lithospheric thickness, crustal thickness, effective friction coefficient in sediments, sediment thickness) influence the lithospheric strength of both the orogen and its foreland, and the mechanical strength of foreland sediments. Then we systematically investigate how these parameters control the foreland-deformation pattern during shortening between the orogen and its foreland. Finally, we compare and apply model results to natural orogen-foreland systems such as the Central-Southern Andes and the Laramide province.

3.2 Numerical model description

3.2.1 Method and model geometry

The material deformation is governed by solving the system of the three basic conservation equations (see Appendix A) in the 2D Cartesian coordinate system. To solve the equations, we use the highly scalable parallel code LaMEM (Lithosphere and Mantle Evolution Model; Kaus et al., 2016). This advanced geodynamic code has been widely used to study geodynamic problems such as the folding and thrusting system and continental collision (e.g., Collignon et al., 2015; Pusok & Kaus, 2015). The initial model contains two structural domains - orogen and foreland (Figure 3.1**)** and is 400 km wide and 400 km deep. As we are interested in the

deformation of the foreland crust, we plot our modeling results in the zoom-in area in the top 60 km of the model (dashed grey rectangular in Figure 3.1) with a horizontal distance between 50 km and 330 km. We assume that the effect of side boundary conditions on the modeling result in this area to be minimized.

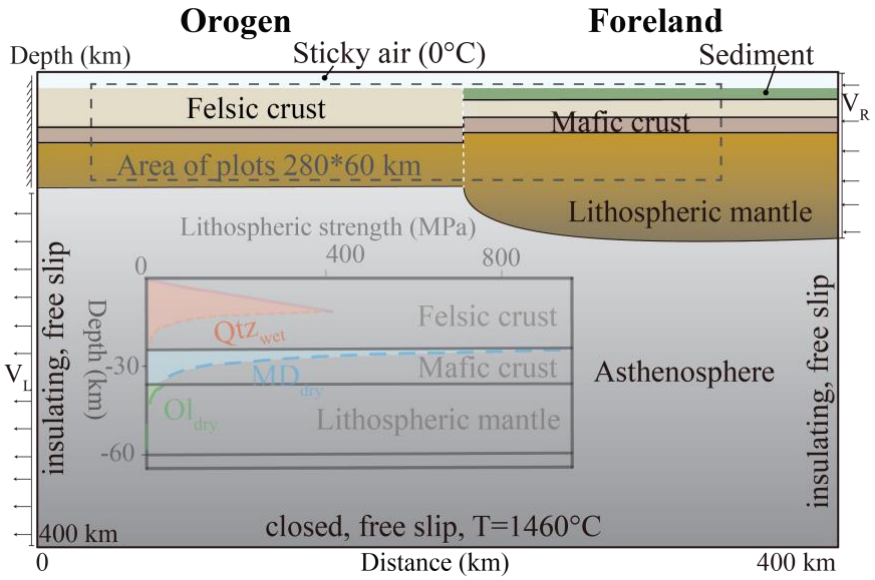

Figure 3.1. Initial model geometry with thermal-mechanical boundary conditions. Prescribed compressing velocity (V_R) from the right side is balanced by the uniform outflux velocity (V_L) along the left side boundary under the orogenic lithosphere. The white dash line is the boundary between the orogen and its foreland. Qtz_{wet}, MD_{dry}, and Ol_{dry} in the example of the 60-km-thick lithospheric strength profile indicate wet quartzite, dry Maryland diabase, and dry olivine, respectively.

The lithospheric thickness of either the orogen or its foreland in the model varies from 60 km to 200 km. Figure 3.1 shows a 60-km-thick lithospheric strength profile, which is an example of the thin and weak orogenic lithosphere due to the lithosphere delamination in orogens (e.g., Kay & Kay, 1993; Babeyko & Sobolev, 2005). Cratonic lithosphere is taken to be up to 200 km thick. The structure of the foreland crust is fixed and contains a 12-km-thick layer of lower mafic crust and a 24-km-thick layer of upper felsic crust with an additional sediment cover of differing thicknesses. By contrast, the thickness of the orogenic crust is varied between 36 km and 70 km. The thick orogenic crust could be produced by tectonic shortening during orogenesis in natural orogens such as the Tibetan plateau and the Central Andes (e.g., Holt & Wallace, 1990; Ramos et al., 2004). The range of sediment thickness in the foreland is 0-8 km, so we apply a 500-m-high grid resolution in the model to track the deformation of this thin sedimentary layer.

3.2.2 Material properties and boundary conditions

Material properties are taken from the published experimental studies and previous geodynamic models (Table 3.1). All materials contain fully visco-elasto-plastic rheology, and the ductile deformation mechanisms include diffusion, dislocation, and Peierls creep regimes. The laboratory-derived flow laws of wet quartzite (Qtz_{wet}; Gleason & Tullis, 1995), dry Maryland diabase (MD_{dry}; Mackwell et al., 1998), and wet/dry olivine (Ol_{wet}/Ol_{dry}; Hirth & Kohlstedt, 2003) are used for the felsic crust and its sediment cover, the mafic crust, and the lithospheric/sublithospheric mantle, respectively. Materials in the felsic crust undergo frictional-plastic strain-softening through a decrease in the friction coefficient from 0.5 to 0.1 over the accumulated strain of 0.5 to 1.5, including the friction angle from 30º to 6º and the cohesion from 20 MPa to 1 MPa (Table 3.1) based on the experience of previous geodynamic models (e.g., Sobolev & Babeyko, 2005; Sobolev et al., 2006).

The values of thermal parameters are within the range expected for crustal and mantle materials (e.g., Sobolev et al., 2006). Radiogenic heat production is 1.0 $\mu W\ m^{-3}$in the felsic crust and 0.3 $\mu W\ m^{-3}$ in the mafic crust. The thermal conductivity increases from 2.5 $W\ m^{-1}K^{-1}$ in the crust to 3.3 $W\ m^{-1}K^{-1}$ in the mantle to mimic the heat transportation by upper mantle convection without additional model convective motions (e.g., Pysklywec and Beaumont, 2004). Material density is temperature- and pressure-dependent (Table 3.1). The continental felsic crust has a reference density of 2800 $kg\ m^{-3}$ to reflect that it has a more felsic (silica-rich) composition than the mafic materials below. The density of sediments is 300 $kg\ m^{-3}$ less than the density of the continental felsic rocks at the same temperature. The reference density of the mantle (3300 $kg\ m^{-3}$) is consistent with the density of the fertile upper mantle (Poudjom Djomani et al., 2001).

The thermal-mechanical boundary conditions contain the top stress-free surface boundary with the temperature of 0°C and the closed free-slip bottom boundary with the temperature of 1460°C (Figure 3.1). The free surface stabilization approach (Kaus et al., 2010) is applied to the top boundary covered by the 10-km-thick low viscous and low density "sticky air" phase, which allows a relatively large integration time step. The thermal gradient at the side boundaries is taken to be zero, which means no horizontal heat flux. The right-hand (East) boundary moves westward with the velocity of 1 or 2 cm/year, producing total 100 km shortening in all models.

The material is allowed to flow out on the left-hand side boundary beneath the orogenic lithosphere to maintain the mass balance.

Table 3.1. Material properties in the numerical models.

Phase	Sediment; Felsic crust	Mafic crust	Lithospheric mantle	Asthenosphere
Density*, ρ_0 (kg m^{-3})	2500; 2800	3000	3300	3300
Heat expansion, α (K^{-1})	3.7e-5	2.7e-5	3e-5	3e-5
Specific heat, C_p (kJ$kg^{-1}K^{-1}$)	1.2	1.2	1.2	1.2
Heat conductivity, k (W $m^{-1}K^{-1}$)	2.5	2.5	3.3	3.3
Heat productivity, A (μW m^{-3})	1.0	0.3	0	0
Friction angle**, φ (°)	3; 30-6	30	30	30
Cohesion**, C_0 (MPa)	1; 20-1	40	40	40
Bulk, shear modulus, K, G (GPa)[1]	55, 36	63, 40	122, 74	122, 74
Creep pre-exponential factor, *Bd/Bn/Bp**** ($Pa^{-n}s^{-1}$)	-/8.57e-28/-	-/5.78e-27/-	1.5e-9/6.22e-16 /6.85e-67	1e-9/2.03e-15 /6.85e-67
Creep activation energy, *Ed/En/Ep**** (kJ mol^{-1})	-/223/-	-/485/-	375/480/540	335/480/540
Creep activation volume *Vd/Vn/Vp**** (cm^3mol^{-1})	-/0/-	-/0/-	5/11/0	4/11/0
Power law exponent[3], n	-/4/-	-/4.7/-	1/3.5/-	1/3.5/-

*Temperature- and pressure-dependent density: $\rho_{P,T} = \rho_0[1 - \alpha(T - T_0)][1 + \frac{P-P_0}{K}]$, where ρ_0 is the reference density at temperature T_0 and pressure P_0, K is the bulk modulus.

**Strain-softening in the felsic crust via a decrease in φ and C_0 over the accumulated strain of 0.5 to 1.5; the sediment is assumed to be initially weak if φ is 3° and C_0 is 1 MPa.

***Viscous creep includes diffusion (*Bd, Ed, Vd*), dislocation (*Bn, En, Vn*), and Peierls (*Bp, Ep, Vp*).

3.3 Model results

3.3.1 Reference model

In the reference model M1 (Figure 3.2), the orogen has the same lithospheric structure as the foreland, except for the 4-km-thick sedimentary layer above the foreland, which differs from the upper crust only by density. After 100 km shortening, the felsic crust in both the orogen and its foreland undergoes pure-shear shortening, resulting in distributed crustal thickening and surface uplift (Figure 3.2b). Figure 3.2c shows that the strain rate norm (square root of the second invariant of deviatoric strain rate) is homogeneously distributed from the surface to the basement at ~17 km depth, and thus a fully thick-skinned structure is formed in the foreland.

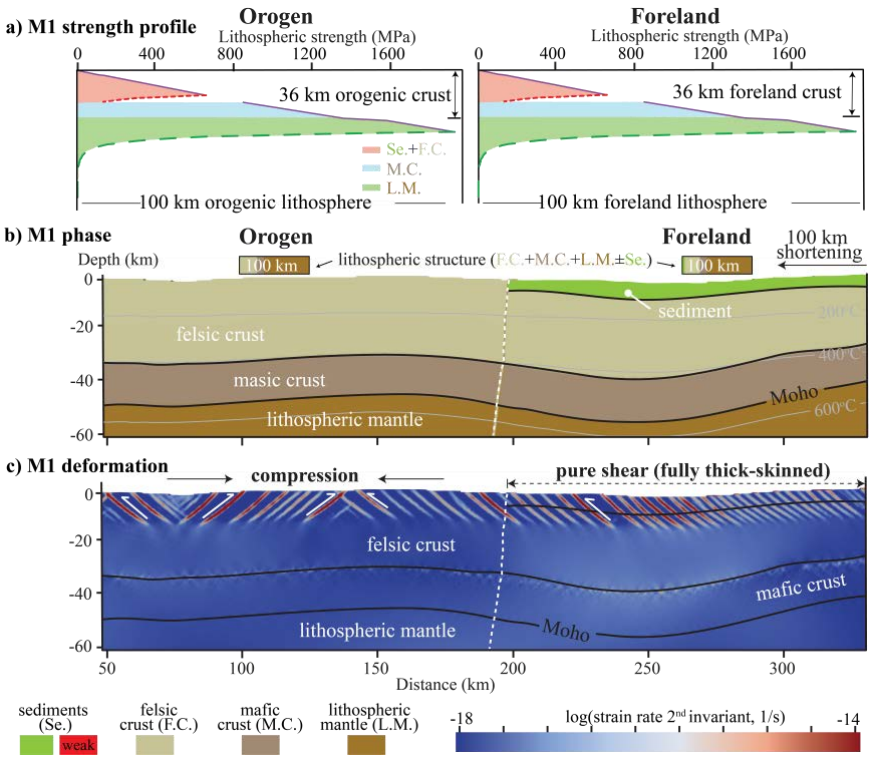

Figure 3.2. Reference model M1. **a)** Lithospheric strength profiles for both the orogen (left) and its foreland (right). **b)** and **c)** are model profiles of the phase and the deformation pattern after 100 km shortening, respectively. The two small boxes above the phase profile are lithospheric structures with the lithospheric thickness inside. The white dashed line is the boundary between the orogen and its foreland. The black line is the boundary between material phases. The white one-way arrows represent the fault direction. The black dashed line with two arrows represents the thick-skinned deformation in the foreland.

We conducted a series of modeling experiments that systematically investigate how the foreland deformation pattern (shortening mode and deformation structure) is affected by changes in lithospheric structure, crustal structure, and sediment strength (Figure 3.3). Below we examine the effect of each of the following factors: (i) thickness of orogenic lithosphere and orogenic crust, (ii) thickness of foreland lithosphere, (iii) friction coefficient of foreland sediments and thickness of foreland sediments, and (iv) their combinations on the deformation pattern.

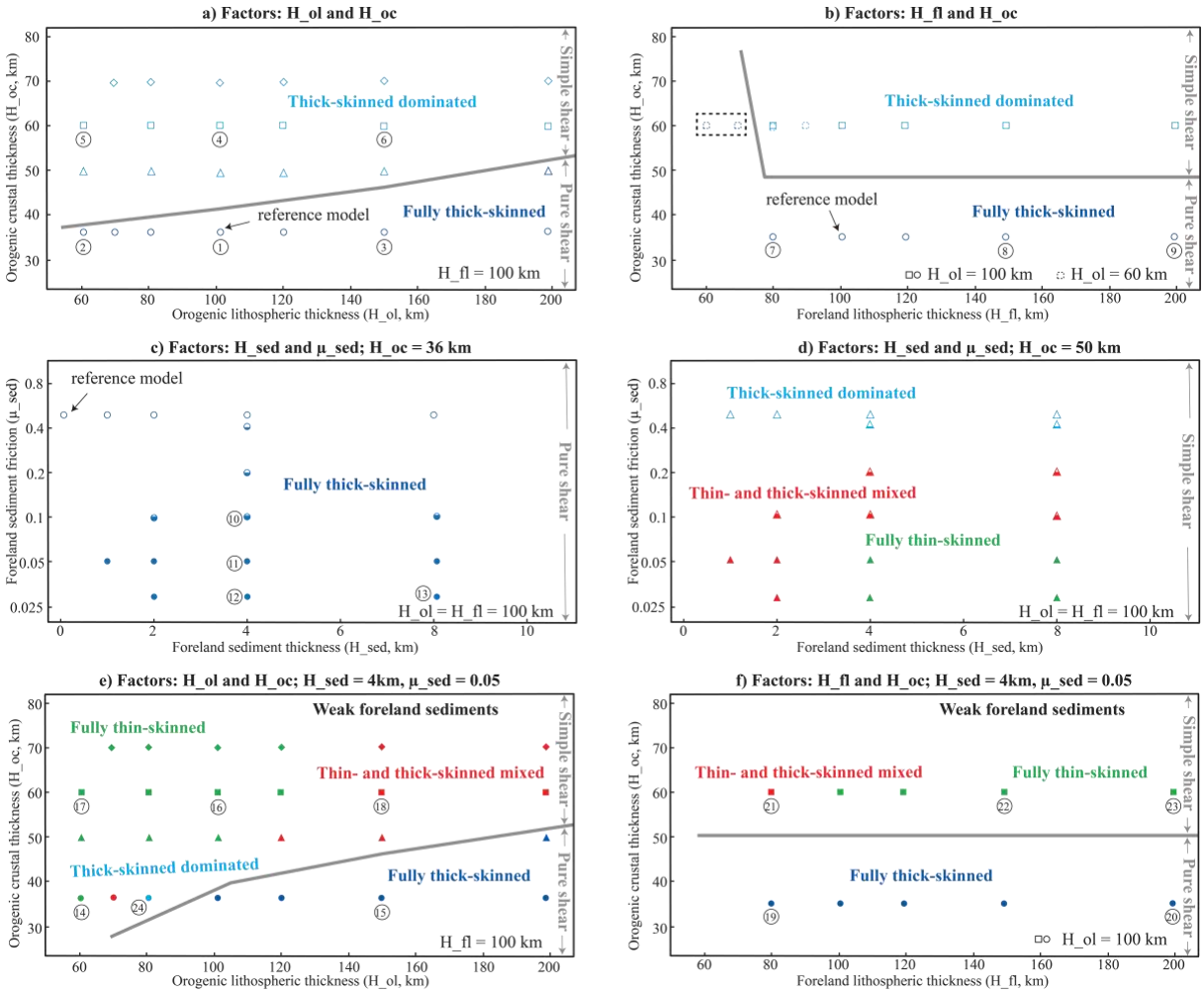

Figure 3.3. Model behaviors for variations in crustal thickness, lithospheric thickness, sediment thickness, and sediment friction coefficient. **a-b)** Models with changing factors: orogenic lithospheric thickness (H_ol), orogenic crustal thickness (H_oc), and foreland lithospheric thickness (H_fl). **c-d)** Models with changing factors: foreland sediment thickness (H_sed) and its friction coefficient (μ_sed), and H_oc. **e-f)** Models with changing factors: H_ol, H_oc, H_fl, and an initially weak foreland sediment layer. Models M1-M24 are illustrated by the number inside the black circle. The grey line shows the transition between two shortening modes.

3.3.2 Variations in orogenic and foreland lithospheric structures

3.3.2.1 Orogenic lithospheric thickness and orogenic crustal thickness

The strength of the continental lithosphere strongly depends on its lithospheric thickness and crustal thickness. First, we fix the thickness of the orogenic crust as in the reference model (36 km) and change the thickness of the orogenic lithosphere. Geological and geophysical observations indicate that the lithosphere under many active orogens (e.g., the Central Andes and the Himalayas) is thin or absent in the orogen-foreland compressional system. This is because the lithospheric mantle, being gravitationally unstable, is susceptible to removal via Rayleigh-Taylor-type instability (Molnar & Houseman, 2004) or delamination (Bird, 1979).

In Model M2 (Figure 3.3a, 3.4a), the orogenic lithosphere is as thin as 60 km and therefore weaker than the 100-km-thick foreland lithosphere. The model shows that the compressional deformation is localized within the orogen and its lithosphere is thickened after 100 km shortening. Simultaneously, a fully thick-skinned structure is formed in the foreland in pure-shear shortening mode. If the orogenic lithosphere is thicker and therefore stronger than the foreland lithosphere (for example, 150 km in Model M3), the shortening is concentrated in the foreland and produces a fully thick-skinned structure in the crust. Therefore, in the models where only the thickness of the orogenic lithosphere changes, while the crustal thickness in the orogen and its foreland remains the same, the foreland crust shortens in pure-shear mode accompanied by the fully thick-skinned deformation.

When the orogenic crust is thickened to 60 km (Models M4-M6 in Figure 3.3a, 3.4c-e), the foreland crust underthrusts beneath the orogen regardless of the thickness of the orogenic lithosphere within the range of parameters considered here. The shortening mode changes from pure-shear to simple-shear, and a narrow zone of the thin-skinned thrust in the foreland is formed. However, the contribution of the thin-skinned deformation to the total foreland crustal deformation is less than 10%, and thus we consider this type of deformation structure as thick-skinned dominated. The 60-km-thick orogenic lithosphere in Model M5 represents a thin lithosphere similar to the Puna plateau, where the lithospheric mantle was likely delaminated (e.g., Kay & Coira, 2009). In this model, the orogenic lithosphere is hotter and much weaker than in the other two Models M4 and M6. Compared to Models M4 and M6, the foreland upper crust in Model M5 underthrusts further towards the orogen, creating a larger viscous flow in the lower part of the thick felsic crust of the orogen and almost no deformation in its upper crust.

In all three models, a pronounced deep detachment zone is produced between the upper crust and lower crust in the foreland.

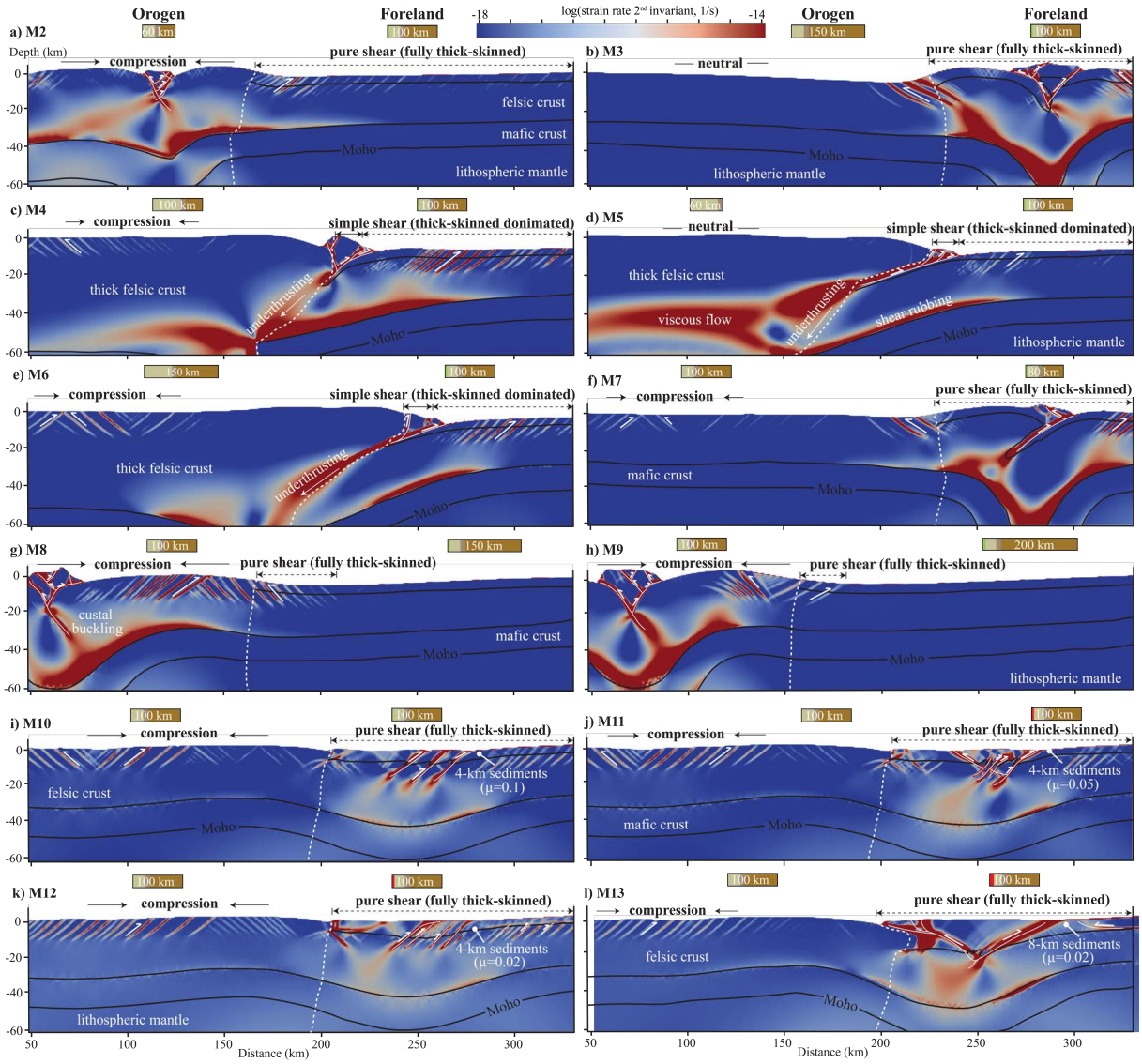

Figure 3.4. Foreland deformation patterns in Models M2-M13 with a different individual factor after 100 km shortening. **a-b**) Models M2 and M3 show the effect of H_ol. **c)** Model M4 shows the effect of H_oc. **d-e)** Models M5 and M6 include factors of H_ol and H_oc. **f-h)** Models M7-M9 show the effect of H_fl. **i-k**) Models M10-M12 show μ_sed in the 4-km-thick foreland sedimentary layer drops from 0.05 (in Model M1) to 0.1, 0.05, and 0.02, respectively. **l)** Models M13 contains μ_sed = 0.02 in the 8-km-thick sedimentary layer. Sediments are considered as initially weak, i.e., red part in the box of the foreland lithospheric structure, when the friction coefficient is not higher than 0.05. The solid black line with two arrows represents the thin-skinned deformation in the foreland. The white dashed line is the boundary between the orogen and its foreland.

3.3.2.2 Foreland lithospheric thickness

Here we test the effect of the foreland lithospheric strength on the deformation style by changing the thickness of the foreland lithosphere, while the initial crustal thicknesses in the foreland and orogen are fixed. When the foreland lithosphere is 20 km thinner and thus weaker than the orogenic lithosphere (Figure 3.4f), the deformation mode in the foreland is pure-shear with the fully thick-skinned structure - the same as in Model M3. Unlike in the mountain belts, the foreland lithosphere in the craton area can be thicker than 150 km. For example, the thermal lithosphere is >180 km thick under some foreland regions of the southwestern Canadian craton (e.g., Currie, 2016). In Models M8 and M9 (Figure 3.3b), the thickness of foreland cratonic lithosphere is not less than 150 km thick, and most of the tectonic shortening is concentrated in the orogenic crust, resulting in crustal buckling and surface uplift (Figure 3.4g-h). The fully thick-skinned structure is formed near the orogen-foreland boundary. As expected, the amount of foreland deformation decreases with thickening of foreland lithosphere.

3.3.2.3 Foreland sediment strength

In addition to the effect of lithospheric strength on the foreland deformation pattern, the foreland sediment mechanical strength (coefficient of friction) and its thickness are also important. Here we test the effect of the change of friction coefficient in sediments from 0.5 in the reference model M1 to 0.1-0.02 in Models M10-M12 (Figure 3.3c, 3.4i-k), which is the appropriate value of friction drop compared to previous geodynamic models (e.g., Sobolev et al., 2006). The foreland deformation in Model M10 is no longer homogenous as in the reference model; three pronounced thrust faults are produced in the middle part of the foreland. When the friction coefficient of sediments is further reduced (Models M11 and M12), the magnitude of deformation in the foreland increases, and the fault system becomes more complicated. Apparently, the sediment weakening due to the friction drop promotes the development of foreland deformation. However, the shortening mode in these models remains pure-shear. There is also no underthrusting of the foreland crust, and therefore the deformation structure is fully thick-skinned. If the sediment thickness increases, the deformation pattern is similar, but with fewer and deeper faults (Figure 3.4l).

3.3.2.4 The effects of multiple factors

None of the above models shows a wide zone of the fully thin-skinned deformation in the foreland. Here, we present models with the combination of multiple factors considered above. All of these models have the 4-km-thick sedimentary layer in the foreland with a friction coefficient of 0.05, and other model parameters are varied in the same way as in previous models. As we will see later, weak foreland sediments result in two additional deformation structures, namely thin- and thick-skinned mixed and fully thin-skinned. We deem the deformation structure to be mixed if it combines features of both thin- and thick-skinned structures and its thin-skinned thrust zone is significantly wider than the zone in the thick-skinned dominated structure.

Models shown in Figure 3.5a-f have the same initial lithospheric structures as in models in Figure 3.4a-f, but also include an initially 4-km-thick layer of weak sediments in the foreland. The weak sedimentary layer in most of the models facilitates the underthrusting of the foreland beneath the orogen and the formation of the mixed or fully thin-skinned deformation structure. Pronounced underthrusting and broad zones of the fully thin-skinned deformation form in models with a thick crust and thin lithosphere in the orogen and thick lithosphere in the foreland (M16, M17, M22, and M23). In all models with large foreland underthrusting the viscous flow is formed in the lower crust of the orogen resulting in orogenic crustal thickening and surface uplift. Interestingly, while the thick orogenic crust remains the main factor that facilitates foreland underthrusting, weak sediments can switch the deformation mode from pure-shear (Model M2) to simple-shear (Model M16), even if the orogenic crust is rather thin (initially 36 km thick in these models); but the orogenic lithosphere is thinner than the foreland lithosphere.

In the particular case of a thicker lithosphere in the orogen and the same crustal thickness in the orogen and its foreland, weak foreland sediments do not change the deformation pattern significantly (compare Models M3 and M7 with Models M17 and M21). In models with a thick orogenic crust and the orogenic lithosphere thicker than the foreland lithosphere, weak foreland sediments switch the deformation structure from thick-skinned dominated in Model M6 to thin- and thick-skinned mixed in Model M20. The thick-skinned deformation is not completely converted to thin-skinned in this model because the orogen is not sufficiently weaker than the foreland.

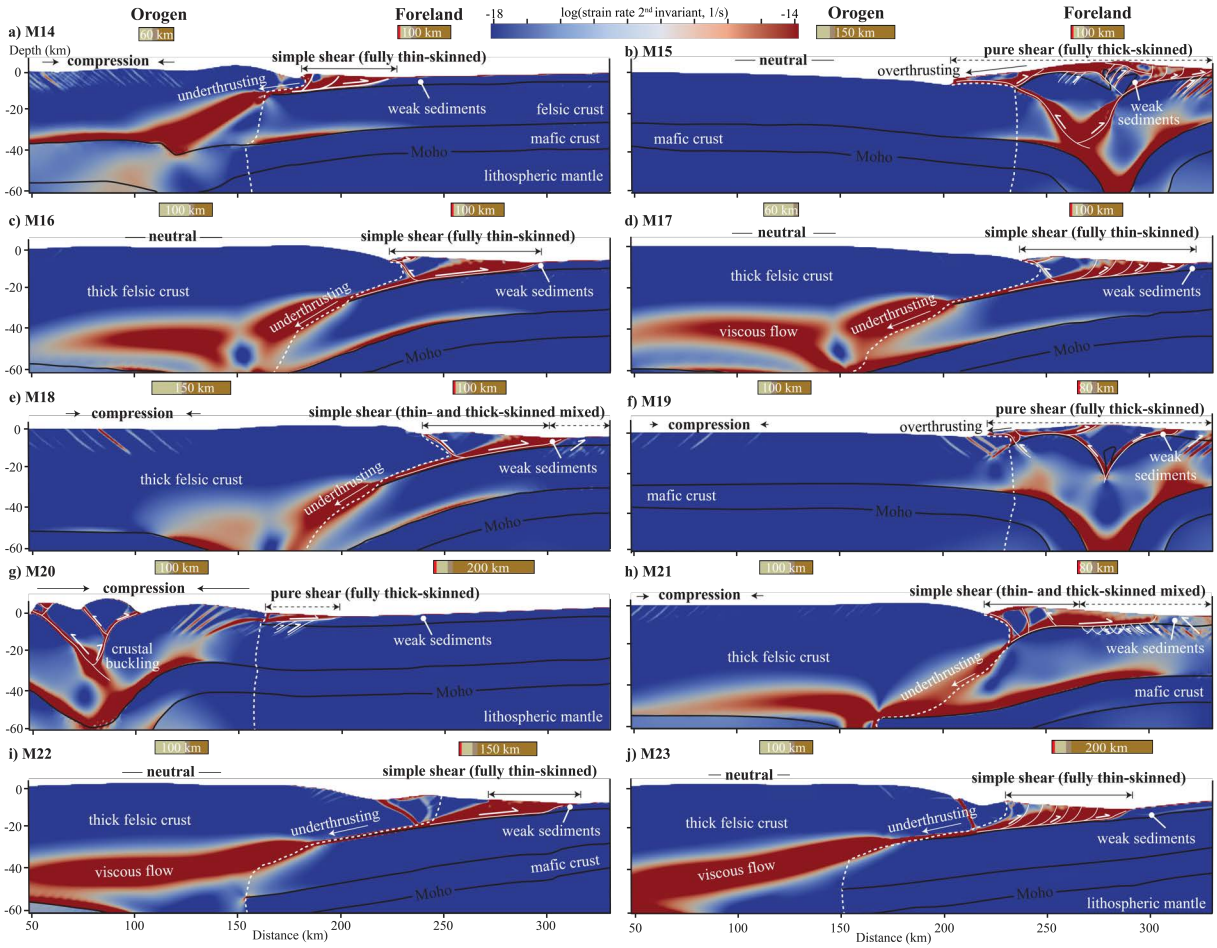

Figure 3.5. Foreland deformation patterns in Models M14-M23 with the combination of multiple factors. **a-g**) Models M14-M20 have the same initial lithospheric structures as in Models M2-M7 and M9, but with the weak sedimentary layer in the foreland. **h-j**) Models M21-M23 change the factor H_fl based on Model M16. The white dashed line is the boundary between the orogen and its foreland.

3.4 Discussion

3.4.1 Lithospheric strength analysis

For each model, we calculated initially integrated lithospheric strength of the orogen and its foreland as well as the strength ratio between them. The integrated strength is estimated through the integration of yield strength envelope (e.g., Tesauro et al., 2013) for initial lithospheric structure. Since the strength of the thin sedimentary layer has little effect on the lithospheric strength, we neglect the strength change caused by the weakening of foreland sediments during the calculation. More details about the calculation are presented in Appendix A.

As we will show below, modeled deformation styles are controlled by the difference in the lithospheric strength between the orogen and the foreland (Figure 3.6). We note, however, that the difference in the integrated strength of the entire lithosphere between the orogen and its foreland does not explain all model results. For example, the entire lithospheric strength of the orogen in Model M18, including a 150-km-thick orogenic lithosphere and a 60-km-thick orogenic crust, is higher than that in Model M24 with an 80-km-thick lithosphere and a 36-km-thick crust in the orogen (Figure A.1). Model M18 behaves in simple-shear shortening mode with thin- and thick-skinned mixed structure in the foreland.

As expected, when other parameters (i.e., lithospheric strength and foreland sediment strength) are fixed, and only the orogenic lithosphere is weaker than the foreland lithosphere, the foreland crust underthrusts beneath the orogen further and causes a larger amount of thin-skinned deformation (compare Model M16 to Models M17 and M18). However, the model behavior of M24 is contradictory to this view, where the deformation structure is thick-skinned dominated with a narrow thin-skinned wedge zone on the edge of foreland (Figure 3.3e).

Figure 3.6 shows that strength difference of the upper part of the lithosphere (e.g., top 40 km lithosphere) between the orogen and its foreland control the foreland deformation pattern better than the strength difference of entire lithosphere. With this new definition of lithospheric strength Model M24 has a higher strength ratio than Model M18 (Figure 3.6a), i.e., Model M24 has a stronger upper orogenic lithosphere than Model M18. As a result, less thin-skinned deformation is formed in Model M24.

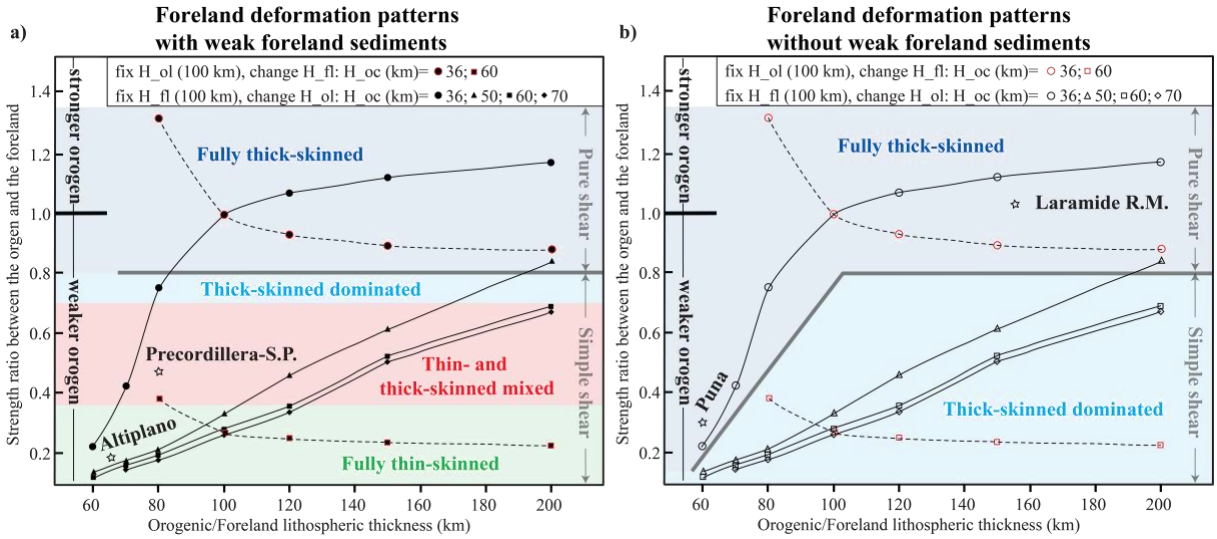

Figure 3.6. Foreland deformation patterns **a)** with or **b)** without weak foreland sediments. Four solid lines and two dashed lines represent the change of orogenic lithospheric thickness and the change of foreland lithospheric thickness, respectively. The orogen is stronger than the foreland as the ratio >1. The grey line is the boundary between pure-shear and simple-shear. Hollow stars indicate four natural systems with different foreland deformation patterns. R.M. – Rocky Mountains; S.P. – Sierras Pampeanas.

It is intuitively clear that if the lithospheric strength in the orogen and its foreland is similar (strength ratio 0.8-1.3 in Figure 3.6), then the foreland (and the orogen) should deform in pure-shear mode, and the deformation structure should be thick-skinned as is demonstrated by Figure 3.6a. Less obvious is simple-shear and thin-skinned foreland deformation at low strength ratio, i.e., when the orogenic lithosphere is much weaker than the foreland lithosphere. In this case, the intuitive scenario would be the localization of shortening in the weak orogen and not in the foreland. However, the strong foreland in our models behaves in two shortening modes with different deformation structures (Figure 3.6a). We infer that in addition to the lithospheric strength mentioned above, the gravitational potential energy (GPE) of the orogen also contributes to the foreland deformation pattern.

Generally, the compressive force driving the orogenic shortening (i.e., the mountain building) causes the thickening of the orogenic crust. During shortening, the force works against two mainly resistive forces, which are the mechanical strength (discussed in this study) and the gravity (e.g., Molnar & Lyon-Caen, 1988). The work against the gravity creates the gravitational potential energy. The GPE per unit surface of the Earth area in the orogen increases with crustal thickening. Thus, to shorten the orogen further, it requires an increasingly

larger amount of work from the driving force to overcome the increasing GPE. When the force can no longer supply the energy needed to elevate the orogen higher, the mountain range is likely to grow laterally in width instead of increasing in height and crustal thickness (Molnar & Lyon-Caen, 1988). Consequently, when the orogen grows laterally, the work done by the specified driving force will be used for deforming the orogenic edge and its foreland, even if the orogenic lithosphere is much weaker than the foreland lithosphere. In this case, the foreland lithosphere underthrusts beneath the edge of the orogen, i.e., the foreland shortening style is simple-shear (Figure 3.6). If there is a thick layer of mechanically weak sediments in foreland, then shear deformation is localized in the sedimentary layer and the foreland deformation pattern is thin-skinned (Figure 3.6a) and otherwise thick-skinned (Figure 3.6b).

3.4.2 Structural controls on the shortening mode and the deformation structure in the foreland

The results of our models demonstrate that the variation of orogenic strength caused by the change in the orogenic crustal thickness has the greatest effect on controlling the shortening mode (i.e., pure-shear or simple-shear). The pure-shear mode develops in models with little difference in crustal thickness between the orogen and the foreland (both are 36 km thick in this study), while the thickened orogenic crust is required to switch from pure-shear to simple-shear (Figure 3.6). The thickened orogenic crust causes the initially high GPE of the orogen and low strength of the upper part of lithosphere in the orogen. The high GPE in the orogen forces the tectonic shortening in the foreland while the thick and weak crust in the orogen allows the strong foreland lithosphere to intrude into it easily in simple-shear mode.

The other three individual factors (H_ol, H_fl, μ_sed and H_sed) have little effect on the transition from pure-shear to simple-shear with one exception. That is the case when the orogenic crust is much thicker (high GPE) than the foreland crust, and the foreland lithosphere is thin. In this particular case (the dashed rectangular in Figure 3.3b), the foreland lithosphere deforms in pure-shear mode instead of underthrusting under the orogen.

Our models show that significantly lower strength of the upper lithosphere in the orogen than in foreland (strength ratio < about 0.7), and the presence of a thick (about 4 km or thicker) layer of weak (friction coefficient about 0.05 or lower) foreland sediments are responsible for the thin-skinned deformation in the foreland. Conversely, if the orogenic lithosphere is stronger

than the foreland lithosphere or there are no thick and weak sediments in foreland, the deformation structure is fully thick-skinned or thick-skinned dominated (Figure 3.6). Furthermore, thick and weak sediments in foreland generally intensify simple-shear shortening by making underthrusting easier and thus broadening the thin-skinned deformation zone. In the case, when the orogenic crust is thick, and the foreland lithosphere is thin, the presence of thick and weak sediments in foreland can even switch foreland deformation from pure-shear to simple-shear mode.

3.4.3 Applications to natural orogen-foreland systems

3.4.3.1 Central Andes

In the Central Andes, the Altiplano-Puna plateau was formed with an N-S oriented deformation diversity, including a broad wedge-shaped thin-skinned thrust belt in the Interandean-Subandean zone and the thick-skinned structure in the Santa Barbara System (Figure 3.7a). The lithosphere under the plateau is very thin but the upper felsic crust is as thick as 50-70 km (e.g., Tassara et al., 2006). This is suggested to be the result of lithosphere delamination, which occurred during Cenozoic shortening (e.g., Kay & Kay, 1993; Beck & Zandt, 2002; Sobolev & Babeyko, 2005). The Puna plateau and its foreland area have a higher seismic attenuation, which implies a hotter and thinner lithosphere than the northern Altiplano part (Whitman et al., 1996). There are rich Paleozoic and Mesozoic sediments deposited in the Subandean zone, which pinch out southward to the Santa Barbara system (e.g., Allmendinger & Gubbels, 1996; Pearson et al., 2013). The local wet conditions in the foreland since late Cenozoic (Strecker et al., 2007) indicate that abundant fluids stored in these ancient sediments may weaken them by reducing their pore fluid pressure.

We applied these observations to the specific case of the Central Andes. In the models (Figure 3.7b-c), the thickness of the orogenic crust under the Altiplano-Puna plateau is 60 km and an additional 10-km-thick lithospheric mantle is attached to the Altiplano crust. The orogenic lithosphere under the Puna plateau only contains the thick crust due to the evidence of mantle lithosphere delamination. The lithosphere of the Puna foreland in the model is 70-km-thick while the foreland lithosphere in the Altiplano part is 30 km thicker than the Puna foreland lithosphere. In agreement with observations, the weak sedimentary layer in the model covers only the north Altiplano foreland crust (Figure 3.7b). Model results clearly show that simple-shear with a fully thin-skinned thrust and pure-shear with a fully thick-skinned structure are

formed in the Altiplano foreland and the Puna foreland, respectively. Our models support and specify the results of a previous relatively low-resolution modeling study (Babeyko & Sobolev, 2005). For instance, in addition to the previous study, our model reproduces observed east-dipping reverse faults in the foreland edge in both cases.

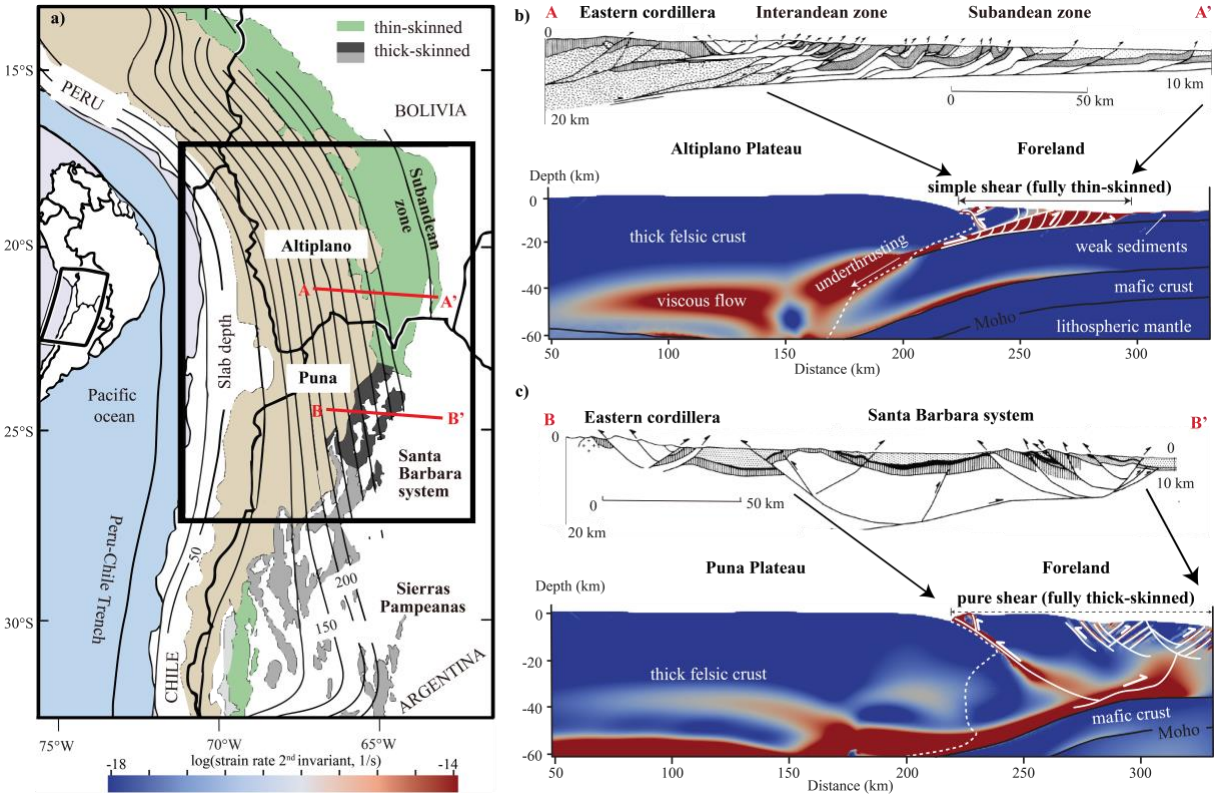

Figure. 3.7. Numerical models with application to the case of the Central Andes. **a)** The left map is modified from Kay & Coira (2009). Geological structures of two cross-sections A-A' and B-B' are modified from Kley et al. (1999), showing **b)** fully thin-skinned deformation in the Interandean - Subandean zone and **c)** fully thick-skinned deformation in the Santa Barbara system. The white dashed line is the boundary between the plateau and its foreland.

3.4.3.2 Laramide Province

The Laramide province (i.e., the Rocky Mountain foreland adjacent to the Colorado Plateau) is a widely thick-skinned deformed province. More than 100 km pure-shear shortening in this province characterizes the Laramide orogenic event from the Late Cretaceous to Paleocene, which is coeval with the period of flat-slab subduction of the Farallon plate. The formation of the Laramide province is suggested to be the result of this flat subduction process, where the flat-slab drives horizontal stresses to deform the plateau-foreland system (e.g., Bird 1984). As

the Colorado Plateau is a strong block before the Laramide shortening, the deformation is minor in the plateau and mainly distributed in the Rocky Mountain foreland (e.g., Spencer, 1996; Humphreys, 2009). The xenolith-based observations estimate the thickness of the pre-Laramide lithosphere of the Colorado Plateau to be more than 150 km due to its underlying cold, refractory mantle root (e.g., Smith & Griffin, 2005; Li et al., 2008). Previous numerical studies of flat subduction suggest that the Colorado Plateau may be thicker and thus stronger than its foreland cratonic lithosphere due to its deep cratonic root (e.g., O'Driscoll et al., 2009; Liu & Currie, 2016). The foreland was formerly part of a continental platform with an approximately 33-km-thick crust before the Laramide orogeny (Bird, 1984). The difference in crustal thickness between the Colorado Plateau and its foreland is less than 5 km (Das & Nolet, 1998).

The results of our models, where the orogenic lithosphere is thicker and stronger than the foreland lithosphere, agree with the observed deformation pattern in the Laramide province. In the models, if their crust structure is not much different and the strength of the upper lithosphere of the orogen is slightly greater than that of foreland, the foreland is subjected to pure-shear shortening with fully thick-skinned structure (e.g., Models M3 and M15 and the hollow star of Laramide R.M. in Figure 3.6b), and there is minor deformation in the plateau.

3.4.3.3 Southern Canadian Rocky Mountains

The foreland deformation belt of the western North American Cordillera is a good example of an intra-plate shortening belt (Figure 3.8a). The mechanics of these belts are debated all the time and one hypothesis is that some Cordilleran foreland thrust and fold belts in the Southwestern Canadian Cordillera are the result of Late Cretaceous intraplate collision (Figure 3.8b; Johnston, 2008). This interpretation is supported by a recent study of Chen et al. (2019), which shows the seismic evidence for mantle suture and the collision origin between the Cordillera ribbon continent and the North American craton.

The southern Canadian Rocky Mountains at the latitude of Calgary, Alberta are considered as an archetypal thin-skinned belt (e.g., Price 1981; Stockmal et al. 2007). The surface of the underlying Archean to Early Proterozoic crystalline basement exhibits little to no relief at the scale of the belt. The sediment cover above the basement dips SW toward the Cordilleran orogen with a thickness of more than 8 km at the western ranges close to the Rocky Mountain trench and a thickness of several hundred meters at the eastern region of Foothills (Stockmal et al., 2007). The thickness of the lithosphere has the steep step from the Cordilleran orogen with

~60 km due to the lithosphere delamination to the eastward cratonic foreland with more than 150 km for at least 50-100 Ma (Bao et al., 2014; Currie and van Wijk, 2016). Although the observed average elevation is as high as 1.1km in the western Canadian Cordillera, the orogenic crust is not as thick as that in other mountain belts - such as the Tibetan Plateau with high topography - and it has little difference from the craton crust in foreland (Currie, 2016).

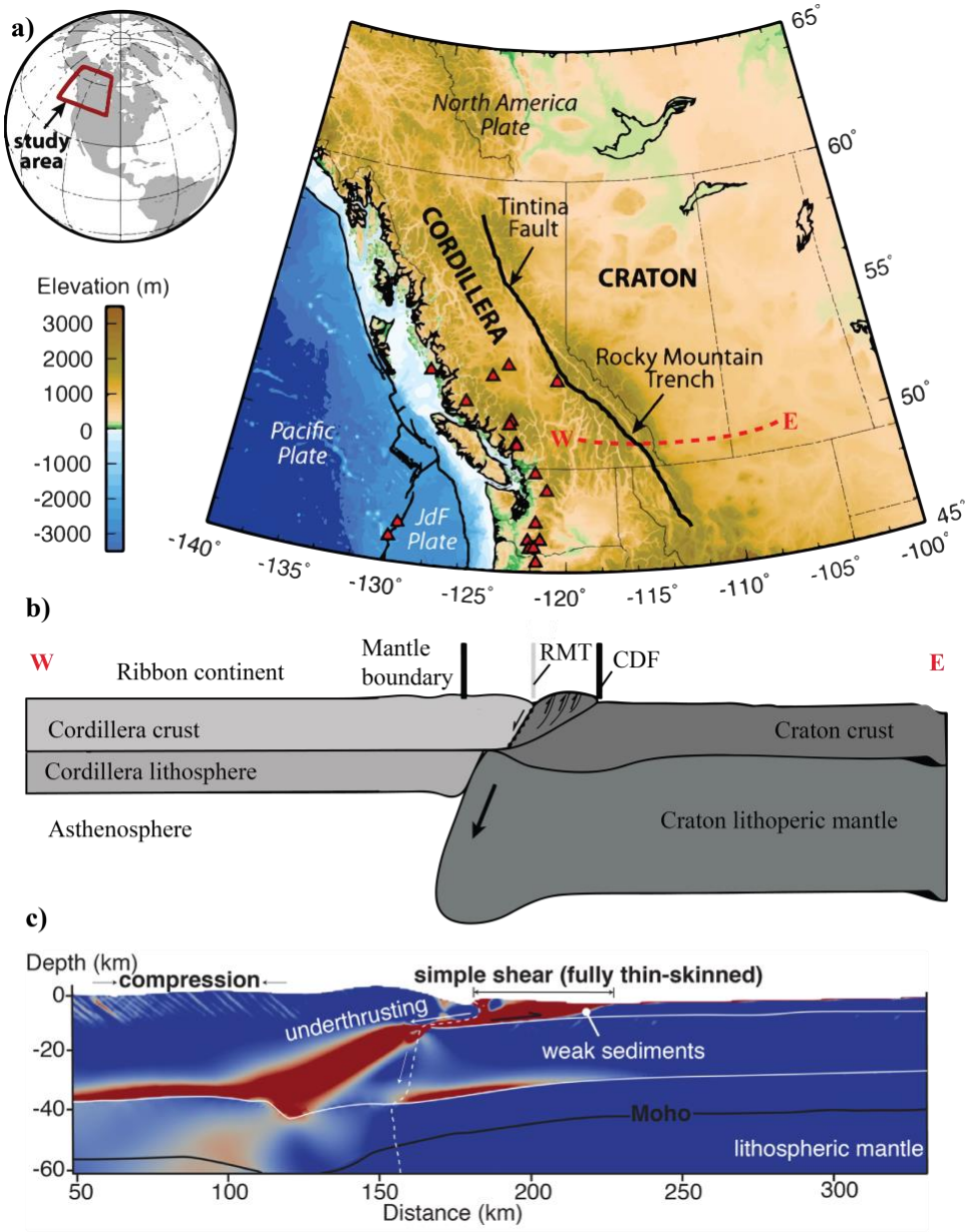

Figure. 3.8. Numerical models with application to the case of the southern Canadian Rocky Mountains. **a)** Surface topography in western Canada with active volcanoes (red triangles), modified from Currie (2016). JdF is Juan de Fuca. **b)** The continental collision model that forms the Cordillera-craton boundary (the W-E cross-section), modified from Chen et al. (2019). **c)** A first-order support to collision hypothesis from one numerical model in this study.

In the numerical model with 60-km-thick orogenic lithosphere and 150-km-thick foreland craton, the integrated strength ratio at top 40 km is about 0.19, and the deformation pattern belongs to the fully thin-skinned deformation (Figure 3.8c). Therefore, the model result could support the tectonic observation of thin-skinned belt and the collision hypothesis in western Canada.

3.4.3.4 Precordillera-Sierras Pampeanas

The province of the Sierras Pampeanas on the eastern side of the Precordillera thin-skinned thrust belts is considered as a modern analog of deformation in the Laramide province (e.g., Jordan & Allmendinger, 1986; Ramos & Folguera, 2009). The deformation structure of the Precordillera-Sierras Pampeanas foreland region, which is adjacent to the Frontal Cordillera of the Southern Andean Mountains, can be roughly considered to be a thin- and thick-skinned mixed deformation (Figure 3.7a). The flat-slab below the Frontal Cordillera stays at 100 km depth, and thus, the lithosphere of the Frontal Cordillera should be less than 100 km thick (e.g., Ramos & Folguera, 2009). The lithospheric thickness increases eastward to the foreland area and reaches more than 150 km in the Sierras Pampeanas. The crustal thickness is more than 60 km under the Frontal Cordillera and rapidly decreases eastward to less than 40 km below its foreland (e.g., Ramos et al., 2004).

Furthermore, there are abundant Paleozoic sedimentary rocks in the Precordillera whereas only a small amount of Cenozoic sediments covers the Sierras Pampeanas (e.g., Ramos et al., 2004; Mescua et al., 2016; Meeßen et al., 2018). Our models with constraints from these observations suggest that the simple-shear shortening should occur in the foreland, accompanied by a mixed deformation consisting of the thin-skinned thrust at the foreland edge and the thick-skinned structure behind it (hollow star of Precordillera-Sierras Pampeanas in Figure 3.6a). This result is consistent with the observed deformation pattern in the Precordillera-Sierras Pampeanas region.

3.5 Conclusions

With high-resolution 2D thermomechanical numerical models, we systematically examine the effects of the lithospheric structure and strength on foreland deformation of the orogen subjected to the tectonic shortening.

We find that three factors control the shortening mode (pure-shear or simple-shear) and the deformation structure (thick-skinned or thin-skinned): (i) the strength difference in the upper part (40 km in this study) of the lithosphere between the orogen and its foreland, rather than the difference in the entire lithospheric strength between them; (ii) GPE of the orogen that is in turn controlled by its crustal thickness and lithospheric thickness, and (iii) the strength and thickness of the deforming foreland sediments.

If the strength of the upper part of the lithosphere of the orogen is higher or similar to that of foreland (strength ratio >0.8) and the orogenic crust is not much thicker than the foreland crust (relatively low GPE of orogen), the pure-shear shortening develops in the foreland.

If the strength of the upper part of the lithosphere of the orogen is significantly lower than that of the foreland (strength ratio <0.7) and the orogenic crust is much thicker than the foreland crust (>50 km causing relatively high GPE of the orogen), the simple-shear shortening develops in the foreland.

In the particular case of the thick orogenic crust (>50 km, high GPE) and the thin (<70 km) orogenic lithosphere, and simultaneously thin (<70-80 km) foreland lithosphere, the foreland deformation mode is pure-shear (Puna-Santa Barbara system case).

The fully thin-skinned or thin- & thick-skinned mixed structures in the foreland can develop only if thick (about 4 km or higher) and mechanically weak (friction coefficient about 0.05 or lower) sediments are present and the foreland shortening develops in simple-shear mode. The most pronounced thin-skinned deformation structure develops in the thick layer of weak sediments when the strength of the orogenic upper lithosphere is much lower than that of foreland upper lithosphere (strength ratio <0.3-0.4; Altiplano-Subandean ranges case).

Our modeling results reproduce natural examples including foreland deformation in the Central and Southern Andes in South America and foreland deformation in the Laramide Province and the Canadian Cordillera in North America.

Appendix A: Geodynamic governing equations and yield strength envelope

The material deformation is governed by solving the coupled system of momentum (1), mass (2), and energy (3) conservation equations below:

$$\frac{\partial \tau_{ij}}{\partial x_j} - \frac{\partial P}{\partial x_i} + \rho g_i = 0 \quad (1)$$

$$\frac{1}{K}\frac{DP}{Dt} - \alpha \frac{DT}{Dt} + \frac{\partial v_i}{\partial x_i} = 0 \quad (2)$$

$$\rho C_p \frac{DT}{Dt} = \frac{\partial}{\partial x_i}\left(k \frac{\partial T}{\partial x_i}\right) + \tau_{ij}\left(\dot{\varepsilon}_{ij}^{v} + \dot{\varepsilon}_{ij}^{p}\right) + A \quad (3)$$

where *i, j* represent spatial directions following Einstein summation convention, $x_{i,j}$ is the Cartesian coordinate, τ_{ij} is the deviatoric stress tensor, P pressure, ρ is the density, g_i is the gravitational acceleration vector, $v_{i,j}$ is the velocity, D/Dt is the material time derivative, K is bulk modulus, α is the thermal expansion coefficient, C_p is the specific heat, k is the thermal conductivity, A is the radiogenic heat production, and $\dot{\varepsilon}_{ij}^{v}, \dot{\varepsilon}_{ij}^{p}$ are viscous and plastic strain-rate deviators, respectively. These basic geodynamic equations are discretized in space (and time) using the finite-difference staggered grid method and solved assuming plane strain, incompressibility, and neglecting thermal diffusion.

The material behaves the frictional-plastic deformation when the deviatoric stress exceeds the plastic yield stress, which follows a pressure-dependent Drucker-Prager yield criterion:

$$\tau_Y = P sin\varphi + C_0 cos\varphi \quad (4)$$

where φ is the internal friction angle and C_0 is the cohesion. Below this yield stress, materials deform viscously with an effective viscosity (η_{eff}) given by:

$$\eta_{eff} = \frac{1}{2B^{\frac{1}{n}}} \dot{\varepsilon}_{II}^{\frac{(1-n)}{n}} exp\left(\frac{E+PV}{nRT}\right) \quad (5)$$

where $\dot{\varepsilon}_{II} = \sqrt{\frac{1}{2}\dot{\varepsilon}_{ij}\dot{\varepsilon}_{ij}}$ is the second invariant of the deviatoric strain rate, $\dot{\varepsilon}_{ij} = \frac{1}{2}\left(\frac{\partial v_i}{\partial x_j} + \frac{\partial v_j}{\partial x_i}\right)$, R is the gas constant. B, n, E, V are the pre-exponential viscosity parameter, stress exponent, activation energy and activation volume, respectively, of the corresponding three creep mechanisms (i.e., diffusion, dislocation, and Peierls) from laboratory experiments.

Integrated strength of the lithosphere (σ_L under compression is estimated from the yield strength envelope (YSE), which has been used in previous studies (e.g., Tesauro et al., 2013):

$$\sigma_L = \int_0^h (\sigma_1 - \sigma_3)dz = \int_0^h min\,(\sigma_B, \sigma_D)dz \quad (6)$$

where h is the lithospheric thickness and σ_1 and σ_3 are the maximum and minimum principal stress components, respectively. Figure A.1 shows initial strength envelopes of the lithosphere with different structures. There are two different types in the envelope: the frictional brittle strength (σ_B; the solid purple line in Figure A.1) and the ductile strength (σ_D; colored dashed curves in Figure A.1). The brittle strength is estimated by Byerlee's law (Byerlee, 1978): $\sigma_B = \int_0^h 2\mu\left(\sqrt{\mu^2+1} + \mu\right)\rho g(1-\lambda)dz$, where μ is the friction coefficient, $\lambda = \frac{P_p}{P_l}$ is the ratio between the pore fluid pressure P_p and the lithostatic pressure P_l. The ductile strength is a function of not only pressure and temperature but also rock types: $\sigma_D = \left(\frac{\dot{\varepsilon}_{ref}}{B}\right)^{\frac{1}{n}} exp\left(\frac{E+PV}{nRT}\right)$, where $\dot{\varepsilon}_{ref}$ is the initial reference strain rate ($10^{-16}\mathrm{s}^{-1}$).

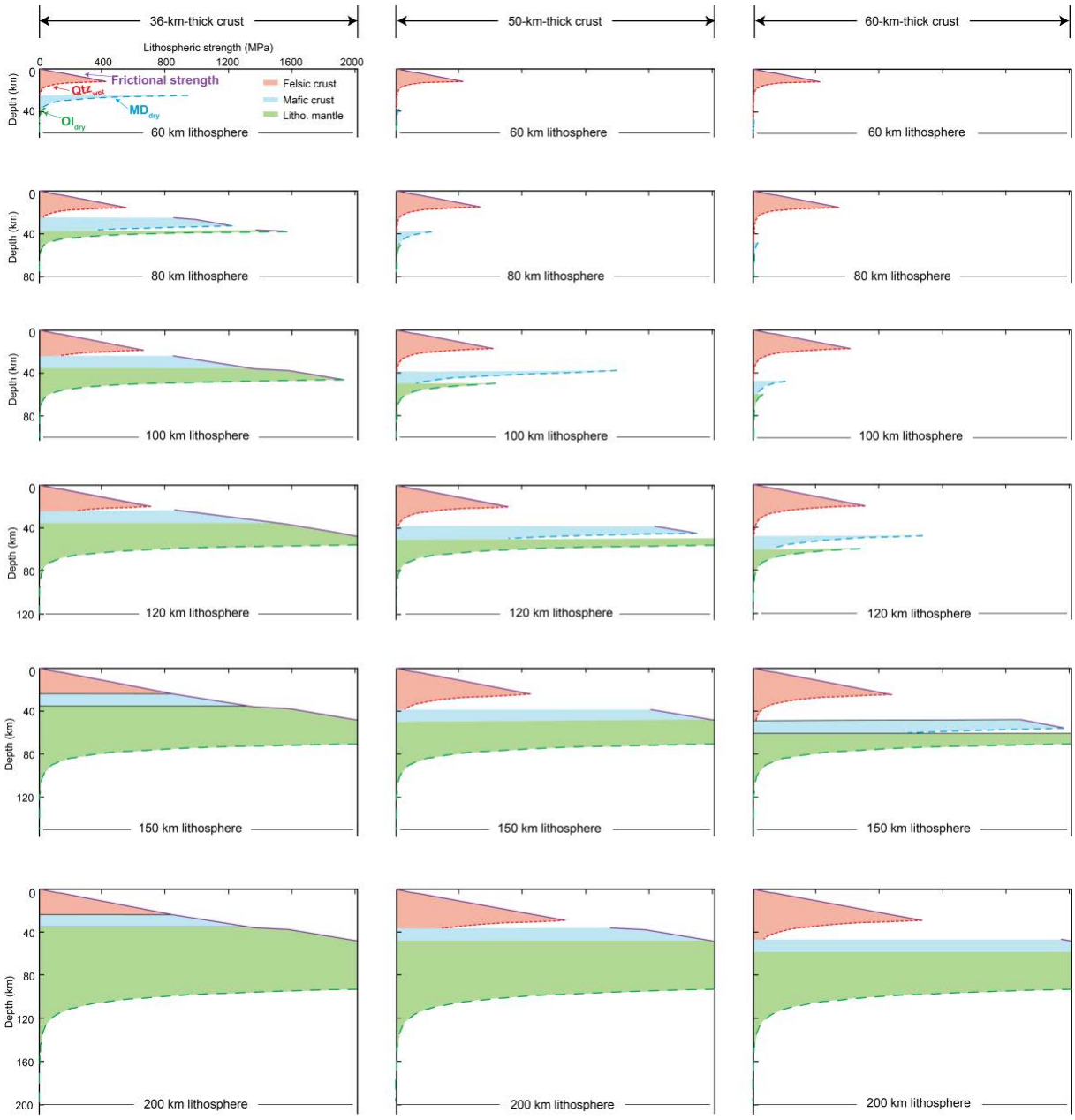

Figure A.1. The list of strength profiles with different initial lithospheric structures (60-200 km) and crustal structures (36km, 50 km, 60 km).

References

Afonso, J. C., & Ranalli, G. (2004). Crustal and mantle strengths in continental lithosphere: is the jelly sandwich model obsolete? *Tectonophysics*, *394*(3), 221–232. https://doi.org/10.1016/j.tecto.2004.08.006

Allmendinger, R. W., & Gubbels, T. (1996). Pure and simple-shear plateau uplift, Altiplano-Puna, Argentina and Bolivia. *Tectonophysics*, *259*(1), 1–13. https://doi.org/10.1016/0040-1951(96)00024-8

Babeyko, A. Y., & Sobolev, S. V. (2005). Quantifying different modes of the late Cenozoic shortening in the central Andes. *Geology*, *33*(8), 621–624. https://doi.org/10.1130/G21126AR.1

Babeyko, A. Y., Sobolev, S. V., Vietor, T., Oncken, O., & Trumbull, R. B. (2006). Numerical Study of Weakening Processes in the Central Andean Back-Arc. In O. Oncken, G. Chong, G. Franz, P. Giese, H.-J. Götze, V. A. Ramos, et al. (Eds.), *The Andes* (pp. 495–512). Springer Berlin Heidelberg. Retrieved from http://link.springer.com/10.1007/978-3-540-48684-8_24

Bao, X., Eaton, D. W., & Guest, B. (2014). Plateau uplift in western Canada caused by lithospheric delamination along a craton edge. *Nature Geoscience*, *7*(11), 830–833. https://doi.org/10.1038/ngeo2270

Beck, S. L., & Zandt, G. (2002). The nature of orogenic crust in the central Andes: NATURE OF OROGENIC CRUST. *Journal of Geophysical Research: Solid Earth*, *107*(B10), ESE 7-1-ESE 7-16. https://doi.org/10.1029/2000JB000124

Bird, P. (1979). Continental delamination and the Colorado Plateau. *Journal of Geophysical Research: Solid Earth*, *84*(B13), 7561–7571. https://doi.org/10.1029/JB084iB13p07561

Bird, P. (1984). Laramide crustal thickening event in the Rocky Mountain Foreland and Great Plains. *Tectonics*, *3*(7), 741–758. https://doi.org/10.1029/TC003i007p00741

Burov, E.B., & Watts, A. B. (2006). The long-term strength of continental lithosphere: “jelly sandwich” or “crème brûlée”? *GSA Today*, *16*(1), 4. https://doi.org/10.1130/1052-5173(2006)016<4:TLTSOC>2.0.CO;2

Burov, Evgene B. (2011). Rheology and strength of the lithosphere. *Marine and Petroleum Geology*, *28*(8), 1402–1443. https://doi.org/10.1016/j.marpetgeo.2011.05.008

Byerlee, J. (1978). Friction of rocks. *Pure and Applied Geophysics*, *116*(4–5), 615–626. https://doi.org/10.1007/BF00876528

Chen, Y., Gu, Y. J., Currie, C. A., Johnston, S. T., Hung, S.-H., Schaeffer, A. J., & Audet, P. (2019). Seismic evidence for a mantle suture and implications for the origin of the Canadian Cordillera. *Nature Communications*, *10*(1), 2249. https://doi.org/10.1038/s41467-019-09804-8

Cobbold, P. R., Mourgues, R., & Boyd, K. (2004). Mechanism of thin-skinned detachment in the Amazon Fan: assessing the importance of fluid overpressure and hydrocarbon generation. *Marine and Petroleum Geology*, *21*(8), 1013–1025. https://doi.org/10.1016/j.marpetgeo.2004.05.003

Collignon, M., Fernandez, N., & Kaus, B. J. P. (2015). Influence of surface processes and initial topography on lateral fold growth and fold linkage mode. *Tectonics*, *34*(8), 2015TC003843. https://doi.org/10.1002/2015TC003843

Currie, C. A. (2016). The Deep Roots of the Rocky Mountains: Geophysical Studies of Western Canada. *Journal of Student Science and Technology*, *9*(1). https://doi.org/10.13034/jsst.v9i1.142

Currie, C. A., & van Wijk, J. (2016). How craton margins are preserved: Insights from geodynamic models. *Journal of Geodynamics*, *100*, 144–158. https://doi.org/10.1016/j.jog.2016.03.015

Dahlen, F. A. (1990). Critical Taper Model of Fold-And-Thrust Belts and Accretionary Wedges. *Annual Review of Earth and Planetary Sciences*, *18*(1), 55–99. https://doi.org/10.1146/annurev.ea.18.050190.000415

Das, T., & Nolet, G. (1998). Crustal thickness map of the western United States by partitioned waveform inversion. *Journal of Geophysical Research: Solid Earth*, *103*(B12), 30021–30038. https://doi.org/10.1029/98JB01119

Gao, X., & Wang, K. (2014). Strength of stick-slip and creeping subduction megathrusts from heat flow observations. *Science*, *345*(6200), 1038–1041. https://doi.org/10.1126/science.1255487

Giambiagi, L., Mescua, J., Bechis, F., Martínez, A., & Folguera, A. (2011). Pre-Andean deformation of the Precordillera southern sector, southern Central Andes. *Geosphere*, *7*(1), 219–239. https://doi.org/10.1130/GES00572.1

Gleason, G. C., & Tullis, J. (1995). A flow law for dislocation creep of quartz aggregates determined with the molten salt cell. *Tectonophysics*, *247*(1), 1–23. https://doi.org/10.1016/0040-1951(95)00011-B

Hassani, R., Jongmans, D., & Chéry, J. (1997). Study of plate deformation and stress in subduction processes using two-dimensional numerical models. *Journal of Geophysical Research: Solid Earth*, *102*(B8), 17951–17965. https://doi.org/10.1029/97JB01354

Hirth, G., & Kohlstedt, D. (2003). Rheology of the upper mantle and the mantle wedge: A view from the experimentalists. *Washington DC American Geophysical Union Geophysical Monograph Series*, *138*, 83–105. https://doi.org/10.1029/138GM06

Holt, W. E., & Wallace, T. C. (1990). Crustal thickness and upper mantle velocities in the Tibetan Plateau Region from the inversion of regional Pnl waveforms: Evidence for a thick upper mantle lid beneath southern Tibet. *Journal of Geophysical Research: Solid Earth*, *95*(B8), 12499–12525. https://doi.org/10.1029/JB095iB08p12499

Humphreys, E. (2009). Relation of flat subduction to magmatism and deformation in the western United States. *Geological Society of America Memoirs*, *204*(0), 85–98. https://doi.org/10.1130/2009.1204(04)

Johnston, S. T. (2008). The Cordilleran Ribbon Continent of North America. *Annual Review of Earth and Planetary Sciences*, *36*(1), 495–530. https://doi.org/10.1146/annurev.earth.36.031207.124331

Jordan, T. E., & Allmendinger, R. W. (1986). The Sierras Pampeanas of Argentina; a modern analogue of Rocky Mountain foreland deformation. *American Journal of Science*, *286*(10), 737–764. https://doi.org/10.2475/ajs.286.10.737

Kaus, B. J. P., Mühlhaus, H., & May, D. A. (2010). A stabilization algorithm for geodynamic numerical simulations with a free surface. *Physics of the Earth and Planetary Interiors*, *181*(1–2), 12–20. https://doi.org/10.1016/j.pepi.2010.04.007

Kaus, B. J. P., Popov, A. A., Baumann, T. S., Pusok, A. E., Bauville, A., Fernandez, N., & Collignon, M. (2016). Forward and inverse modelling of lithospheric deformation on geological timescales. *NIC Symposium 2016 - Proceedings*, *48*, 299–307.

Kay, R. W., & Kay, S. M. (1993). Delamination and delamination magmatism. *Tectonophysics*, *219*(1), 177–189. https://doi.org/10.1016/0040-1951(93)90295-U

Kay, S. M., & Coira, B. L. (2009). Shallowing and steepening subduction zones, continental lithospheric loss, magmatism, and crustal flow under the Central Andean Altiplano-Puna plateau. *Geological Society of America Memoirs*, *204*, 229–259. https://doi.org/10.1130/2009.1204(11)

Kley, J., Monaldi, C. R., & Salfity, J. A. (1999). Along-strike segmentation of the Andean foreland: causes and consequences. *Tectonophysics*, *301*(1–2), 75–94. https://doi.org/10.1016/S0040-1951(98)90223-2

Kohlstedt, D. L., Evans, B., & Mackwell, S. J. (1995). Strength of the lithosphere: Constraints imposed by laboratory experiments. *Journal of Geophysical Research: Solid Earth*, *100*(B9), 17587–17602. https://doi.org/10.1029/95JB01460

Lacombe, O., & Bellahsen, N. (2016). Thick-skinned tectonics and basement-involved fold–thrust belts: insights from selected Cenozoic orogens. *Geological Magazine*, *153*(5–6), 763–810. https://doi.org/10.1017/S0016756816000078

Laske, G., Masters, T. G., Ma, Z., & Pasyanos, M. E. (2013). Update on CRUST1.0: A 1-degree Global Model of Earth's Crust.

Li Zheng-Xue Anser, Lee Cin-Ty A., Peslier Anne H., Lenardic Adrian, & Mackwell Stephen J. (2008). Water contents in mantle xenoliths from the Colorado Plateau and vicinity: Implications for the mantle rheology and hydration-induced thinning of continental lithosphere. *Journal of Geophysical Research: Solid Earth*, *113*(B9). https://doi.org/10.1029/2007JB005540

Liu, S., & Currie, C. A. (2016). Farallon plate dynamics prior to the Laramide orogeny: Numerical models of flat subduction. *Tectonophysics*, *666*, 33–47. https://doi.org/10.1016/j.tecto.2015.10.010

Mackwell, S. J., Zimmerman, M. E., & Kohlstedt, D. L. (1998). High-temperature deformation of dry diabase with application to tectonics on Venus. *Journal of Geophysical Research: Solid Earth*, *103*(B1), 975–984. https://doi.org/10.1029/97JB02671

Meeßen, C., Sippel, J., Scheck-Wenderoth, M., Heine, C., & Strecker, M. R. (2018). Crustal Structure of the Andean Foreland in Northern Argentina: Results From Data-Integrative Three-Dimensional Density Modeling. *Journal of Geophysical Research: Solid Earth*. https://doi.org/10.1002/2017JB014296

Mescua, J. F., Giambiagi, L., Barrionuevo, M., Tassara, A., Mardonez, D., Mazzitelli, M., & Lossada, A. (2016). Basement composition and basin geometry controls on upper-crustal deformation in the Southern Central Andes (30–36°S). *Geological Magazine*, *153*(5–6), 945–961. https://doi.org/10.1017/S0016756816000364

Molnar, P., & Houseman, G. A. (2004). The effects of buoyant crust on the gravitational instability of thickened mantle lithosphere at zones of intracontinental convergence.

Geophysical Journal International, *158*(3), 1134–1150. https://doi.org/10.1111/j.1365-246X.2004.02312.x

Molnar, P., & Lyon-Caen, H. (1988). Some simple physical aspects of the support, structure, and evolution of mountain belts. In *Geological Society of America Special Papers* (Vol. 218, pp. 179–208). Geological Society of America. https://doi.org/10.1130/SPE218-p179

O'Driscoll, L. J., Humphreys, E. D., & Saucier, F. (2009). Subduction adjacent to deep continental roots: Enhanced negative pressure in the mantle wedge, mountain building and continental motion. *Earth and Planetary Science Letters*, *280*(1), 61–70. https://doi.org/10.1016/j.epsl.2009.01.020

Pearson, D. M., Kapp, P., DeCelles, P. G., Reiners, P. W., Gehrels, G. E., Ducea, M. N., & Pullen, A. (2013). Influence of pre-Andean crustal structure on Cenozoic thrust belt kinematics and shortening magnitude: Northwestern Argentina. *Geosphere*, *9*(6), 1766–1782. https://doi.org/10.1130/GES00923.1

Pfiffner, O. A. (2017). Thick-Skinned and Thin-Skinned Tectonics: A Global Perspective. *Geosciences*, *7*(3), 71. https://doi.org/10.3390/geosciences7030071

Poudjom Djomani, Y. H., O'Reilly, S. Y., Griffin, W. L., & Morgan, P. (2001). The density structure of subcontinental lithosphere through time. *Earth and Planetary Science Letters*, *184*(3), 605–621. https://doi.org/10.1016/S0012-821X(00)00362-9

Price, R. A. (1981). The Cordilleran foreland thrust and fold belt in the southern Canadian Rocky Mountains. *Geological Society, London, Special Publications*, *9*(1), 427–448. https://doi.org/10.1144/GSL.SP.1981.009.01.39

Pusok, A. E., & Kaus, B. J. P. (2015). Development of topography in 3-D continental-collision models. *Geochemistry, Geophysics, Geosystems*, *16*(5), 1378–1400. https://doi.org/10.1002/2015GC005732

Pysklywec, R. N., & Beaumont, C. (2004). Intraplate tectonics: feedback between radioactive thermal weakening and crustal deformation driven by mantle lithosphere instabilities.

Earth and Planetary Science Letters, *221*(1), 275–292. https://doi.org/10.1016/S0012-821X(04)00098-6

Ramos, V. A., & Folguera, A. (2009). Andean flat-slab subduction through time. *Geological Society, London, Special Publications*, *327*(1), 31–54. https://doi.org/10.1144/SP327.3

Ramos, V. A., Zapata, T., Cristallini, E., & Introcaso, A. (2004). The Andean Thrust System Latitudinal Variations in Structural Styles and Orogenic Shortening, 30–50.

Smith, D., & Griffin, W. L. (2005). Garnetite Xenoliths and Mantle–Water Interactions Below the Colorado Plateau, Southwestern United States. *Journal of Petrology*, *46*(9), 1901–1924. https://doi.org/10.1093/petrology/egi042

Sobolev, S. V., & Babeyko, A. Y. (2005). What drives orogeny in the Andes? *Geology*, *33*(8), 617–620. https://doi.org/10.1130/G21557AR.1

Sobolev, Stephan V., Babeyko, A. Y., Koulakov, I., & Oncken, O. (2006). Mechanism of the Andean Orogeny: Insight from Numerical Modeling. In O. Oncken, G. Chong, G. Franz, P. Giese, H.-J. Götze, V. A. Ramos, et al. (Eds.), *The Andes* (pp. 513–535). Springer Berlin Heidelberg. https://doi.org/10.1007/978-3-540-48684-8_25

Spencer, J. E. (1996). Uplift of the Colorado Plateau due to lithosphere attenuation during Laramide low-angle subduction. *Journal of Geophysical Research: Solid Earth*, *101*(B6), 13595–13609. https://doi.org/10.1029/96JB00818

Stockmal, G. S., Beaumont, C., Nguyen, M., & Lee, B. (2007). Mechanics of thin-skinned fold-and-thrust belts: Insights from numerical models. *Geological Society of America Special Papers*, *433*, 63–98. https://doi.org/10.1130/2007.2433(04)

Strecker, M. R., Alonso, R. N., Bookhagen, B., Carrapa, B., Hilley, G. E., Sobel, E. R., & Trauth, M. H. (2007). Tectonics and Climate of the Southern Central Andes. *Annual Review of Earth and Planetary Sciences*, *35*(1), 747–787. https://doi.org/10.1146/annurev.earth.35.031306.140158

Tassara, A., Götze, H.-J., Schmidt, S., & Hackney, R. (2006). Three-dimensional density model of the Nazca plate and the Andean continental margin. *Journal of Geophysical Research: Solid Earth*, *111*(B9). https://doi.org/10.1029/2005JB003976

Tesauro, M., Kaban, M. K., & Cloetingh, S. A. P. L. (2013). Global model for the lithospheric strength and effective elastic thickness. *Tectonophysics*, *602*, 78–86. https://doi.org/10.1016/j.tecto.2013.01.006

Whitman, D., Isacks, B. L., & Kay, S. M. (1996). Lithospheric structure and along-strike segmentation of the Central Andean Plateau: seismic Q, magmatism, flexure, topography and tectonics. *Tectonophysics*, *259*(1–3), 29–40. https://doi.org/10.1016/0040-1951(95)00130-1

Chapter 4

Applying constraints of surface topography, shortening magnitude and mantle flow under the plateau on geodynamic simulations of the foreland deformation in the Altiplano-Puna plateau

Abstract

A spectacular along-strike segmentation of the style and magnitude of deformation and the nature of sedimentary basins exists in the Altiplano-Puna plateau. In the northern Altiplano segment, the tectonic shortening started during the Eocene and its accumulated magnitude is more than 300 km. A ~250-km-wide thin-skinned thrust wedge locates in the eastern flank of the plateau as an indication of a simple-shear shortening mode. The thrust zone correlates with thick Paleozoic units, in which a series of Silurian, Devonian, and Carboniferous detachments define the basal decollément of the orogenic wedge. In contrast, these mechanically weak layers abate and eventually vanish in the southern Puna. The foreland shortening there started later and is approximately two times smaller than in the Altiplano foreland. In addition, the deformation pattern changes to pure-shear accompanied by the thick-skinned structure. Previous studies suggest an intimate relation between the foreland-deformation diversity and both the shallow and deep lithospheric structures. However, the relationship between foreland-deformation patterns and surface topography and subduction-induced mantle flow beneath the plateau is not well-known. Here, I apply more constraints (magnitude of shortening, subduction-induced corner flow, and surface topography) on the high-resolution 2D geodynamic models to quantify this relationship. I propose two preferred models for each of the plateau provinces, where in addition to the reconstruction of the foreland-deformation type, the topography of the plateau-foreland system has an appropriate first-order fit to the observations. The Altiplano model implies that before the start of 120 km shortening at ca. 10 Ma, the plateau crust, underlain by a thin lithospheric lid, was much thicker and moderately denser than the foreland crust, overlain by thick, mechanically weak Paleozoic sediments. The Puna model implies that the thick plateau crust, without the lithospheric lid, was thinner than

the Altiplano crust at the beginning of 60 km shortening and weak sediments were absent in the Puna foreland. Mantle flow under the plateau, likely caused by subduction process in the mantle wedge corner, has a significant effect on the shortening style by controlling the dipping direction of the reverse fault on the western edge of the Puna foreland. Furthermore, a modeled basal shear zone dipping down to ~45 km at the boundary between the Puna plateau and its foreland coincides with the observed seismogenic depth zone in the broken foreland of the NW Argentine Andes.

4.1 Introduction

In contrast to orogens formed through continental collision, such as the Himalayas, the Andean mountain system of western South America is known as the product of subduction of the oceanic Nazca plate beneath the South America plate (e.g., Dewey & Bird, 1970; James, 1971; Jordan et al., 1983; Ramos & Aleman, 2000). The tectonic processes, such as mountain-building processes, subduction of oceanic ridges, normal or flat subduction of the oceanic plate under the continental plate, vary temporally and spatially in different sectors of the Andes (Figure 4.1). There are remarkable differences between the central part and the rest of the Andes. For instance, the Central Andes, which after the Himalayan orogen, is the second-largest active orogen on Earth, contains a plateau along a distance of more than 1,500 km of modern subduction margins. The plateau is about 4 km high. Such a broad and high plateau is absent in the Northern and Southern Andes. The tectonic shortening started during the Eocene and accumulated more than 300 km in the central part, whereas much less shortening (less than 50 km) occurred in the side flanks of the Andes. The shortening in the Southern Andes started later (Allmendinger et al., 1997; Kley & Monaldi, 1998; Lamb et al., 1997; Vietor & Echtler, 2006).

The single broad plateau, which is the main continental-scale feature of the Central Andes between about 12°S and 27°S, has an average elevation of ~4 km, and lateral extents of ~1700 km from north to south and 300-400 km from west to east (Figure 4.2). The high plateau can be subdivided into the northern Altiplano of Peru and Bolivia and southern Argentine Puna plateaus, where the two plateaus differ in topography, lithospheric structure, and the conditions of formation (Allmendinger & Gubbels, 1996; Allmendinger et al., 1997). The Altiplano Plateau is an internally asymmetric drained basin with an average elevation of ~3.8 km while the Puna Plateau is characterized by a greater local relief and higher topography (~4.4 km average elevation), including a series of intermontane basins (e.g., Whitman et al., 1996; Figure 4.2). These contrasting elevation distributions reflect the different tectonic histories of the respective segments.

Figure 4.1. Schematic map of South America, modified from Stern (2004), shows ages of subducting Nazca plate close to the Peru-Chile trench, oceanic ridges (Gutscher, 2002), convergence rate and directions along the entire Andes (Norabuena et al., 1998; Angermann et al., 1999), and Andean volcanic zone (Ramos & Aleman, 2000). The morphotectonic structures of the central Andes (black dashed rectangular), modified from Siks & Horton (2011) and Ibarra et al. (2019), indicates the Altiplano-Puna plateau-foreland region.

Seismic studies indicate that such high elevation is largely compensated at depth by more than 70 km thick crust under the plateau, as a result of late Cenozoic crustal shortening (James, 1971a; Jordan et al., 1983; Isacks, 1988; Zandt et al., 1994; Beck & Zandt, 2002). Lithospheric thinning can also make the plateau uplift by producing an additional thermal component to the topography due to thermal expansion (Isacks, 1988). The seismic attenuation studies show a thinner plateau lithosphere beneath the Puna than that below the Altiplano (Whitman et al., 1996). Therefore, these studies suggested that the elevation of the Altiplano was caused primarily by crustal thickening, whereas the Puna topography is supported by both a crustal root (smaller than beneath the Altiplano) and by a shallower thermal asthenosphere.

The bulk shortening in the Central Andes has an average rate of ~0.5-1 cm/yr over the last 45 Ma, and the shortening rate increases to 1-1.6 cm/yr from 10 Ma (Oncken et al., 2006). The accumulated shortening, during the late Cenozoic, is more than 300 km in the Altiplano and 120-150 km in the Puna (Figure 4.3). This shortening generated an unusually thick continental crust throughout the Central Andes (Allmendinger & Gubbels, 1996; Beck et al., 1996; Isacks, 1988; Beck & Zandt, 2002; Yuan et al., 2002). In the last 10 Ma, the cumulative shortening is 120 km for the Altiplano foreland, which is approximately 40% of late Cenozoic shortening (Oncken et al., 2006) and about double of the Puna foreland shortening. The present-day crustal thickness varies from 65-80 km in the Altiplano plateau to 50-65 km in the Puna plateau (Figure 4.3).

The crustal thickness under the Central Andean hinterland is nearly double the thickness of the crust under its foreland. From the perspective of mass conservation, the thickness of the mantle lithosphere should have doubled as well. However, it is inferred that the mantle lithosphere is anomalously thin under the Altiplano Plateau and likely completely absent under the Puna Plateau at present-day, even though the magnitude of lithospheric shortening across the Puna is less than half of that across the Altiplano (Kay & Kay, 1993; Whitman et al., 1996; Myers et al., 1998; Haberland et al., 2003). This violates a simple linear relationship between the shortening rate and the lithospheric thickness.

Seismic velocities are relatively high in the uppermost mantle of the central Altiplano Plateau and a relatively low in the crust and uppermost mantle in the Puna Plateau and its foreland, confirming a thicker lithosphere in the Altiplano (Myers et al., 1998; Schurr et al., 2006; Heit et al., 2008; Bianchi et al., 2013). This seismic evidence confirms that under the Altiplano a

lithospheric lid is still present, whereas beneath the Puna, the mantle lithosphere is completely removed. Removal of the entire lithosphere may explain why the Puna stays at a higher elevation than the Altiplano, despite having a thinner crust (Yuan et al, 2002). However, seismic images illustrating the present-day subsurface structure do not constrain the timing of lithosphere removal.

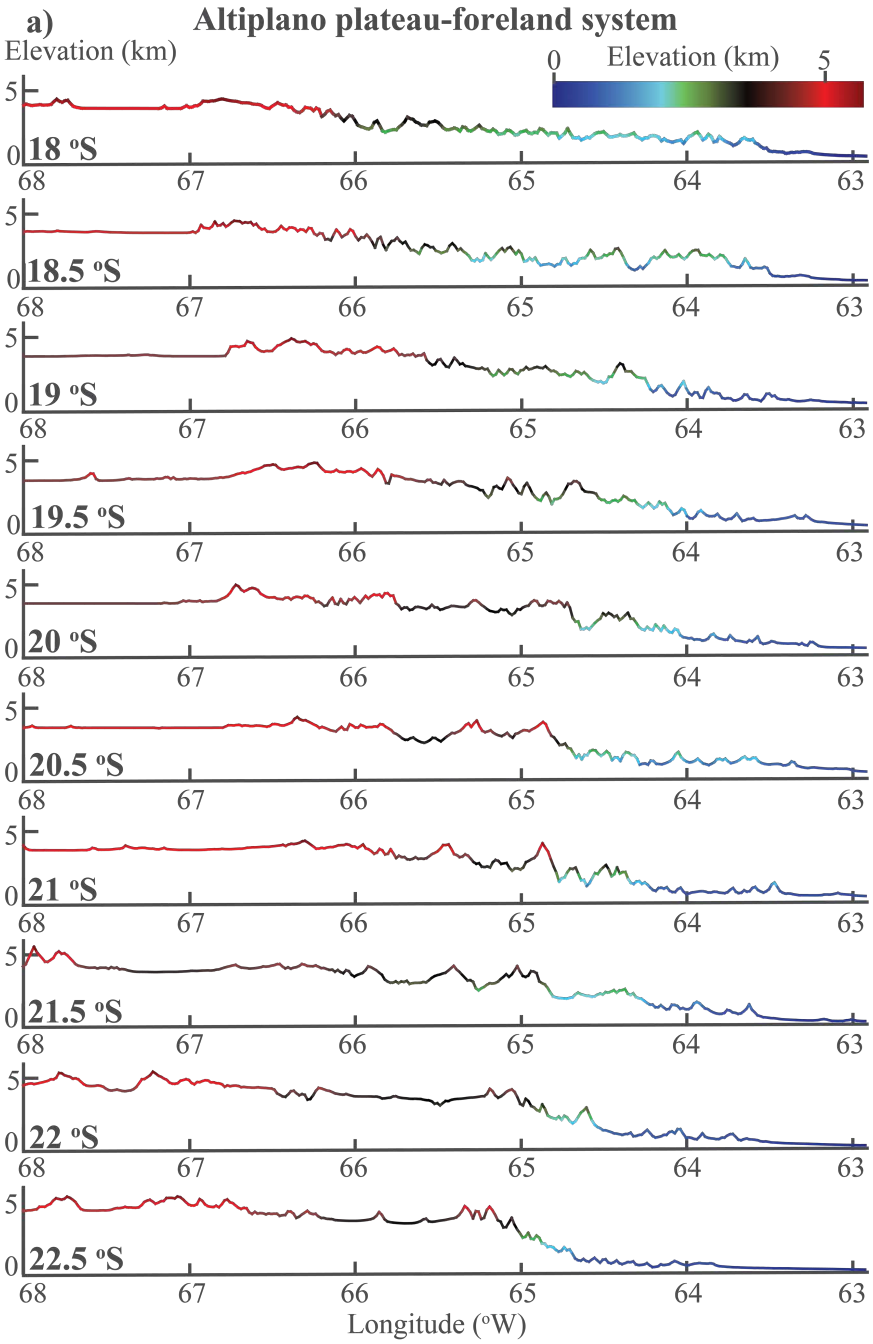

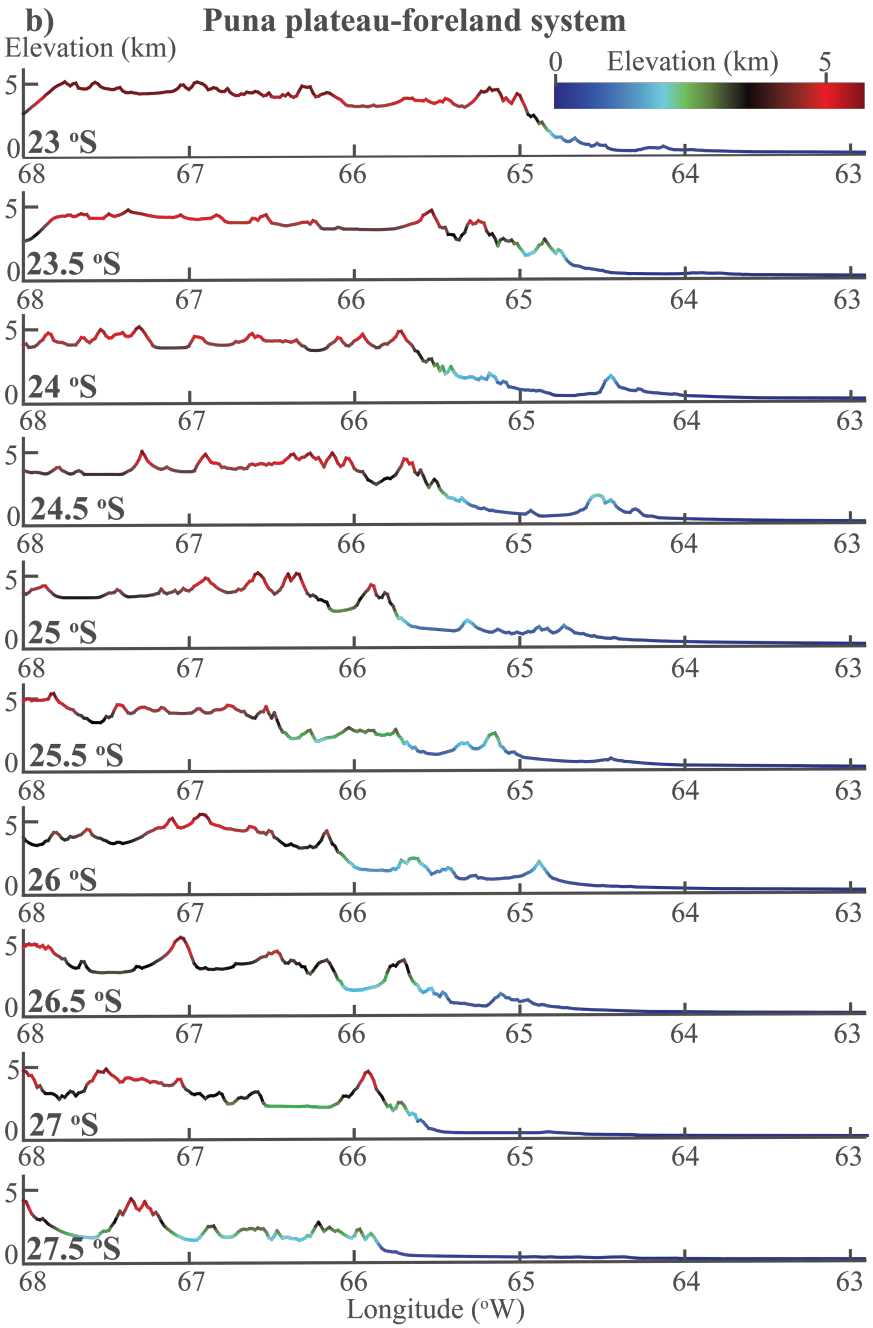

Figure 4.2. Surface topography of the Altiplano-Puna plateau-foreland system. **a)** Topography observation of the Altiplano plateau-foreland system from 18°S to 22.5°S. **b)** Topography observation of the Puna plateau-foreland system from 23°S to 27.5°S. Data source: ETOPO1.

Seismic studies also indicate that the thick plateau crust in the central Andes mainly consists of felsic to intermediate rocks, and there appears to be a lack of mafic lower crust across the whole plateau (Beck & Zandt, 2002; Yuan et al., 2002). A basalt/gabbro-eclogite transition can occur when the thick crust reaches the critical depth. The eclogitized mafic crust has a similar seismic velocity as the underlying mantle lithosphere, thus making it difficult to distinguish between

them (Beck and Zandt, 2002). In other words, the eclogitized lower crust can either be thin but intact below the thick felsic crust, or (what is likely) have been removed with the underlying mantle lithosphere below much of the central Andes. Furthermore, the eclogitized lower crust can have a high density, and would provide the driving force to initiate the lithosphere removal process in the Puna Plateau, which is supported by seismic tomography images (e.g., Beck & Zandt, 2002; Kay & Coira, 2009; Krystopowicz & Currie, 2013; Wang et al., 2015).

The two plateau provinces are also distinguished by a pronounced N-S oriented differentiation in the style and magnitude of the upper crustal foreland deformation, and the nature of sedimentary basins (Allmendinger & Gubbels, 1996; Whitman et al., 1996; Kley et al., 1999). At approximately 23-24°S, east of the Altiplano plateau and the Eastern Cordillera, a ~250-km-wide, wedge-shaped, thin-skinned fold-and-thrust belt defines the eastern border of the orogen, which is then changed by the contiguous Chaco-Paraná foredeep (Figure 3.7 in Chapter 3). The spatial extent of the fold-and-thrust belt in Bolivia correlates with thick Paleozoic sedimentary units, in which a series of Silurian, Devonian, and Carboniferous detachments define the basal decollément of the orogenic wedge (Allmendinger & Gubbels, 1996; Pearson et al., 2013; Figure 4.3).

Conversely, south of 23-24°S, these mechanically weak layers thin and eventually disappear, and the thin-skinned tectonics is replaced by the thick-skinned tectonics on Santa Barbara broken forelands. Allmendinger and Gubbels (1996) interpreted the thin-skinned thrust zone in the Altiplano foreland as indicative of a simple-shear mode of lithospheric shortening, and the thick-skinned structure in the Puna foreland as an expression of pure-shear shortening.

The gradual increase of the wavelength of foreland structures from north to south is accompanied by decreasing accumulated shortening and the width of the orogenic plateau, and by decreasing the thickness of the foreland lithosphere. North-south trends are also evident in other key features of the Southern Central Andes, such as the timing of the N-S directed passage of Juán Fernandez Ridge during last 26 Ma, which probably resulted in the onset of the flat-slab subduction between 28-33°S and widening of the magmatic arc, and the timing of an ignimbrite flare-up in the Puna (e.g., Silva, 1989; Ramos & Aleman, 2000; Ward et al., 2017; Figure 4.1).

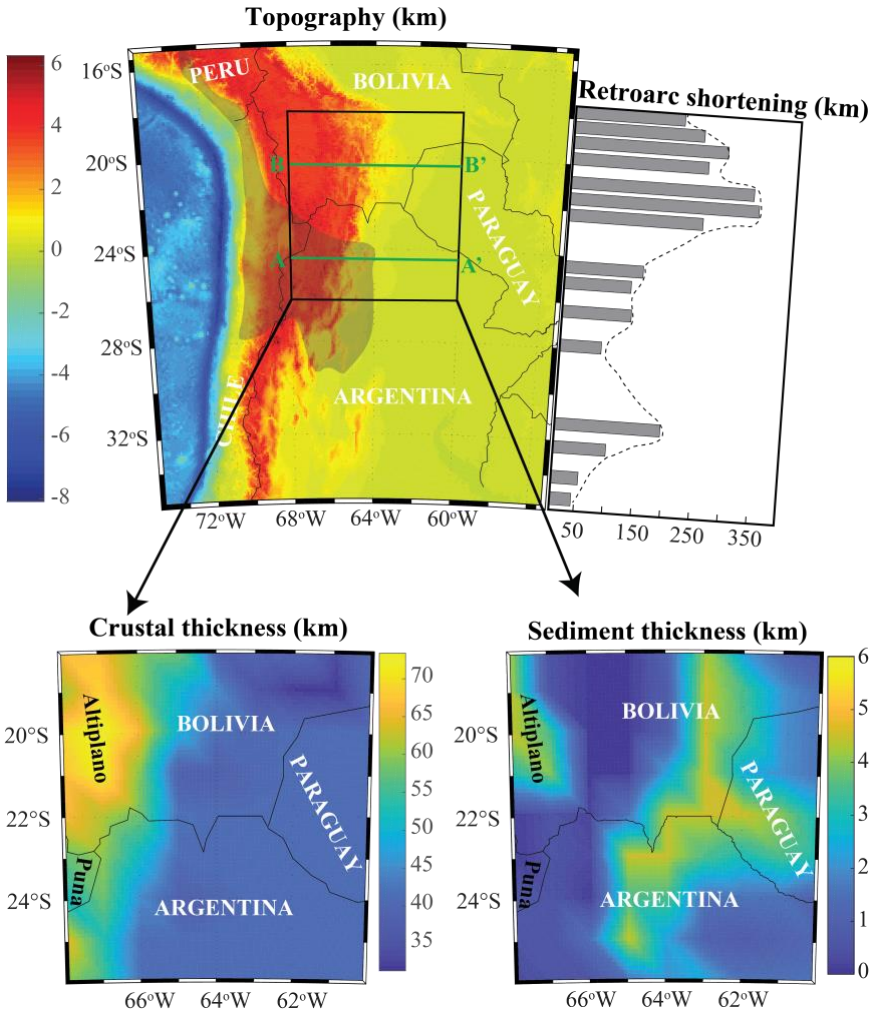

Figure 4.3. Present-day topography, thickness of the crust, thickness of the sedimentary layer in the Central Andes (data source: ETOPO1 and CRUST 1.0), and the magnitude of backarc shortening for the Central-Southern Andes, modified from Horton (2018).

These observations suggest a close connection between the style and intensity of deformation and lithospheric structures and processes. Large-scale thermomechanical models, supported by numerous field observations, can be used to explore these correlations between the different phenomena observed in the Central Andes. Previous 2D models of the Central Andes have attempted to quantify some of these correlations (e.g., Babeyko & Sobolev, 2005; Sobolev & Babeyko, 2005; Babeyko et al., 2006; Sobolev et al., 2006; Chapter 3 in this study). For instance, Babeyko and Sobolev (2005) and Babeyko et al. (2006) demonstrated that a strength drop of sedimentary basins above the foreland sediments might have been responsible for the pure- to simple-shear mode change and for the formation of thin-skinned wedge. The evolution of foreland deformation may also be correlated with N-S variations of the lithospheric strength in the Altiplano-Puna plateau-foreland system (Sobolev et al., 2006). However, these authors did

not further clarify how lithospheric strength variations and foreland sediment weakening control foreland-deformation patterns, due to the lack of necessary numerical resolution at that time.

The previous chapter systematically examined the nature of lithospheric strength variation as well as foreland sediment weakening, and their effects on the foreland deformation evolution. The results of high-resolution 2D thermomechanical models presented in that chapter are consistent with the observed foreland-deformation patterns in the Altiplano-Puna plateau. However, there are more observations in the plateau-foreland system in the Central Andes that can be used to constrain or to verify the numerical model. For example, the magnitude of shortening is different in the foreland region of these two plateaux. The question arises whether the models constrained by the appropriate magnitudes of shortening will show the same deformation patterns as previous models or not?

In addition to the foreland deformation, the surface topography of the Altiplano-Puna plateau-foreland region is worth using as a constraint for the models. The high plateau in the Central Andes is not as flat as in Tibet; instead, the two segments of the plateau have different elevations reflecting their different tectonic histories at the fairly recent stage (10-0 Ma). Whitman et al. (1993) proposed that these contrasting distributions are due to primarily crustal thickening for the Altiplano and both a crustal root and a thin mantle lithosphere root for the Puna. However, prior to this work, this hypothesis had not been tested by geodynamic models. In particular, relationships between shortening, lithospheric and crustal structures, and the elevation evolution of these two plateaux were not explored by modeling.

Tectonic shortening in the Central Andes is likely strongly correlated with the subduction of the Nazca oceanic plate beneath the South America plate during late Cenozoic (Jordan et al., 1983; Allmendinger et al., 1997; Sobolev et al., 2006; Vietor & Echtler, 2006; Ramos & Folguera, 2009). The subduction dynamics can affect both the foreland deformation and surface topography in the plateau-foreland system. A period of flat-slab subduction at about 35-25 Ma was recorded in the Altiplano segment (James & Sacks, 1999). This trend of slab flattening progressed to the Puna segment between 20° and 24°S between 18-12 Ma (Kley et al., 1999). The flat-slab later started to rollback, which was evidenced by widespread bimodal volcanism (James & Sacks, 1999).

The subduction zone produces a corner flow in the mantle wedge above the slab (Figure 1.1 in Chapter 1), which may be enhanced due to slab steepening. This corner flow can not only bring the hot asthenosphere up to melt the hydrated lithosphere beneath the plateau, and lead to important crustal and lithospheric delamination (Oncken et al., 2006; Wang et al., 2015), but also drag the overriding plate towards the subducting slab, resulting in the Cenozoic speedup of South America's trenchward motion (Russo & Silver, 1996). Therefore, the mantle flow can be associated with the overriding plate deformation (e.g., Isacks, 1988; Beck & Zandt, 2002; Garzione et al., 2006). A possible example of the relation of upper plate deformation with mantle flow is the Southern Patagonian Andes, where a change in the deformation regime coincides with the opening of the Drake Passage in the Oligocene (Barker, 2001; Livermore et al., 2005). However, the effect of slab-driven corner flow beneath the plateau on the foreland deformation and topography remains unclear.

In this chapter, by using high-resolution 2D thermomechanical models I first investigate the effect of the mantle flow on the foreland deformation in the Puna case. Then I study the surface topography evolution, in addition to the evolution of foreland-deformation patterns in both the Altiplano and the Puna segments and finally come out with models fitting best observations.

4.2 Numerical model description

4.2.1 Model geometry

The numerical models are designed to study the topography evolution in the Altiplano-Puna plateau and its foreland region in addition to the reconstruction of foreland-deformation patterns. The models inherit some features from the Central Andean models in the previous chapter. For example, the lithosphere under the Altiplano plateau has a thick crust and a thin lithospheric mantle while only a thick crust exists below the Puna plateau due to the lithosphere delamination. A weak sedimentary layer is covered upon the Altiplano foreland but absent in Puna foreland. The foreland lithosphere is thinner in the Puna case than in the Altiplano case, which is consistent with seismic evidence (Whitman et al., 1996).

The difference from previous models (Figure 3.7) is that here we broaden the model domain (now from a width of 68°W to 60°W) and to 400 km depth (Figure 4.4), which roughly fits two natural geomorphological cross-sections A-A' and B-B' shown in Figure 4.1. In the Altiplano

case, the hinterland region, between 68°W and 64.5°W, includes the Altiplano Plateau and the Eastern Cordillera. The foreland from 64.5°W to 60°W includes the Interandean Zone, Subandean Ranges, and Chaco Plain (Figure 4.4). The Puna hinterland is narrower than Altiplano hinterland and covers two degrees of longitude from 68°W. The Sa. De Zapla – Santa Barbara System – Chaco Plain foreland at 65.5-60°W is correspondingly wider than the Altiplano foreland. Furthermore, the amount of shortening is 120 km in the Altiplano model, and 60 km in the Puna model.

The finite-difference computer code LaMEM is used to calculate the mechanical evolution of surface topography through shortening, under assumptions of incompressibility and plane strain. The model mesh has 768 * 384 grid points, with a grid horizontal spacing of 0.85 km for 68°W-63°W and 1.95 km for 63°W-60°W. The vertical grid spacing is 0.73 km in the top 140 km and 1.35 km at greater depth. These smaller top grid elements are used to ensure a well-resolved orogen-foreland lithosphere and shallow sedimentary layer. Each grid point includes nine particles, which are advected with the model velocity field, to trace material properties.

4.2.2 Material properties and boundary conditions

The materials in the model have elasto-visco-plastic rheology with the pressure-dependent plastic yield stress according to the Drucker-Prager yield criterion (Equation 12 in Chapter 2). Felsic crustal materials undergo frictional-plastic strain-softening by decreasing the internal friction angle and cohesion with increasing finite strain. Specifically, the plastic-related friction coefficient is linearly reduced from 0.5 to 0.1 over accumulated strain of 0.5 to 1.5 (Table 3.1). This strain-softening approximates rock weakening due to pore fluid pressure variations, fault gouge formation and mineral reactions during deformation (e.g., Beaumont et al., 2006; Sobolev et al., 2006). When the deformation is viscous, we choose rheological parameters from previous studies (e.g., Babeyko et al., 2006; Beaumont et al., 2006; Liu & Currie, 2016). We use wet quartzite, dry Maryland diabase (MD_{dry}; Mackwell et al., 1998), and wet/dry olivine for the felsic crust and its sediment cover, the mafic crust, and the lithospheric/sublithospheric mantle, respectively.

All materials have a temperature-pressure-dependent density:

$$\rho_{P,T} = \rho_0 \left[1 - \alpha \left(T - T_0\right)\right]\left[1 + \frac{P - P_0}{K}\right] \qquad (1)$$

where ρ_0 is the reference density at the temperature T_0 (°C) and pressure P_0 (Pa), α is the volumetric thermal expansion coefficient, and K is the bulk modulus (e.g., Sobolev & Babeyko, 2005; Beaumont et al., 2006; Gerya & Stöckhert, 2006; Currie et al., 2008). The sediment is by 300 kg m^{-3} less dense than the underlying felsic crust at the same temperature. The felsic crust has a reference density of 2800 kg m^{-3}, which reflects a more granitic (silica-rich) composition than the mafic materials that make up the lower crust. The reference density of the mantle (3300 kg m^{-3}) is consistent with the density of fertile upper mantle (Poudjom Djomani et al., 2001).

The mechanical boundary conditions are as follows: 1) a stress-free top surface, which allows topography to develop at the bottom of the sticky-air layer in response to the underlying dynamics, 2) a free slip basal boundary, 3) no vertical velocity on the side boundaries, 4) a horizontal velocity of 2 cm/yr on the right lithosphere side boundary, 5) a velocity of 1 cm/yr on the left lithosphere side boundary, and 6) a variable velocity to the left side boundary of the sublithospheric mantle. In last 10 Ma, GPS data shows that the shortening rate increases eastward from 0.8 -1.1 cm/yr in Central Andes to 0.9-1.6 cm/yr in Subandean Ranges (Oncken et al., 2006), and may be increasing in the further eastern foreland than in Subandean belts. Hence, it makes sense to impose a high velocity on the right-side boundary that is a few hundred kilometers away east from the Subandean belts.

The free surface stabilization approach (Kaus et al., 2010) is applied to the top boundary, covered by the 10-km-thick low viscous and low density "sticky air" phase, which allows a relatively large integration timestep. The thermal boundary conditions are: 1) insulating (no heat flux) side boundaries, 2) a constant temperature of 1460°C at the base of the model at a depth of 400 km (this temperature corresponds to the potential temperature of 1300°C and adiabatic gradient of 0.4 °/km), and 3) a constant temperature of 0°C for the top boundary.

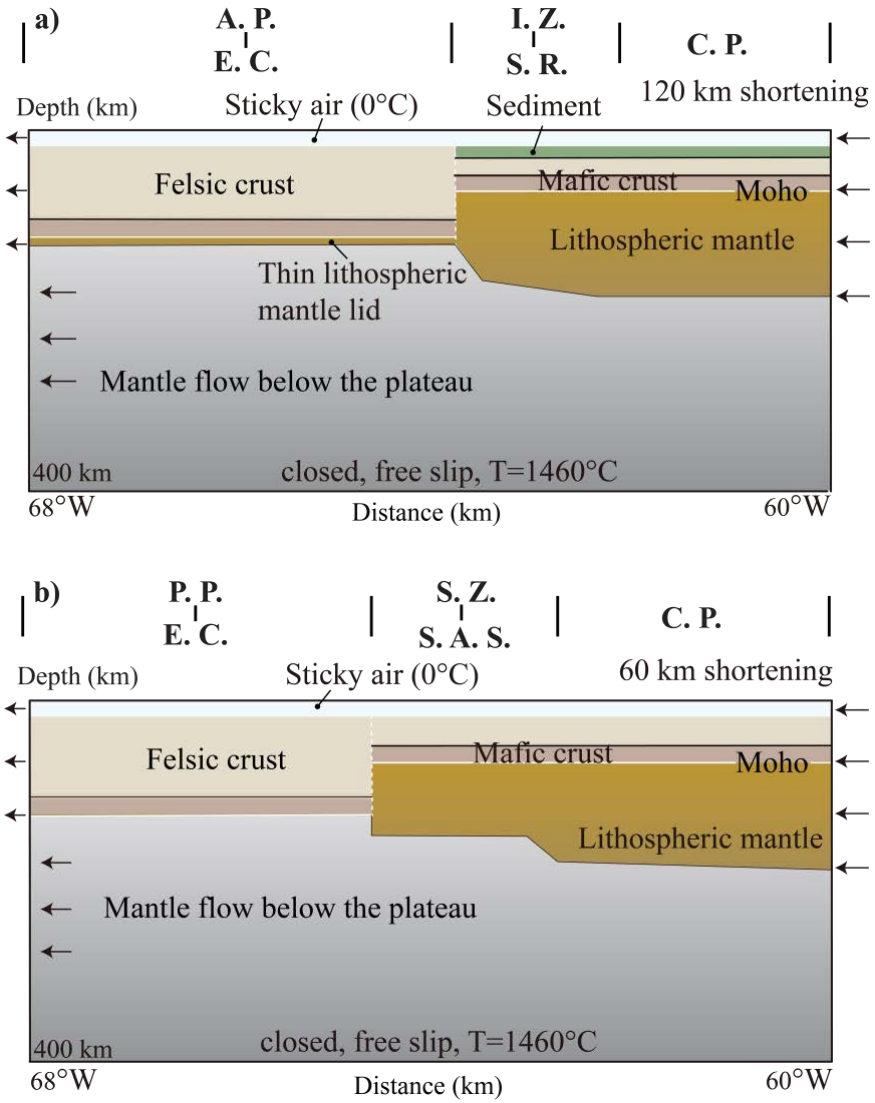

Figure 4.4. Initial model setup, including forelands of **(a)** the Altiplano Plateau and **(b)** the Puna Plateau. A.P. is the Altiplano Plateau, P.P. is the Puna Plateau, E.C. is the Eastern Cordillera, I.Z. is the Interandean Zone, S.R. is Subandean Ranges, S.Z. is Sa. de Zapla, S.A.S. is Santa Barbara System, C.P. is Chaco Plain.

4.3 Numerical results

4.3.1 Reference model

In the reference model R1, the orogenic lithosphere is as thin as 60 km and its crust is 50 km thick with a 38-km-thick felsic crust. The foreland lithospheric is 100-km-thick with a 36 km thick crust. Thus, the orogenic lithosphere is thinner and weaker than the foreland lithosphere (Figure 4.5a). The deformation is described by the second invariant of strain rate, which

characterizes the dynamics of changes of the internal deformation. The size of Model R1 is 400 * 400 km. As we are interested in the deformation evolution on the foreland crust part, the plot area is limited to the top 60 km. In order to minimize the effect of side boundary conditions, the off-plane horizontal distance is set to be between 50 km and 330 km.

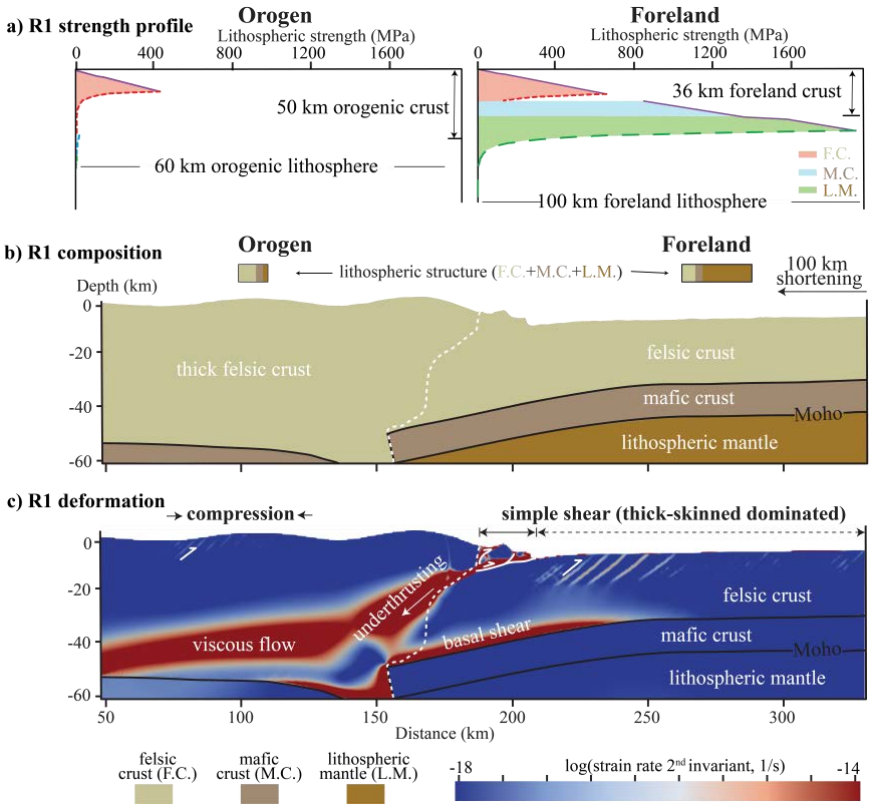

Figure 4.5. Reference model R1. **a)** Lithospheric strength profiles for both orogen (left) and its foreland (right). **b)** and **c)** are model profiles of the material field and the deformation field after 100 km shortening, respectively. The two small boxes on top of the composition profile are lithospheric structures with the lithospheric thickness inside. The white dashed line is the boundary between the orogen and its foreland. The black line is the boundary between different compositions. The white one-way arrows represent the fault direction. The black dashed/solid line with two arrows represents the thick-skinned/thin-skinned deformation in the foreland.

As shortening starts, the deformation first localizes at the weak orogen side, resulting in orogenic crust buckling and surface uplift. After 100 km shortening, the foreland intrudes into the orogen and forms a basal shear just above the top of the mafic crust. Simultaneously, the foreland felsic crust intrudes into the orogen forming the viscous flow in the thickened orogenic felsic crust (Figure 4.5b). This underthrusting process produces a simple-shear shortening mode and a narrow zone of the thin-skinned thrust in the foreland edge. The contribution of the thin-

skinned deformation to the total foreland crustal deformation is less than 10%, thus we consider this type of deformation structure as thick-skinned dominated (Figure 4.5c).

In order to compare the modeled topography with the observed, we set the boundary point between the orogen and its foreland (Figures 4.5 and 4.6) as a reference point. Then we fix this point to be the eastern edge point of the hinterland (e.g., the edge of the Altiplano Plateau - East Cordillera region in Figure 4.3; Figure 1 in Siks & Horton (2011).

Note that our model does not consider the surface erosion and sedimentation, which may smooth the large elevation difference between the plateau and its foreland through time. Therefore, currently we can only study the first-order relationship between surface topography and deep lithospheric dynamics. In future work, the surface process should be included in the numerical model.

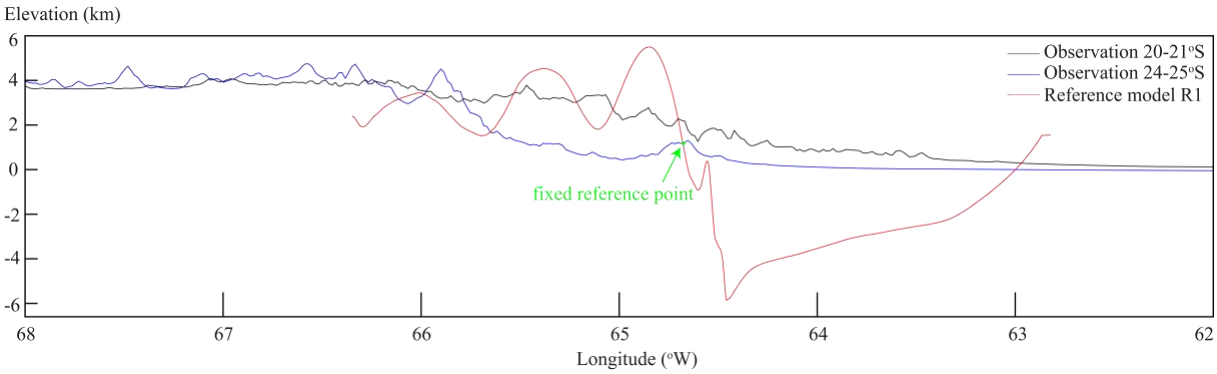

Figure 4.6. Surface topography of the reference model R1 after 100 km shortening (red line). The observations represent the average topography of the Altiplano region at 20°S -21°S (black line) and the Puna region at 24°S - 25°S (blue line). The green solid point represents the fixed reference point for the comparison between modeled topography and observation.

4.3.2 The effect of mantle flow on the foreland deformation

In the Puna plateau-foreland system, a slab steepening (flat to normal dip) occurred in the last 10-12 Ma in the Puna segment (Ramos & Folguera, 2009), which produced asthenosphere flow in the wedge corner above the slab. Here we present numerical models similar to the Puna case, but with an additional westward mantle flow beneath the plateau to study its effect on the foreland deformation during shortening.

First, I develop a simple numerical model, where there is an intraplate shortening between a plateau with a 60-km-thick crust-only lithosphere and a 70-km-thick foreland lithosphere (Figure 4.7). The thin foreland lithosphere is still much mechanically stronger than the lithosphere of the plateau due to the thin foreland crust (Figure A.1 in Chapter 3). After 100 km shortening, the foreland crust, in the model without mantle flow (Figure 4.7a), underthrusts into the plateau. The foreland crust deforms in the simple-shear mode, and the underthrusting lithosphere produces a viscous crustal flow at the bottom of the plateau felsic crust. When there is a mantle flow under the plateau (Figure 4.7b), the shortening mode in the foreland changes to pure-shear. The magnitude of viscous flow in the plateau lower crust becomes smaller, and thus the plateau crust thickens less than that in the model without mantle flow. Interestingly, the fault dipping direction is different in these two models.

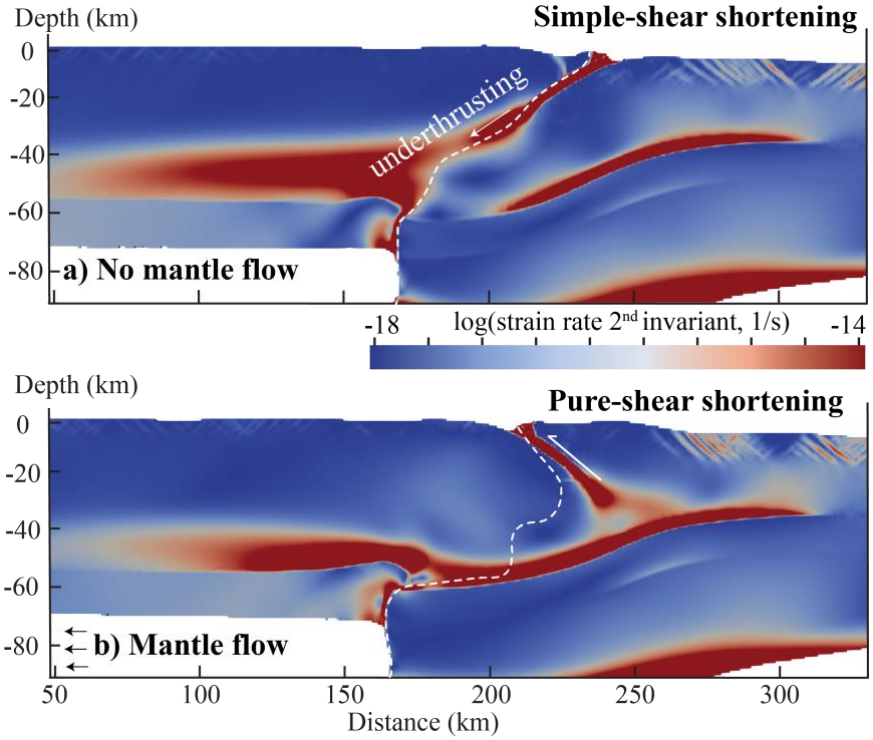

Figure 4.7. A numerical example showing the effect of mantle flow on the foreland shortening mode.

I then set up the model closer to the real case of the Puna plateau-foreland system by adding more constraints from geological and geophysical observations (Figure 4.4b). At the beginning the plateau crust is only 50km thick, and it is assumed that the mantle lithosphere beneath the plateau is delaminated. The foreland lithosphere is 70 km thick close to the edge of the plateau

and linearly increases to 110 km eastwards. The shortening rate Vs = 2 cm/yr, is imposed at the foreland side boundary, and the velocity of mantle flow below the plateau differs from 0 to 2Vs (Figure 4.8). With the flow speeding up, more intensive deformation is localized on the western edge of the foreland, and the magnitude of the reverse fault (white arrow in Figure 4.8) increases. Additionally, a second mega reverse fault is formed inside the foreland when the flow rate is double the shortening rate (Figure 4.8d). In all cases foreland crust deforms in pure-shear mode regardless of the intensity of mantle flow, but the pronounced inverse fault appears only when the mantle flow rate is higher than a quarter of the shortening rate.

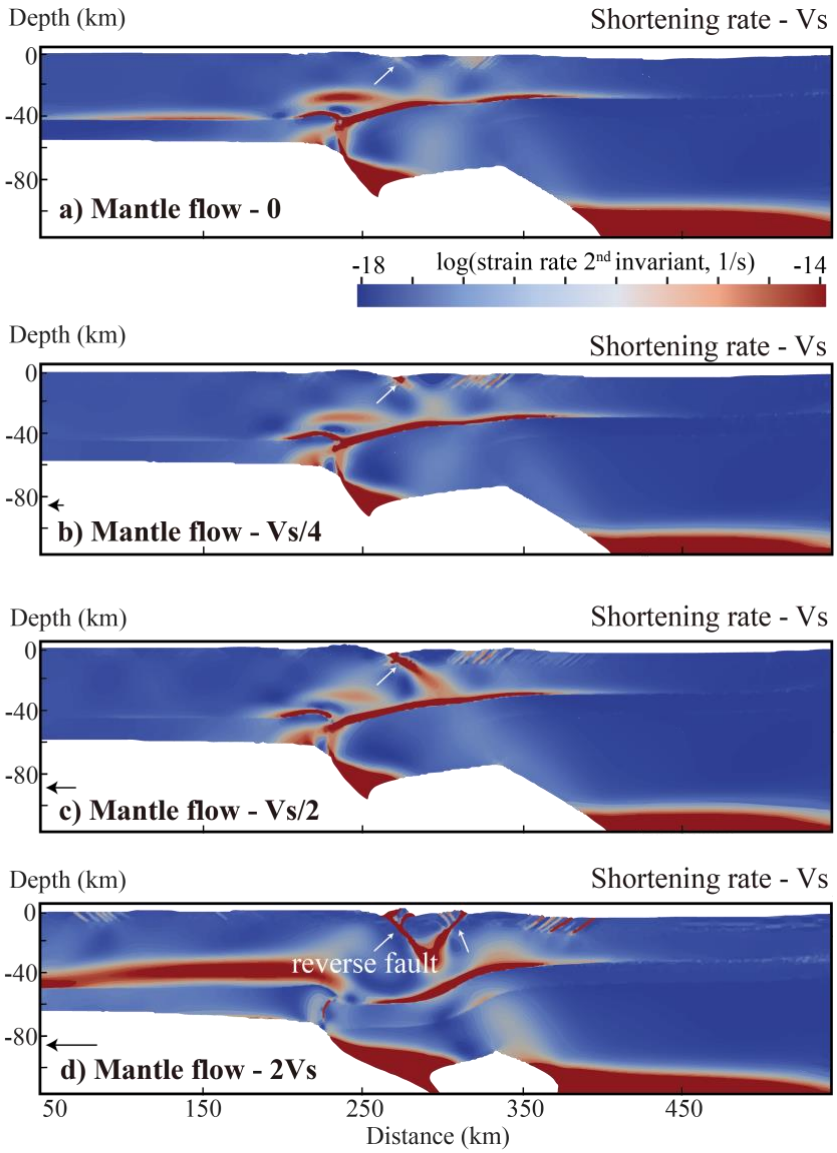

Figure 4.8. The effect of mantle flow on the foreland deformation pattern in the Puna case. The white arrow represents the formation of the mega reverse fault due to the speeding up of mantle flow below the plateau.

4.3.3 Preferred model for the Altiplano plateau-foreland system

The northern Altiplano portion of the Central Andes is characterized by thin-skinned, eastward propagating deformation in its foreland. Seismic evidence showed that the thick hinterland crust under the plateau and Eastern Cordillera gets thinner towards the east to the Interandean-Subandean Zone, but the lithosphere thickens from the hinterland to the foreland. In addition, there are mechanically weak sedimentary basins with thick pre-Cenozoic units on the foreland surface. The mantle flow, from the further western mantle wedge due to the Nazca plate subduction process, is inferred to be under the plateau with a trenchward direction.

With these constraints on the Altiplano model (Table 4.1), I investigate the relationships between the lithospheric structure, mantle flow, foreland deformation, and surface topography. Here I show the preferred model for the Altiplano case (Figure 4.9 - 4.10).

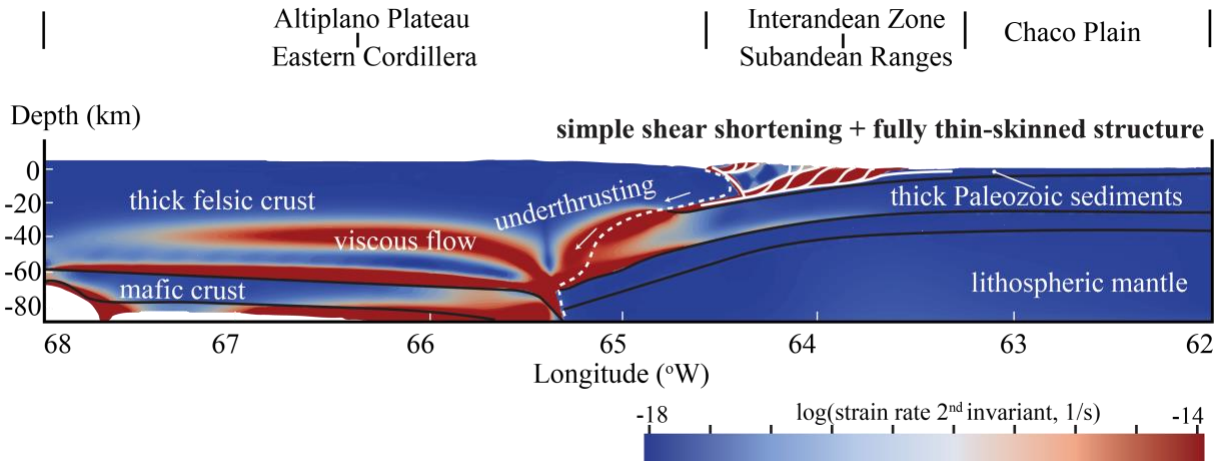

Figure 4.9. Altiplano plateau-foreland model after 120 km shortening. A simple-shear shortening mode, accompanied by fully thin-skinned deformation, is developed in the Interandean – Subandean Zone. Note that the mantle flow beneath the hinterland is not shown.

At the beginning, there is a 5 km thin mantle lithospheric lid underlying the 67-km-thick crust, with a 55-km-thick felsic part, below the hinterland. The thickness of plateau crust increases up to 80 km after 120 km shortening, which is consistent with the present-day observations (e.g., Yuan et al., 2002; Tassara et al., 2006). After 120 km shortening, there is a fully thin-skinned thrust zone formed in the thick Paleozoic sedimentary basin of the Interandean - Subandean zone. The mega fault zone dives to a depth of about 20 km, as a result of the underthrusting of the foreland crust into the thick plateau crust indicating the simple-shear deformation mode.

The underthrusting produces a viscous flow in the plateau lower crust, which results in its crustal thickening and surface uplift.

Figure 4.10 shows the surface topography of the preferred Altiplano model after 120 km shortening compared with the observed average present-day topography between 20°S and 21°S. The model topography has a good first-order fit to the observation; the difference may well be due to the surface erosion and sedimentation not considered in the model. The surface processes can smooth the elevation by eroding the surface at high elevation and then transporting and depositing the material into the low-land. Note that in order to fit the observed topography the density of the plateau crust in the model was set to be by 100 kg/m3 denser (at the same temperature) than the foreland crust, which we interpret as a result of the high-pressure metamorphic reactions in the thickened crust of the plateau.

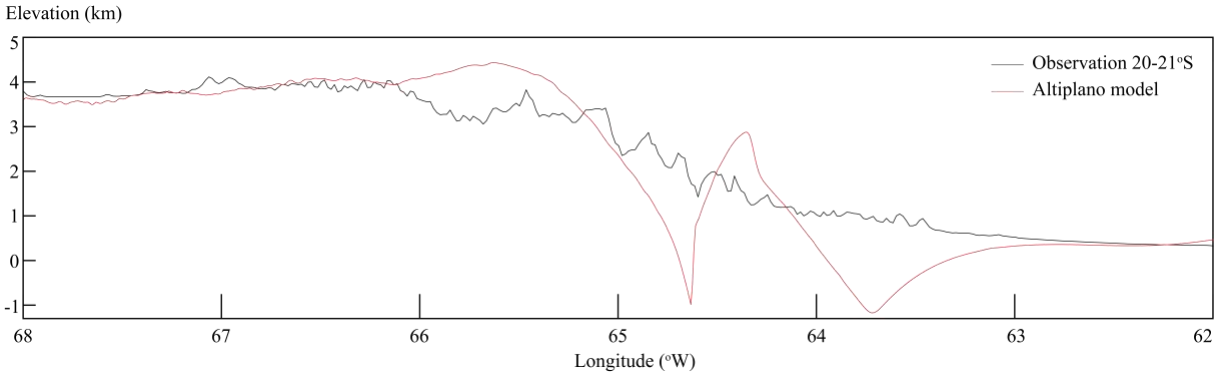

Figure 4.10. Modeled surface topography of the Altiplano plateau and its foreland after 120 km shortening (red line). The observation represents the average topography of the Altiplano plateau-foreland region at 20°S -21°S (black line). Note that the model does not include surface erosion and sedimentation.

4.3.4 Preferred model for the Puna plateau-foreland system

The foreland of the Puna plateau is distinguished from the Altiplano foreland by the uplift of basement ranges and thrusts along reverse faults. Compared with the northern Altiplano plateau, the crust of the Puna plateau is thinner and likely has no mantle lithosphere lid below it due to the lithosphere delamination. The foreland lithosphere is likely thinner than in the Altiplano foreland, which is inferred from the high seismic attenuation in this area. In the last 10 Ma, the magnitude of shortening in the Puna plateau foreland system is approximately half of the

shortening of the Altiplano system. Similar to the Altiplano model, I apply these constraints to the Puna models (Table 4.1) and here shows here only the best-fit preferred model (Figure 4.11 - 4.12).

The initial plateau crust is 60 km and includes a 48-km-thick felsic crust. The initial lithosphere overlain by a thin crustal layer is 70 km thick in the Sa. de Zapla and the Santa Barbara System and is thickened to 120 km eastwards in Chaco Plain. Beneath the plateau, there is a mantle flow with the same velocity as the shortening rate, induced by the mantle wedge corner flow. After 60 km shortening, the foreland undergoes a pure-shear deformation, where there is no underthrusting process and no viscous flow in the thick felsic crust under the plateau. The absence of a weak, thick, Paleozoic sedimentary basin causes the fully thick-skinned deformation in the Sa. de Zapla - Santa Barbara System. Interestingly, the fault zone extends from the surface to the bottom of the felsic crust to a depth of 40-50 km and produces the basal shear. This is almost double the depth of the estimated deeping depth from previous geological studies (e.g., Kley et al., 1999). However, recent seismic studies in the broken foreland of the NW Argentine Andes (Zeckra et al., 2019, unpublished) shows that the seismogenic depth zone can be as high as 45 km. This is consistent with the depth of the basal shear zone in our model and verifies such a deep root of the fault.

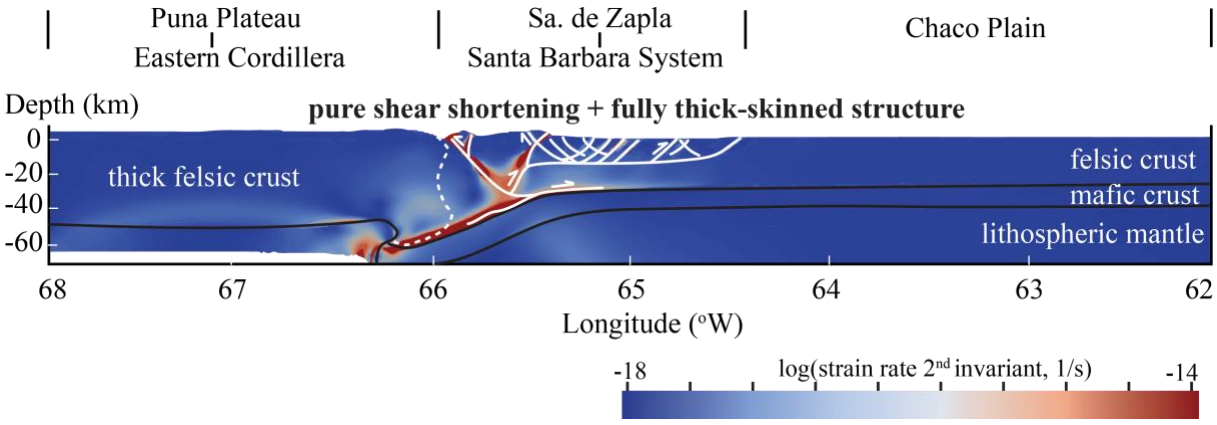

Figure 4.11. Puna plateau-foreland model after 60 km shortening. A pure-shear shortening mode, accompanied by fully thick-skinned deformation, is developed in the Sa. De Zapla - Santa Barbara System. Note that the mantle flow beneath the hinterland is not shown.

Regarding the surface topography (Figure 4.12), the average elevation is about 4-4.5 km in the Puna Plateau - Eastern Cordillera hinterland, consistent with the observed elevation (Figure 4.3). Similar to the Altiplano case, the elevation of the Sa. de Zapla - Santa Barbara System

poorly matches to the observation due to the absence of surface erosion and sedimentation in the model.

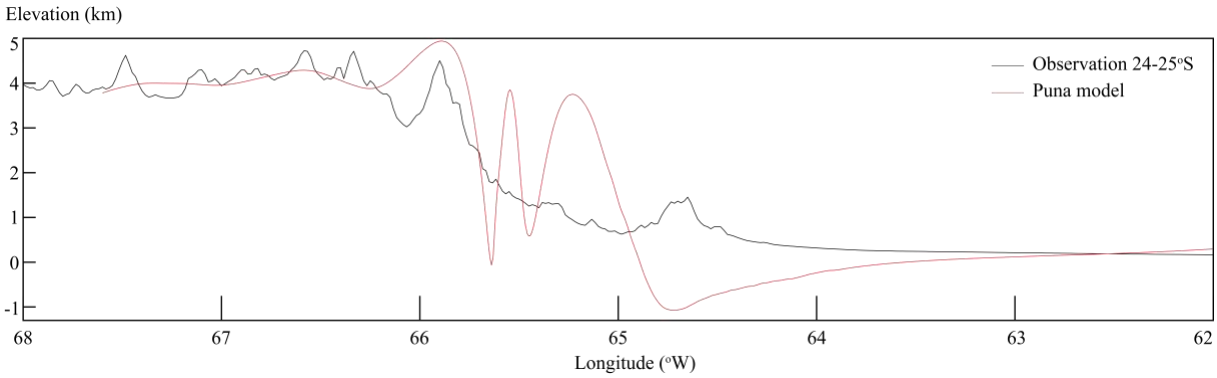

Figure 4.12. Modeled surface topography of the Puna plateau and its foreland after 60 km shortening (red line). The observation represents the average topography of the Puna foreland region at 24°S -25°S (black line). Note that the model does not include surface erosion and sedimentation.

4.4 Discussion and conclusions

4.4.1 Summary of model results

I conducted a number of model experiments to investigate the evolution of plateau-foreland topography and the lithospheric structure of the plateau-foreland system in the Central Andes, during tectonic shortening with the subduction-induced corner flow (Table 4.1). I first select the models with the observation-consistent deformation patterns that develop in both the Altiplano foreland (fully simple-shear with thin-skinned thrust) and the Puna foreland (fully pure shear with thick-skinned tectonics). The magnitude of shortening was set to 120 km in the northern Altiplano section and 60 km in the southern Puna section in agreement with observations. I then examine the effect of each of the following factors: (i) thickness of the plateau lithosphere and plateau crust, (ii) thickness of the foreland lithosphere, (iii) density of the plateau crust and (iv) their combinations on the surface topography.

Table 4.1. List of models showing parameter variations tested in this section. ML is the mantle lithosphere. The mantle flow is below the plateau.

Model group	Crustal thickness (km)	ML thickness (km)	Mantle flow (cm/yr)	Figure #
Group A: test variation in the plateau crust in the **Altiplano case**. A1' is the model where the mafic crust is thicker than the felsic crust in the foreland. A2' and A3' are models where the foreland sediments are not weak.				
A1	55	0	0, 2	
A1'	55	0	0	
A2	60	0	2	
A2'	60	0	2	
A3	60-50	0	2	
A3'	60-50	0	2	
Group B: test variation in the plateau mantle lithosphere in the **Altiplano case**. B2' is the model where the mafic crust is thicker than the felsic crust in the foreland. B4', B5' are models where the plateau crust is 100 kg/m3 denser at the same temperature than the foreland crust.				
B1	45	5	0, 2	
B2	50	10	0, 2	Figure 4.5-4.6
B2'	50	10	0, 2	
B3	60	5	0, 0.5, 1, 2	
B4	67	0, 5, 10	2	
B4'	67	0, 5, 10	2	Figure 4.9-4.10
B5	72	0, 5, 10, 15, 20	2	
B5'	72	0, 5, 10, 15, 20	2	
Group C: test variation in the plateau crust in the **Puna case**. C2' and C4'are models where the thickness of the foreland lithosphere under Sa. de Zapla - Santa Barbara System is 48-70 km. C5' is the model where the model domain is 400 km wide.				
C1	50	0	0, 0.5, 1, 4	Figure 4.8
C2	52	0	0, 2	
C2'	52	0	2	
C3	55	0	0, 0.5, 1, 2	
C4	55-50	0	2	
C4'	55-50	0	2	
C5	60	0	0, 1, 2, 4	Figure 4.11-4.12
C5'	60	0	0, 2	Figure 4.7
C6	60-55	0	0, 1, 2, 4, 6	
Group D: test variation in the plateau mantle lithosphere in the **Puna case**.				
D1	60	3, 5, 10	0, 1, 2	

Obviously, the thickening of the plateau crust lifts the plateau, which in turn increases the elevation difference between the plateau and its foreland (e.g., the topography difference in Model A2 is ~500 m higher than in Model A1). The thickness of the thin mantle lithosphere lid insignificantly changes the topography (compare Model A2 with Model B3). The topography in the foreland rises when the foreland lithosphere becomes thinner (Model C4'). If the lithosphere is thinner, the hot asthenosphere becomes thicker, which provides an additional thermal component to the topography (e.g., Isacks, 1988; Currie, 2016). The weak sediments in the foreland have little effect on the evolution of surface topography but a large effect on the foreland deformation style (compare A2 and A3 with A2' and A3').

The effect of mantle flow below the plateau on both the foreland deformation pattern and surface topography is important. For example, in Model A1, the difference between plateau and foreland elevations is about 500 meters larger when the mantle flow is present below the Altiplano Plateau. Furthermore, the mantle flow in Model C5' does not only change the shortening mode of the foreland (Figure 4.7) but also assists the formation of megathrust fault at the edge of the foreland (Figure 4.8).

4.4.2 Fitting of deformation patterns together with surface topography in the Altiplano-Puna plateau and its foreland

How strength variations of the crust and the lithosphere affect foreland deformation is discussed in Chapter 3. The generic models successfully reproduce foreland-deformation patterns of Central Andes but are not fully consistent with observed shortening rates and surface topography. Here I present preferred models for the Altiplano and Puna sections, that fit data on shortening rates, foreland-deformation patterns (Figure 4.9 and 4.11) and first-order features of surface topography (Figure 4.10 and 4.12).

In the preferred model for the Altiplano section, the foreland deforms in the simple-shear mode with a fully thin-skinned thrust belt, and the topography of the plateau-foreland system coincides with the observed average topography at 20°S-21°S. In this model, the magnitude of total shortening is 120 km, which is equal to the cumulative shortening of the Central Southern Andean (21°S) in the last 10 Ma. After shortening, the thick crust under the hinterland further thickens to about 80 km, in agreement with the present-day crust under the Altiplano Plateau and Eastern Cordillera. The Altiplano crust should be denser (by about 100 kg/m$_3$) than the

western foreland crust in the Interandean-Subandean Zone, likely because of the high-pressure metamorphic reactions in the thickened crust.

The preferred model for the Puna section reproduces first-order topography features at 24°S-25°S, where the elevation of the hinterland region (i.e., the Puna Plateau and Eastern Cordillera) is 4-4.5 km and decreases to almost sea level in the far east foreland. There is a poor topography fit in the Sa. de Zapla-Santa Barbara System deformation area, most likely owing to the absence of erosion and sedimentation in the model. The Puna system undergoes a 60 km shortening, which is half of the Altiplano shortening. The mantle flow below the plateau due to the subduction process in the mantle wedge corner is another critical factor (in addition to the lithospheric strength and foreland sediment strength) controlling surface topography and foreland-deformation pattern. The corner flow maintains the east-dipping reverse faulting on the edge of the foreland and enables the pure-shear shortening mode accompanied by a fully thick-skinned deformation structure in the Sa. de Zapla-Santa Barbara System region. It also facilitates the fault to extend deep into the felsic crust at (~45 km) and forms the basal shear zone. The existence of this zone is verified by the recent seismic observations in the broken foreland of the NW Argentine Andes.

References

Allmendinger, R. W., & Gubbels, T. (1996). Pure and simple shear plateau uplift, Altiplano-Puna, Argentina and Bolivia. *Tectonophysics*, *259*(1), 1–13. https://doi.org/10.1016/0040-1951(96)00024-8

Allmendinger, R. W., Teresa E. Jordan, Suzanne M. Kay, & Isacks, and B. L. (1997). The Evolution of the Altiplano-Puna plateau of the Central Andes. *Annual Review of Earth and Planetary Sciences*, *25*(1), 139–174. https://doi.org/10.1146/annurev.earth.25.1.139

Angermann, D., Klotz, J., & Reigber, C. (1999). Space-geodetic estimation of the nazca-south america euler vector. *Earth and Planetary Science Letters*, *171*(3), 329–334. https://doi.org/10.1016/S0012-821X(99)00173-9

Babeyko, A. Y., & Sobolev, S. V. (2005). Quantifying different modes of the late Cenozoic shortening in the central Andes. *Geology*, *33*(8), 621–624. https://doi.org/10.1130/G21126AR.1

Babeyko, A. Y., Sobolev, S. V., Vietor, T., Oncken, O., & Trumbull, R. B. (2006). Numerical Study of Weakening Processes in the Central Andean Back-Arc. In O. Oncken, G. Chong, G. Franz, P. Giese, H.-J. Götze, V. A. Ramos, et al. (Eds.), *The Andes* (pp. 495–512). Springer Berlin Heidelberg. Retrieved from http://link.springer.com/10.1007/978-3-540-48684-8_24

Barker, P. F. (2001). Scotia Sea regional tectonic evolution: implications for mantle flow and palaeocirculation. *Earth-Science Reviews*, *55*(1), 1–39. https://doi.org/10.1016/S0012-8252(01)00055-1

Beaumont, C., Nguyen, M. H., Jamieson, R. A., & Ellis, S. (2006). Crustal flow modes in large hot orogens. *Geological Society, London, Special Publications*, *268*(1), 91–145. https://doi.org/10.1144/GSL.SP.2006.268.01.05

Beck, S. L., & Zandt, G. (2002). The nature of orogenic crust in the central Andes: NATURE OF OROGENIC CRUST. *Journal of Geophysical Research: Solid Earth*, *107*(B10), ESE 7-1-ESE 7-16. https://doi.org/10.1029/2000JB000124

Beck, S. L., Zandt, G., Myers, S. C., Wallace, T. C., Silver, P. G., & Drake, L. (1996). Crustal-thickness variations in the central Andes. *Geology*, *24*(5), 407–410.

Bianchi, M., Heit, B., Jakovlev, A., Yuan, X., Kay, S. M., Sandvol, E., et al. (2013). Teleseismic tomography of the southern Puna plateau in Argentina and adjacent regions. *Tectonophysics*, *586*, 65–83. https://doi.org/10.1016/j.tecto.2012.11.016

Currie, C. A. (2016). The Deep Roots of the Rocky Mountains: Geophysical Studies of Western Canada. *Journal of Student Science and Technology*, *9*(1). https://doi.org/10.13034/jsst.v9i1.142

Currie, C. A., Huismans, R. S., & Beaumont, C. (2008). Thinning of continental backarc lithosphere by flow-induced gravitational instability. *Earth and Planetary Science Letters*, *269*(3), 436–447. https://doi.org/10.1016/j.epsl.2008.02.037

Dewey, J. F., & Bird, J. M. (1970). Mountain belts and the new global tectonics. *Journal of Geophysical Research (1896-1977)*, *75*(14), 2625–2647. https://doi.org/10.1029/JB075i014p02625

Garzione, C. N., Molnar, P., Libarkin, J. C., & MacFadden, B. J. (2006). Rapid late Miocene rise of the Bolivian Altiplano: Evidence for removal of mantle lithosphere. *Earth and Planetary Science Letters*, *241*(3), 543–556. https://doi.org/10.1016/j.epsl.2005.11.026

Gerya, T., & Stöckhert, B. (2006). Two-dimensional numerical modeling of tectonic and metamorphic histories at active continental margins. *International Journal of Earth Sciences*, *95*(2), 250–274. https://doi.org/10.1007/s00531-005-0035-9

Gutscher, M.-A. (2002). Andean subduction styles and their effect on thermal structure and interplate coupling. *Journal of South American Earth Sciences*, *15*(1), 3–10. https://doi.org/10.1016/S0895-9811(02)00002-0

Haberland, C., Rietbrock, A., Schurr, B., & Brasse, H. (2003). Coincident anomalies of seismic attenuation and electrical resistivity beneath the southern Bolivian Altiplano plateau. *Geophysical Research Letters*, *30*(18). https://doi.org/10.1029/2003GL017492

Heit, B., Koulakov, I., Asch, G., Yuan, X., Kind, R., Alcocer-Rodriguez, I., et al. (2008). More constraints to determine the seismic structure beneath the Central Andes at 21°S using

teleseismic tomography analysis. *Journal of South American Earth Sciences*, *25*(1), 22–36. https://doi.org/10.1016/j.jsames.2007.08.009

Horton, B. K. (2018). Tectonic Regimes of the Central and Southern Andes: Responses to Variations in Plate Coupling During Subduction. *Tectonics*, *37*(2), 402–429. https://doi.org/10.1002/2017TC004624

Ibarra, F., Liu, S., Meeßen, C., Prezzi, C. B., Bott, J., Scheck-Wenderoth, M., et al. (2019). 3D data-derived lithospheric structure of the Central Andes and its implications for deformation: Insights from gravity and geodynamic modelling. *Tectonophysics*, *766*, 453–468. https://doi.org/10.1016/j.tecto.2019.06.025

Isacks, B. L. (1988). Uplift of the Central Andean Plateau and bending of the Bolivian Orocline. *Journal of Geophysical Research: Solid Earth*, *93*(B4), 3211–3231. https://doi.org/10.1029/JB093iB04p03211

James, D. E. (1971a). Andean crustal and upper mantle structure. *Journal of Geophysical Research (1896-1977)*, *76*(14), 3246–3271. https://doi.org/10.1029/JB076i014p03246

James, D. E. (1971b). Plate Tectonic Model for the Evolution of the Central Andes. *GSA Bulletin*, *82*(12), 3325–3346. https://doi.org/10.1130/0016-7606(1971)82[3325:PTMFTE]2.0.CO;2

James, D. E., & Sacks, I. S. (1999). Cenozoic Formation of the Central Andes: A Geophysical Perspective. In *Geology and Ore Deposits of the Central Andes* (Brian J. Skinner, Vol. 7, pp. 1–25). Society of Economic Geologists.

Jordan, T. E., Isacks, B. L., Allmendinger, R. W., Brewer, J. A., Ramos, V. A., & Ando, C. J. (1983). Andean tectonics related to geometry of subducted Nazca plate. *GSA Bulletin*, *94*(3), 341–361. https://doi.org/10.1130/0016-7606(1983)94<341:ATRTGO>2.0.CO;2

Kaus, B. J. P., Mühlhaus, H., & May, D. A. (2010). A stabilization algorithm for geodynamic numerical simulations with a free surface. *Physics of the Earth and Planetary Interiors*, *181*(1–2), 12–20. https://doi.org/10.1016/j.pepi.2010.04.007

Kay, R. W., & Kay, S. M. (1993). Delamination and delamination magmatism. *Tectonophysics*, *219*(1), 177–189. https://doi.org/10.1016/0040-1951(93)90295-U

Kay, S. M., & Coira, B. L. (2009). Shallowing and steepening subduction zones, continental lithospheric loss, magmatism, and crustal flow under the Central Andean Altiplano-Puna plateau. *Geological Society of America Memoirs*, *204*, 229–259. https://doi.org/10.1130/2009.1204(11)

Kley, J., Monaldi, C. R., & Salfity, J. A. (1999). Along-strike segmentation of the Andean foreland: causes and consequences. *Tectonophysics*, *301*(1–2), 75–94. https://doi.org/10.1016/S0040-1951(98)90223-2

Kley, Jonas, & Monaldi, C. R. (1998). Tectonic shortening and crustal thickness in the Central Andes: How good is the correlation? *Geology*, *26*(8), 723–726. https://doi.org/10.1130/0091-7613(1998)026<0723:TSACTI>2.3.CO;2

Klotz, J., Khazaradze, G., Angermann, D., Reigber, C., Perdomo, R., & Cifuentes, O. (2001). Earthquake cycle dominates contemporary crustal deformation in Central and Southern Andes. *Earth and Planetary Science Letters*, *193*(3), 437–446. https://doi.org/10.1016/S0012-821X(01)00532-5

Krystopowicz, N. J., & Currie, C. A. (2013). Crustal eclogitization and lithosphere delamination in orogens. *Earth and Planetary Science Letters*, *361*, 195–207. https://doi.org/10.1016/j.epsl.2012.09.056

Lamb, S., Hoke, L., Kennan, L., & Dewey, J. (1997). Cenozoic evolution of the Central Andes in Bolivia and northern Chile. *Geological Society, London, Special Publications*, *121*(1), 237–264. https://doi.org/10.1144/GSL.SP.1997.121.01.10

Liu, S., & Currie, C. A. (2016). Farallon plate dynamics prior to the Laramide orogeny: Numerical models of flat subduction. *Tectonophysics*, *666*, 33–47. https://doi.org/10.1016/j.tecto.2015.10.010

Livermore, R., Nankivell, A., Eagles, G., & Morris, P. (2005). Paleogene opening of Drake Passage. *Earth and Planetary Science Letters*, *236*(1), 459–470. https://doi.org/10.1016/j.epsl.2005.03.027

Mackwell, S. J., Zimmerman, M. E., & Kohlstedt, D. L. (1998). High-temperature deformation of dry diabase with application to tectonics on Venus. *Journal of Geophysical Research: Solid Earth*, *103*(B1), 975–984. https://doi.org/10.1029/97JB02671

Myers, S. C., Beck, S., Zandt, G., & Wallace, T. (1998). Lithospheric-scale structure across the Bolivian Andes from tomographic images of velocity and attenuation for P and S waves. *Journal of Geophysical Research: Solid Earth*, *103*(B9), 21233–21252. https://doi.org/10.1029/98JB00956

Norabuena, E., Leffler-Griffin, L., Mao, A., Dixon, T., Stein, S., Sacks, I. S., et al. (1998). Space Geodetic Observations of Nazca-South America Convergence Across the Central Andes. *Science*, *279*(5349), 358–362. https://doi.org/10.1126/science.279.5349.358

Oncken, O., Hindle, D., Kley, J., Elger, K., Victor, P., & Schemmann, K. (2006). Deformation of the Central Andean Upper Plate System — Facts, Fiction, and Constraints for Plateau Models. In O. Oncken, G. Chong, G. Franz, P. Giese, H.-J. Götze, V. A. Ramos, et al. (Eds.), *The Andes* (pp. 3–27). Springer Berlin Heidelberg. https://doi.org/10.1007/978-3-540-48684-8_1

Pearson, D. M., Kapp, P., DeCelles, P. G., Reiners, P. W., Gehrels, G. E., Ducea, M. N., & Pullen, A. (2013). Influence of pre-Andean crustal structure on Cenozoic thrust belt kinematics and shortening magnitude: Northwestern Argentina. *Geosphere*, *9*(6), 1766–1782. https://doi.org/10.1130/GES00923.1

Poudjom Djomani, Y. H., O'Reilly, S. Y., Griffin, W. L., & Morgan, P. (2001). The density structure of subcontinental lithosphere through time. *Earth and Planetary Science Letters*, *184*(3), 605–621. https://doi.org/10.1016/S0012-821X(00)00362-9

Ramos, V., & Aleman, A. (2000). Tectonic evolution of the Andes. *Tectonic Evolution of South America. 31st Int. Geol. Cong., Rio de Janeiro, Brazil*, 453–480.

Ramos, V. A., & Folguera, A. (2009). Andean flat-slab subduction through time. *Geological Society, London, Special Publications*, *327*(1), 31–54. https://doi.org/10.1144/SP327.3

Russo, R. M., & Silver, P. G. (1996). Cordillera formation, mantle dynamics, and the Wilson cycle. *Geology*, *24*(6), 511–514. https://doi.org/10.1130/0091-7613(1996)024<0511:CFMDAT>2.3.CO;2

Schurr, B., Rietbrock, A., Asch, G., Kind, R., & Oncken, O. (2006). Evidence for lithospheric detachment in the central Andes from local earthquake tomography. *Tectonophysics*, *415*(1–4), 203–223. https://doi.org/10.1016/j.tecto.2005.12.007

Siks, B. C., & Horton, B. K. (2011). Growth and fragmentation of the Andean foreland basin during eastward advance of fold-thrust deformation, Puna plateau and Eastern Cordillera, northern Argentina. *Tectonics*, *30*(6), TC6017. https://doi.org/10.1029/2011TC002944

Silva, S. L. de. (1989). Altiplano-Puna volcanic complex of the central Andes. *Geology*, *17*(12), 1102–1106. https://doi.org/10.1130/0091-7613(1989)017<1102:APVCOT>2.3.CO;2

Sobolev, S. V., & Babeyko, A. Y. (2005). What drives orogeny in the Andes? *Geology*, *33*(8), 617–620. https://doi.org/10.1130/G21557AR.1

Sobolev, Stephan V., Babeyko, A. Y., Koulakov, I., & Oncken, O. (2006). Mechanism of the Andean Orogeny: Insight from Numerical Modeling. In O. Oncken, G. Chong, G. Franz, P. Giese, H.-J. Götze, V. A. Ramos, et al. (Eds.), *The Andes* (pp. 513–535). Springer Berlin Heidelberg. https://doi.org/10.1007/978-3-540-48684-8_25

Stern, C. R. (2004). Active Andean volcanism: its geologic and tectonic setting. *Revista Geológica de Chile*, *31*(2). https://doi.org/10.4067/S0716-02082004000200001

Tassara, A., Götze, H.-J., Schmidt, S., & Hackney, R. (2006). Three-dimensional density model of the Nazca plate and the Andean continental margin. *Journal of Geophysical Research: Solid Earth*, *111*(B9). https://doi.org/10.1029/2005JB003976

Vietor, T., & Echtler, H. (2006). Episodic Neogene Southward Growth of the Andean Subduction Orogen between 30°S and 40°S — Plate Motions, Mantle Flow, Climate, and Upper-Plate Structure. In O. Oncken, G. Chong, G. Franz, P. Giese, H.-J. Götze, V. A. Ramos, et al. (Eds.), *The Andes* (pp. 375–400). Springer Berlin Heidelberg. https://doi.org/10.1007/978-3-540-48684-8_18

Wang, H., Currie, C. A., & DeCelles, P. G. (2015). Hinterland basin formation and gravitational instabilities in the central Andes: Constraints from gravity data and geodynamic models. In *Geological Society of America Memoirs* (Vol. 212, pp. 387–406). Geological Society of America. https://doi.org/10.1130/2015.1212(19)

Ward, K. M., Delph, J. R., Zandt, G., Beck, S. L., & Ducea, M. N. (2017). Magmatic evolution of a Cordilleran flare-up and its role in the creation of silicic crust. *Scientific Reports*, *7*. https://doi.org/10.1038/s41598-017-09015-5

Whitman, D., Isacks, B. L., & Kay, S. M. (1996). Lithospheric structure and along-strike segmentation of the Central Andean Plateau: seismic Q, magmatism, flexure, topography and tectonics. *Tectonophysics*, *259*(1–3), 29–40. https://doi.org/10.1016/0040-1951(95)00130-1

Yuan, X., Sobolev, S. V., & Kind, R. (2002). Moho topography in the central Andes and its geodynamic implications. *Earth and Planetary Science Letters*, *199*(3–4), 389–402. https://doi.org/10.1016/S0012-821X(02)00589-7

Zandt, G., Velasco, A. A., & Beck, S. L. (1994). Composition and thickness of the southern Altiplano crust, Bolivia. *Geology*, *22*(11), 1003–1006. https://doi.org/10.1130/0091-7613(1994)022<1003:CATOTS>2.3.CO;2

Chapter 5

Cenozoic foreland-deformation diversity in the Altiplano-Puna plateau: Insights from 3D geodynamic modeling of the plateau-foreland shortening system

Abstract

Here, I present the first 3D geodynamic models of the plateau-foreland shortening system in the Central Andes to quantify different foreland deformation modes in the two plateau segments simultaneously. The models use robust constraints from observations and high-resolution 2D models presented in the previous chapter. Two models were computed, one with the same shortening at the Altiplano and Puna segments and another with two times larger shortening at the Altiplano segment. Both models reproduce a simple-shear shortening, caused by underthrusting of the foreland beneath the plateau, and a wide thrust belt in the weak sedimentary layer (i.e., thin-skinned tectonics) in the Altiplano segment as well as the pure-shear, thick-skinned deformation in the Puna foreland. A lateral fault zone forms in the Altiplano-Puna foreland boundary, representing the tectonic transition from northern thin-skinned to southern thick-skinned. This fault zone is much more pronounced in the model with different shortening rates between the Altiplano and Puna segments; however, it is inconsistent with the observation. We calculate the force required to drive shortening in the model where the two plateaus have the same shortening rate. Calculations show that a higher force is required to trigger the thick-skinned deformation of the Puna foreland than the thin-skinned deformation of the northern Altiplano foreland. Thus, we infer that a significant part of the tectonic shortening in the Puna section was in fact not realized in the Puna plateau or foreland but may likely have been accommodated by trench retreat. To model this process, it is necessary to include the subduction process, which is planned in future work.

5.1 Introduction

In this chapter, I develop the first 3D thermomechanical models of the plateau-foreland system in the Central Andes to determine how the Altiplano foreland and Puna foreland deform in the same model. I also investigate the effect of the shortening magnitude on the evolution of foreland deformation.

5.2 Model description

5.2.1 Model approach and setup

I use the code LaMEM to carry out thermal-mechanical calculations on an Eulerian kinematical framework, which has an 800 km * 800 km * 200 km model domain (Figure 5.1). There are more than 8.39 million grid points and 0.23 billion Lagrangian markers randomly distributes within the Eulerian mesh. Specifically, the model assigns 256 grid points in both the horizontal distance and the lateral N-S direction (3.125 km/grid point), and 128 grid points in the vertical direction with 96 points on top 90 km and 32 points on the depth below. Thus, the vertical resolution is 0.9375 km/point from the surface to a depth of 90 km and 3.4375 km/point below this depth. The resolution is sufficient to obtain the crustal-scale deformation in the 3D geodynamic model.

In setting up the 3D model, experience was used from the 2D models described in previous chapters. In particular, in the initial setup, the crust under the plateau is assumed to be as thick as 60 km with a 48-km-thick felsic portion. An additional 10-km-thick mantle lithospheric lid is set below the Altiplano crust and no mantle lithosphere under the Puna crust. In the foreland, the lithosphere is thicker and stronger, and the crust (36 km thick) is thinner than that in the plateau. The lithospheric thickness increases to 90 km in the Altiplano foreland and 70 km in the southern Puna foreland. In the Brazilian shield, the lithosphere is 150 km thick with a 36-km-thick crust. The mechanical 4-km-thick weak sediments are located in the Altiplano plateau foreland and the Brazilian shield (Figure 4.2) as suggested by Allmendinger & Gubbels, (1996) and Pearson et al., (2013). The sedimentary layer is thin (~2 km) in other areas and absent in the Santa Barbara system.

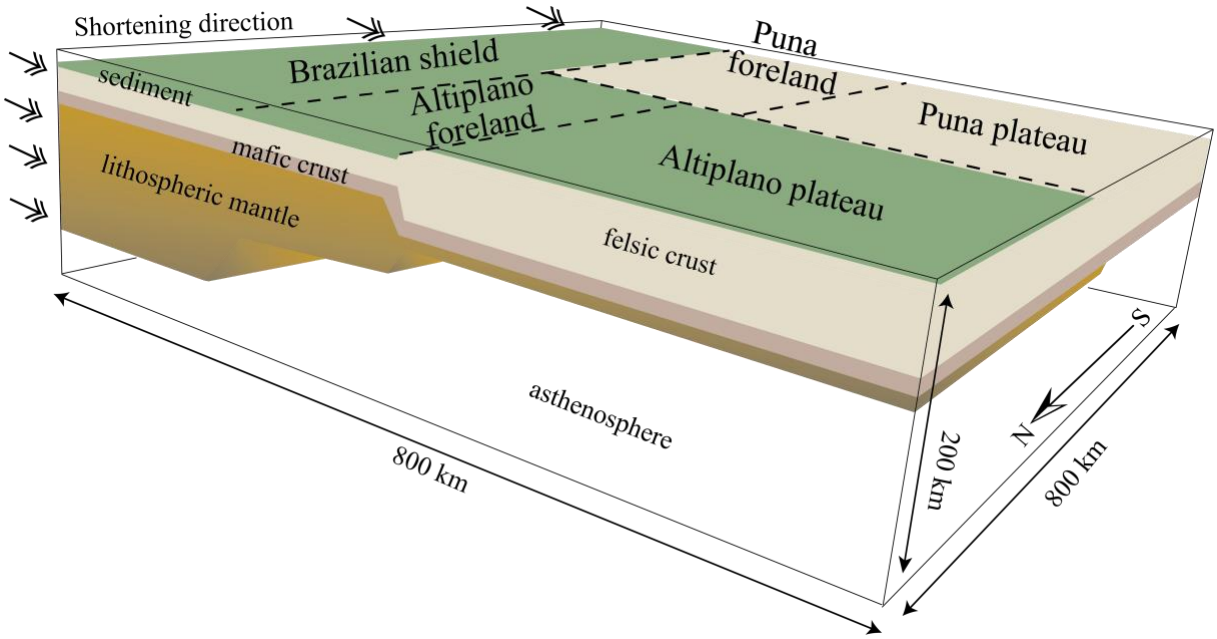

Figure 5.1. Initial 3D model setup applied to the Altiplano-Puna case. A thin lithospheric lid exists under the Altiplano plateau and is absent under the Puna plateau. There is a thick Paleozoic sedimentary basin on top of the Altiplano foreland.

5.2.2 Material properties and boundary conditions

Crustal material undergoes the frictional-plastic strain-softening through a decrease in the friction (μ) from 0.5 to 0.1 including φ from 30º to 6º and C_0 from 20 MPa to 1 MPa over an accumulated strain of 0.5 to 1.5 (Table 5.1). This approximates rock weakening due to pore fluid pressure variations, fault gouge formation and mineral reactions during deformation (e.g., Huismans & Beaumont, 2003; Babeyko & Sobolev, 2005; Beaumont et al., 2006; Liu & Currie, 2016). The plastic yield stress follows the pressure-dependent Drucker-Prager yield criterion (Equation 12 in Chapter 2).

When the deviatoric stress is below the frictional-plastic yield stress, materials undergo viscous creep deformation with an effective viscosity (η_{eff}) given by equation 11 in Chapter 2. The major creep types are known as diffusion creep, dislocation creep, and Peierls creep, which are all implemented for viscous rheology (Table 5.1). Values of viscous rheologies used here follow those of earlier studies (Babeyko et al., 2006; Sobolev et al., 2006; Liu & Currie, 2016). The laboratory-derived viscous flows of wet quartzite (Qtz_{wet}, Gleason and Tullis, 1995), dry Maryland diabase (MD_{dry}, Mackwell, et al., 1998), and dry/wet olivine (Ol_{dry}/Ol_{wet}; Hirth &

Kohlstedt, 2003) are used for the sedimentary cover and felsic crust, mafic crust, lithospheric mantle, and upper mantle, respectively. Figure 5.2 shows the viscous field for each material.

Table 5.1. Material properties in the 3D numerical models.

Phase	Sediments; Felsic crust	Mafic crust	Lithospheric mantle	Asthenosphere
Density*, ρ_0 (kg m^{-3})	2500; 2800	3000	3300	3300
Heat expansion, α (K^{-1})	3.7e-5	2.7e-5	3e-5	3e-5
Specific heat, C_p ($kJkg^{-1}K^{-1}$)	1.2	1.2	1.2	1.2
Heat conductivity, k ($W\ m^{-1}K^{-1}$)	2.5	2.5	3.3	3.3
Heat productivity, A (μW m^{-3})	1.0	0.3	0	0
Friction angle**, φ (°)	3; 30-6	30	30	30
Cohesion**, C_0 (MPa)	1; 20-1	40	40	40
Bulk, shear modulus, K, G (GPa)[1]	55, 36	63, 40	122, 74	122, 74
Creep pre-exponential factor, Bd/Bn/Bp*** ($Pa^{-n}s^{-1}$)	-/8.57e-28/-	-/5.78e-27/-	1.5e-9/6.22e-16 /6.85e-67	1e-9/2.03e-15 /6.85e-67
Creep activation energy, Ed/En/Ep*** (kJ mol^{-1})	-/223/-	-/485/-	375/480/540	335/480/540
Creep activation volume Vd/Vn/Vp*** (cm^3mol^{-1})	-/0/-	-/0/-	5/11/0	4/11/0
Power law exponent[3], n	-/4/-	-/4.7/-	1/3.5/-	1/3.5/-

*Temperature- and pressure-dependent density: $\rho_{P,T} = \rho_0[1 - \alpha(T - T_0)][1 + \frac{P-P_0}{K}]$, where ρ_0 is the reference density at temperature T_0 and pressure P_0, K is the bulk modulus.

**Strain-softening in the felsic crust via a decrease in φ and C_0 over the accumulated strain of 0.5 to 1.5; the sediment is assumed to be initially weak if φ is 3° and C_0 is 1 MPa.

***Viscous creep includes diffusion (*Bd, Ed, Vd*), dislocation (*Bn, En, Vn*), and Peierls (*Bp, Ep, Vp*).

It is assumed that the sublithospheric mantle in the asthenosphere is fertile and hydrated (wet), whereas the lithospheric mantle has undergone dehydration and melt depletion during formation (dry).

The initial thermal structure of the model is calculated by using a surface temperature of 0°C, a temperature of 1380°C at the base of the model (Figure 5.2). Thermal parameters for each material are within the range expected for crustal and mantle materials (Currie & Hyndman, 2006). Radiogenic heat production is 1.0 μW m^{-3} in the felsic crust and 0.3 μW m^{-3} in the

lower mafic crust. The thermal conductivity in the crust layer is 2.5 $W\,m^{-1}K^{-1}$ and then increases to 3.3 $W\,m^{-1}K^{-1}$ down to the mantle. This artificial conductivity from previous models (Pysklywec & Beaumont, 2004) mimics heat transportation by upper mantle convection without additional model convective motions.

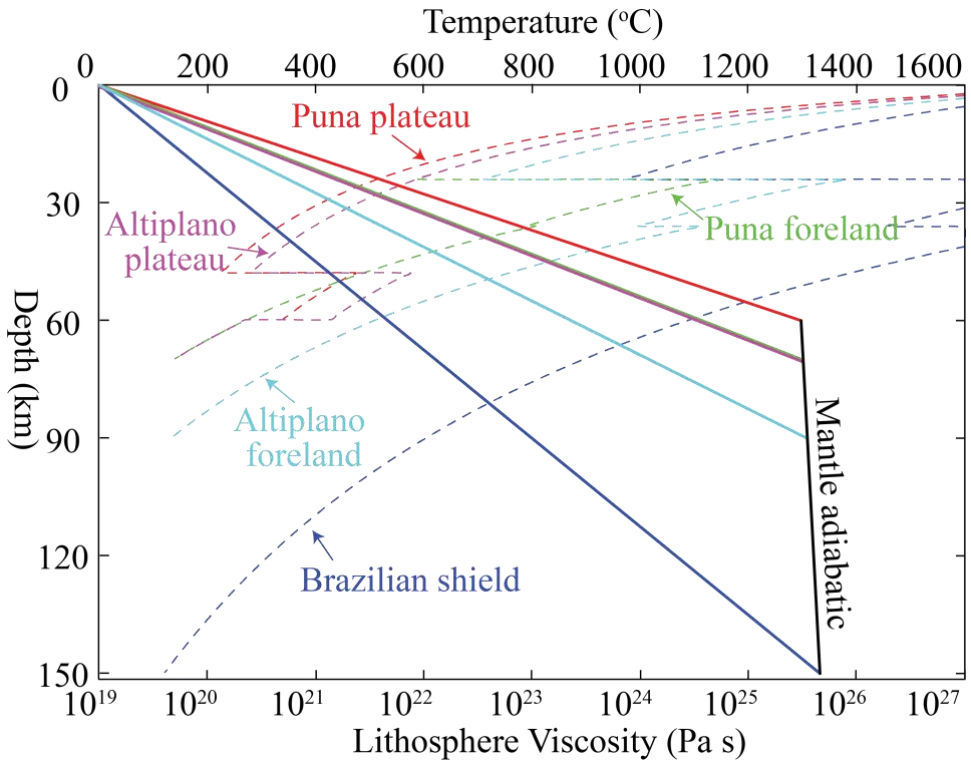

Figure 5.2. Initial temperature field (solid line) and viscosity field (dashed line) of each phase's lithosphere applied to the 3D Altiplano-Puna case.

Mechanical boundary conditions include: 1) a free surface, which uses a low-density, low-viscosity sticky air layer on top to allow the development of topography in response to the underlying dynamics, 2) a free slip basal boundary, 3) no vertical velocity on the side boundaries, 4) an inflow velocity on the foreland lithosphere on the left-hand boundary to drive the shortening, 5) an outflow velocity under the lithosphere on the right-hand boundary. This outflow can maintain the mass balance in the model domain.

5.3 Results

Two 3D thermomechanical models with different magnitudes of shortening are computed. Model S1 has the same amount of shortening on both the Altiplano and the Puna by imposing

a constant shortening rate on the left side boundary close to the Brazilian shield. In Model S2, the lithospheric shortening in the Altiplano is double that of the shortening in the Puna.

5.3.1 Same amounts of shortening on segments of the Altiplano and the Puna

In Model S1, 200-km-shortening is applied to both the Altiplano plateau-foreland system as and the Puna system. During shortening, the Altiplano foreland underthrusts beneath its plateau, accompanied by a wedge-shaped thrust belt in the top sedimentary layer (i.e., thin-skinned deformation; Figure 5.3b and Figure 5.4a). As a result, a strong crustal flow forms at the bottom of the felsic crust under the Altiplano plateau (Figure 5.4c). The crust intrudes from the foreland into the plateau, causing the crustal thickening under the plateau. Since there is no mechanically weak in the Puna foreland, it is thinner than the Altiplano foreland. The deformation there occurs in the entire felsic crust from the surface to the deep basement in the pure-shear deformation mode with fully thick-skinned tectonics (Figure 5.4b).

After shortening, the entire Altiplano-Puna plateau forms a high topography while the topography of its foreland is low and flat (Figure 5.3a). The average elevation difference between them is about 4-5 km. This is more than 1 km higher than the observed elevation (Figure 4.2). A lateral deformation transition zone is formed in the foreland boundary between the Altiplano and the Puna, indicating a 3D character of the plateau-foreland compressional system (Figure 5.3b). With the change of structural style, the magnitude of crustal flow under the plateau gradually decreases from the Altiplano to the Puna causing a reduction of crustal thickening from the Altiplano to the Puna. As a result, the Altiplano plateau crust becomes thicker than the Puna plateau crust, which agrees with present observation. Note that, the east-dipping reverse fault form in front of the Puna foreland in our model is agreement with observations (Kley et al., 1999).

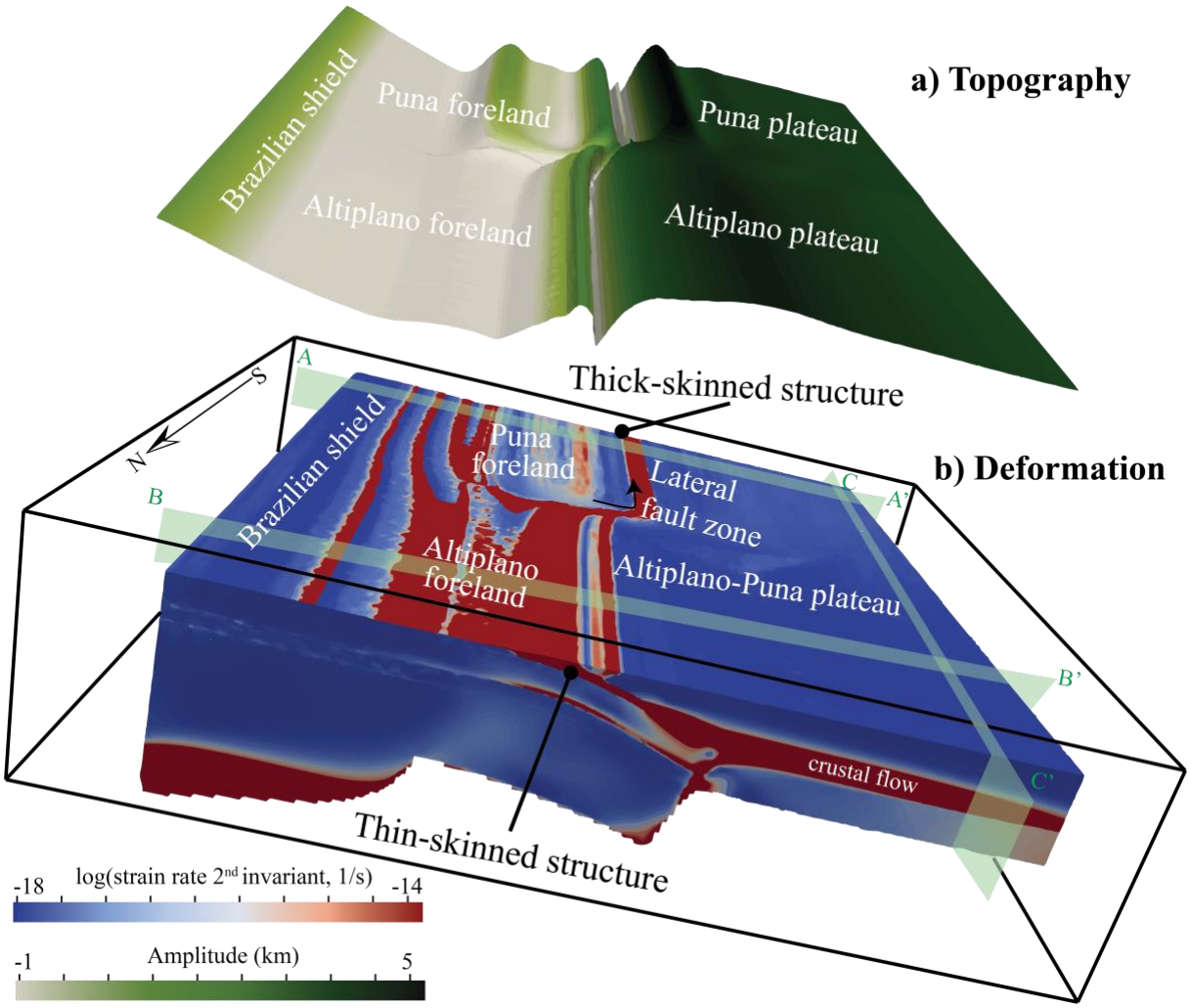

Figure 5.3. 3D numerical model of the Altiplano-Puna plateau-foreland system after 200 km shortening. **a)** Surface topography of the plateau and its foreland. **b)** Deformation of the plateau and its foreland, including a thin-skinned thrust in Altiplano foreland and a thick-skinned structure in Puna foreland. A lateral deformation transition zone locates in the boundary between the Altiplano foreland and the Puna foreland.

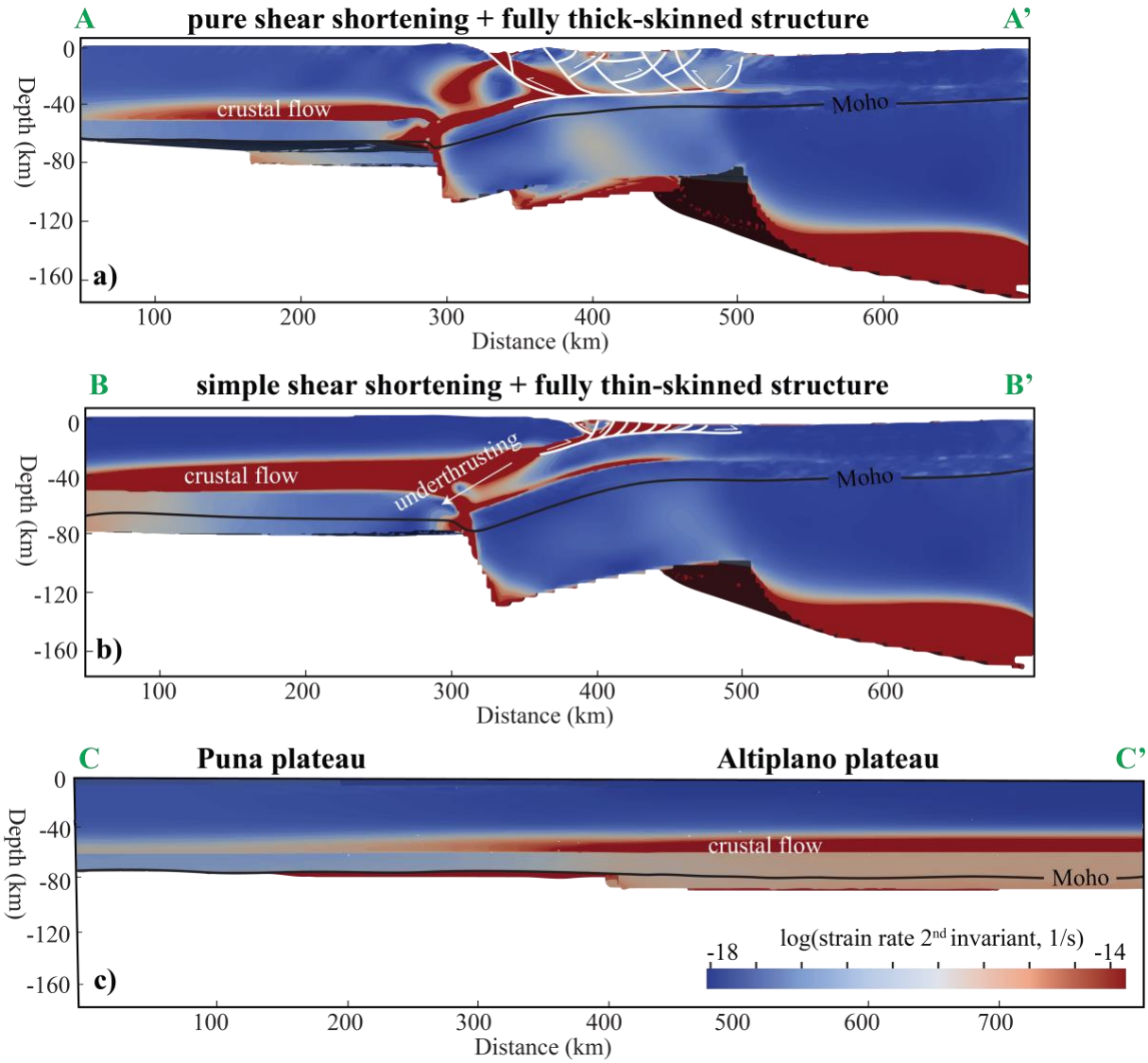

Figure 5.4. Three cross-sections of model deformation in Figure 5.3. a) A-A' cross-section shows the deformation pattern in the Altiplano case. B) B-B' cross-section shows the deformation pattern in the Puna case. C) C-C' cross-section shows that crustal flow under the plateau gradually decreases, and thus the crustal thickening reduces from the Altiplano plateau to the Puna plateau.

5.3.2 Different amounts of shortening on segments of the Altiplano and the Puna

In the last 10 Ma, the amount of shortening in the Puna plateau-foreland system is approximately half of the shortening of the Altiplano system (Figure 4.2; Oncken, et al., 2006). Therefore, Model S2 addresses the evolution of foreland deformation with a different rate of shortening between the Altiplano and the Puna sections (Figure 5.5b). The thick Brazilian

Shield lithosphere is removed in this model. Therefore, there is no lithospheric strength difference between the preexistent shield and the foreland. Unlike Model S1, there is no localized deformation at the boundary between the shield and foreland in Model S2. However, similar to Model S1, Model S2 also shows a simple-shear shortening with the fully thin-skinned thrust belt in the Altiplano foreland. Meanwhile, a thick-skinned structure with faults penetrating deep into the basement rocks forms in the Puna foreland with little underthrusting (i.e., pure-shear shortening mode).

There is also a lateral fault zone formed in the boundary between two forelands. This zone shows an N-S structural transition from a northern thin-skinned to a southern thick-skinned. Since the model only simulates 100 km shortening on the Puna side, the Puna foreland deformation zone is narrower in Model S2 than that in Model S1. Correspondingly, the topography of the entire Puna plateau-foreland is lower in this model (Figure 5.5a). The average elevation difference between the plateau and its foreland is about 3.5-4.5 km here, which matches the observed elevation.

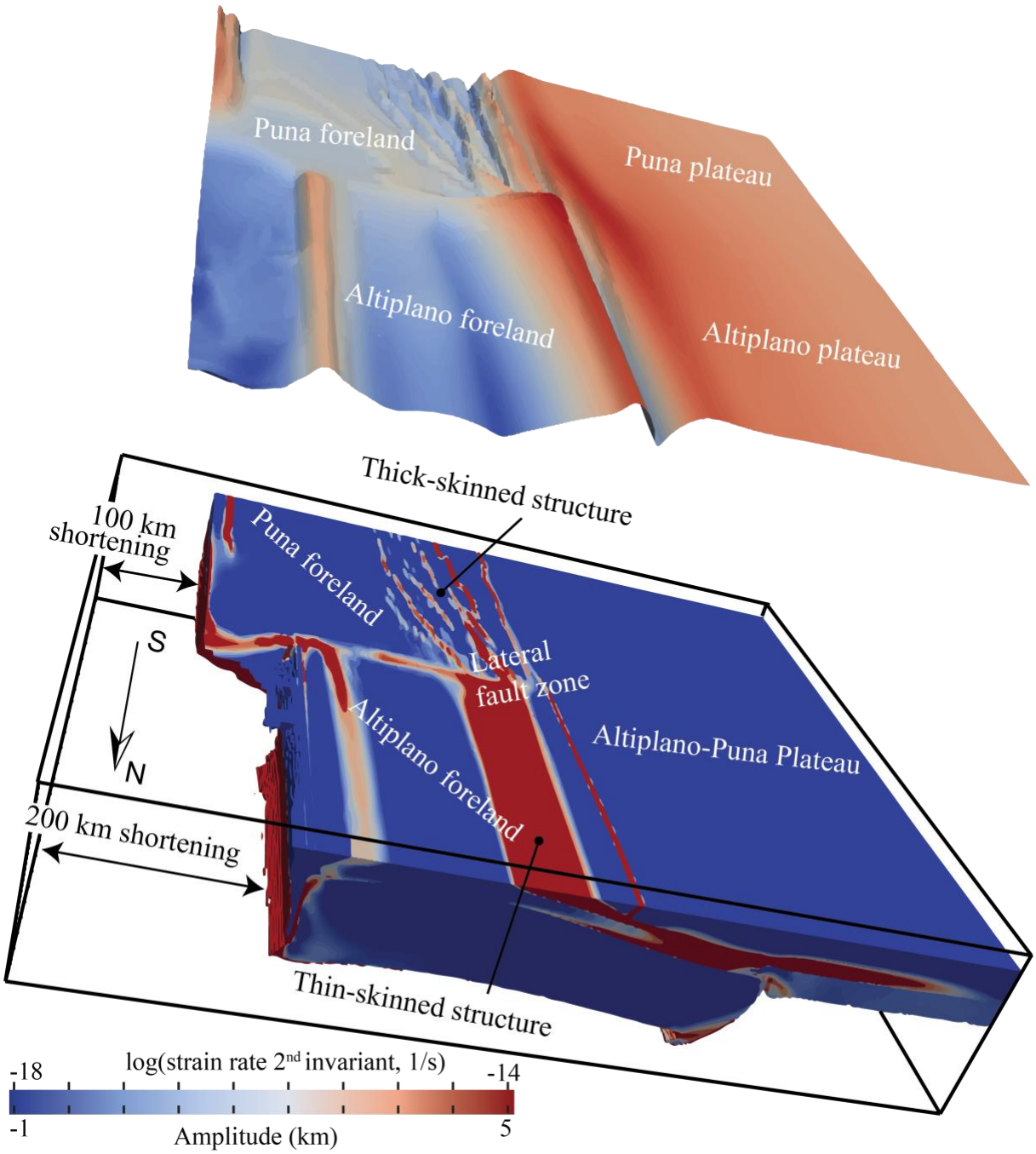

Figure 5.5. 3D numerical model of the Altiplano-Puna plateau-foreland system with different shortening amounts in the sections of the Altiplano and Puna. **a)** Surface topography of the plateau and its foreland. **b)** Deformation of the plateau and its foreland, induced by 200 km shortening in the Altiplano section and 100 km shortening in the Puna section. There is a thin-skinned thrust in the Altiplano foreland and a thick-skinned structure in the Puna foreland. A lateral deformation transition zone locates in the boundary between the Altiplano foreland and the Puna foreland.

5.4 Discussion

The results of our 3D models show that the foreland-deformation diversity can be reproduced regardless of the different or same amount of shortening in the back-arc of the two segments of the Central Andes. Therefore, the difference of magnitudes of shortening has little effect on the types of foreland deformation in the Altiplano-Puna plateau. Instead, the existence of a weak, thick sedimentary basin in the foreland and the lithospheric strength difference between the plateau and its foreland play a crucial role in the deformation diversity. This result is consistent with the suggestions from our high-resolution 2D model in Chapter 3.

A long lateral fault zone is formed in the Altiplano-Puna foreland boundary in our model with different shortening rates in the Altiplano and Puna sections, representing the structural transition from the northern thin-skinned to the southern thick-skinned. However, in nature, the W-E width of the lateral fault is very narrow and mainly exists in the east edge of Eastern Cordillera (Siks & Horton, 2011). There is no fault at the N-S transition zone from the Subandean Ranges to the Santa Barbara System between 23°S and 24°S, even though it is considered as the transition zone from thin-skinned to thick-skinned deformation (Kay & Coira, 2009). In this respect, Model S1, with the same shortening rate at the Altiplano and Puna sections fits the observations better. Why then does shortening in the Puna foreland appears to be much less than in the Altiplano foreland? To answer this question, I examine forces that drive shortening in Model S1.

I calculate the force (F) necessary to drive the shortening at a constant bulk rate in the foreland-side boundary by using the equation below, which has also been used in previous studies (Babeyko & Sobolev, 2005):

$$F = \int_0^h (\tilde{\sigma}_{xx}) dz \qquad (15)$$

where h is the thickness of the foreland lithosphere, $\tilde{\sigma}_{xx}$ is the horizontal deviatoric stress, z is the depth.

Figure 5.6 shows the evolution of the driving force in the Model S1. When the shortening rate remains constant, more forces are required to trigger the thick-skinned deformation in the Puna foreland than the thin-skinned deformation in the northern Altiplano foreland. In the Altiplano

case, the force rapidly decreases from 7.4*10$_{12}$ N/m to 5.4*10$_{12}$ N/m before 2.8 Ma. In this period, the foreland underthrusts beneath the plateau as an expression of simple-shear shortening. Later, it turns harder for the foreland to inject deeper and further into the plateau. Therefore, the force is required to increase to maintain the same shortening rate. The same behavior but the opposite ascending and descending trend occurs in the Puna case. From another perspective, if the driving force is constant (i.e., the contraction forces from the Brazilian shield to the Subandean Ranges and the Santa Barbara System are the same magnitudes), then the shortening rate is higher in the Altiplano case than that in the Puna case. As a result, the Altiplano backarc area should have a larger amount of shortening than the Puna backarc in the same period. The force balance implies a greater force is transmitted to the fore-arc in the Puna section than in the Altiplano section. From that, we infer that a significant part of the tectonic shortening in the Puna section was, in fact, not realized in the Puna plateau or foreland but may be localized in the fore-arc and likely have been accommodated by trench retreat. To model this process, it is required to include the western subduction process, which is planned in future work.

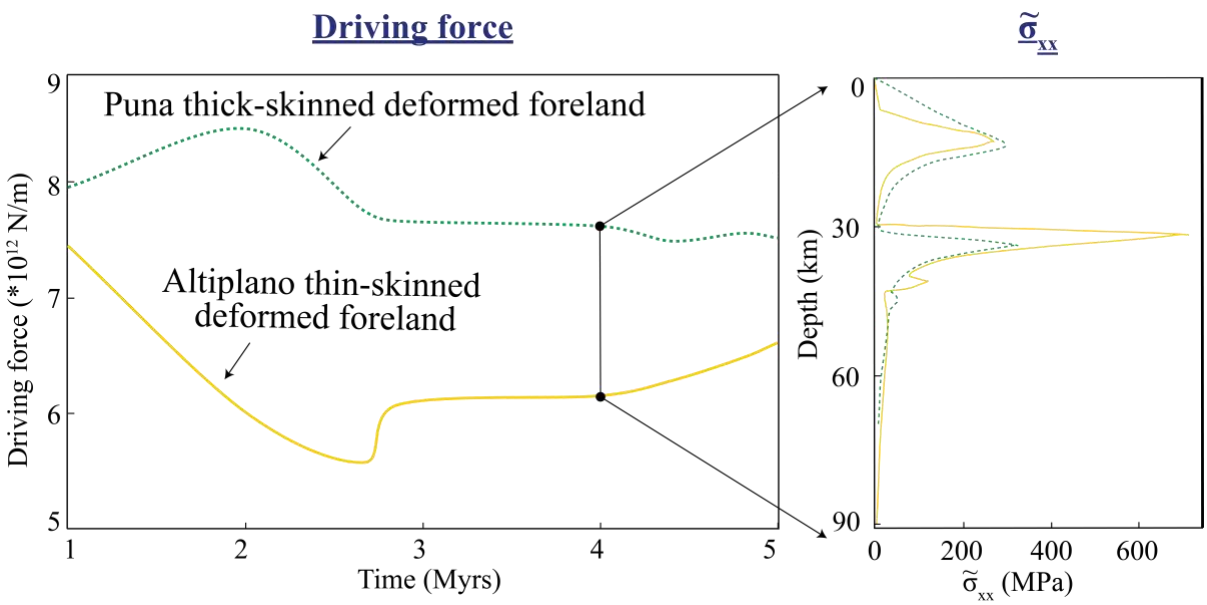

Figure 5.6. The external driving force necessary to drive shortening at a constant bulk rate in the model S1. More force is required in the Puna section where the thick-skinned deformation occurs. Black solid circle - horizontal deviatoric stress $\tilde{\sigma}_{xx}$ distribution through depth at the boundaries of the Puna foreland (green) and the Altiplano foreland (yellow) at a specific computing time.

5.5 Conclusions

We develop the first 3D geodynamic models of the Altiplano-Puna plateau-foreland shortening system to investigate the foreland-deformation diversity. The following conclusions may be drawn:

(1) A fully thin-skinned thrust wedge, accompanied with the simple-shear underthrusting, forms in the weak, thick Paleozoic sedimentary layer of the Altiplano foreland. The Puna foreland undergoes pure-shear shortening with a fully thick-skinned structure due to its thinner lithosphere than in the northern Altiplano foreland and the absence of weak sediments. There is more felsic crust from the foreland intruding into the bottom of the plateau crust in the Altiplano than in the Puna, resulting in a thicker Altiplano plateau crust.

(2) Results of the 3D models with different shortening rates in the Altiplano and Puna segments show that there should be a long lateral fault zone in the Altiplano-Puna foreland boundary, implying the structural transition from the northern thin-skinned to southern thick-skinned. However, such a fault zone is not observed.

(3) Calculations show that the driving force for a constant shortening rate is greater in the Puna than in the Altiplano. From that, we infer that a significant part of the tectonic shortening in the Puna section was in fact not realized in the Puna plateau or foreland but may have been accommodated by trench retreat.

References

Allmendinger, R. W., & Gubbels, T. (1996). Pure and simple shear plateau uplift, Altiplano-Puna, Argentina and Bolivia. *Tectonophysics*, *259*(1), 1–13. https://doi.org/10.1016/0040-1951(96)00024-8

Babeyko, A. Y., & Sobolev, S. V. (2005). Quantifying different modes of the late Cenozoic shortening in the central Andes. *Geology*, *33*(8), 621–624. https://doi.org/10.1130/G21126AR.1

Babeyko, A. Y., Sobolev, S. V., Vietor, T., Oncken, O., & Trumbull, R. B. (2006). Numerical Study of Weakening Processes in the Central Andean Back-Arc. In O. Oncken, G. Chong, G. Franz, P. Giese, H.-J. Götze, V. A. Ramos, et al. (Eds.), *The Andes* (pp. 495–512). Springer Berlin Heidelberg. Retrieved from http://link.springer.com/10.1007/978-3-540-48684-8_24

Beaumont, C., Nguyen, M. H., Jamieson, R. A., & Ellis, S. (2006). Crustal flow modes in large hot orogens. *Geological Society, London, Special Publications*, *268*(1), 91–145. https://doi.org/10.1144/GSL.SP.2006.268.01.05

Beck, S. L., & Zandt, G. (2002). The nature of orogenic crust in the central Andes: NATURE OF OROGENIC CRUST. *Journal of Geophysical Research: Solid Earth*, *107*(B10), ESE 7-1-ESE 7-16. https://doi.org/10.1029/2000JB000124

Beck, S. L., Zandt, G., Myers, S. C., Wallace, T. C., Silver, P. G., & Drake, L. (1996). Crustal-thickness variations in the central Andes. *Geology*, *24*(5), 407–410.

Currie, C. A., & Hyndman, R. D. (2006). The thermal structure of subduction zone back arcs. *Journal of Geophysical Research: Solid Earth*, *111*(B8), B08404. https://doi.org/10.1029/2005JB004024

Gleason, G. C., & Tullis, J. (1995). A flow law for dislocation creep of quartz aggregates determined with the molten salt cell. *Tectonophysics*, *247*(1), 1–23. https://doi.org/10.1016/0040-1951(95)00011-B

Haberland, C., Rietbrock, A., Schurr, B., & Brasse, H. (2003). Coincident anomalies of seismic attenuation and electrical resistivity beneath the southern Bolivian Altiplano plateau. *Geophysical Research Letters*, *30*(18). https://doi.org/10.1029/2003GL017492

Hirth, G., & Kohlstedt, D. (2003). Rheology of the upper mantle and the mantle wedge: A view from the experimentalists. *Washington DC American Geophysical Union Geophysical Monograph Series*, *138*, 83–105. https://doi.org/10.1029/138GM06

Horton, B. K. (2018). Tectonic Regimes of the Central and Southern Andes: Responses to Variations in Plate Coupling During Subduction. *Tectonics*, *37*(2), 402–429. https://doi.org/10.1002/2017TC004624

Huismans, R. S., & Beaumont, C. (2003). Symmetric and asymmetric lithospheric extension: Relative effects of frictional-plastic and viscous strain softening. *Journal of Geophysical Research: Solid Earth*, *108*(B10), 2496. https://doi.org/10.1029/2002JB002026

Kay, S. M., & Coira, B. L. (2009). Shallowing and steepening subduction zones, continental lithospheric loss, magmatism, and crustal flow under the Central Andean Altiplano-Puna plateau. *Geological Society of America Memoirs*, *204*, 229–259. https://doi.org/10.1130/2009.1204(11)

Kley, J., Monaldi, C. R., & Salfity, J. A. (1999). Along-strike segmentation of the Andean foreland: causes and consequences. *Tectonophysics*, *301*(1–2), 75–94. https://doi.org/10.1016/S0040-1951(98)90223-2

Liu, S., & Currie, C. A. (2016). Farallon plate dynamics prior to the Laramide orogeny: Numerical models of flat subduction. *Tectonophysics*, *666*, 33–47. https://doi.org/10.1016/j.tecto.2015.10.010

Mackwell, S. J., Zimmerman, M. E., & Kohlstedt, D. L. (1998). High-temperature deformation of dry diabase with application to tectonics on Venus. *Journal of Geophysical Research: Solid Earth*, *103*(B1), 975–984. https://doi.org/10.1029/97JB02671

Myers, S. C., Beck, S., Zandt, G., & Wallace, T. (1998). Lithospheric-scale structure across the Bolivian Andes from tomographic images of velocity and attenuation for P and S waves. *Journal of Geophysical Research: Solid Earth*, *103*(B9), 21233–21252. https://doi.org/10.1029/98JB00956

Oncken, O., Hindle, D., Kley, J., Elger, K., Victor, P., & Schemmann, K. (2006). Deformation of the Central Andean Upper Plate System — Facts, Fiction, and Constraints for Plateau Models. In O. Oncken, G. Chong, G. Franz, P. Giese, H.-J. Götze, V. A. Ramos, et al. (Eds.), *The Andes* (pp. 3–27). Springer Berlin Heidelberg. https://doi.org/10.1007/978-3-540-48684-8_1

Oncken, O., Chong, G., Franz, G., Giese, P., Götze, H.-J., Ramos, V. A., et al. (2006). *The Andes: Active Subduction Orogeny*. Springer Science & Business Media.

Pearson, D. M., Kapp, P., DeCelles, P. G., Reiners, P. W., Gehrels, G. E., Ducea, M. N., & Pullen, A. (2013). Influence of pre-Andean crustal structure on Cenozoic thrust belt kinematics and shortening magnitude: Northwestern Argentina. *Geosphere*, *9*(6), 1766–1782. https://doi.org/10.1130/GES00923.1

Pysklywec, R. N., & Beaumont, C. (2004). Intraplate tectonics: feedback between radioactive thermal weakening and crustal deformation driven by mantle lithosphere instabilities. *Earth and Planetary Science Letters*, *221*(1), 275–292. https://doi.org/10.1016/S0012-821X(04)00098-6

Schurr, B., Rietbrock, A., Asch, G., Kind, R., & Oncken, O. (2006). Evidence for lithospheric detachment in the central Andes from local earthquake tomography. *Tectonophysics*, *415*(1–4), 203–223. https://doi.org/10.1016/j.tecto.2005.12.007

Siks, B. C., & Horton, B. K. (2011). Growth and fragmentation of the Andean foreland basin during eastward advance of fold-thrust deformation, Puna plateau and Eastern Cordillera, northern Argentina. *Tectonics*, *30*(6), TC6017. https://doi.org/10.1029/2011TC002944

Sobolev, S. V., Babeyko, A. Y., Koulakov, I., & Oncken, O. (2006). Mechanism of the Andean Orogeny: Insight from Numerical Modeling. In O. Oncken, G. Chong, G. Franz, P.

Giese, H.-J. Götze, V. A. Ramos, et al. (Eds.), *The Andes* (pp. 513–535). Springer Berlin Heidelberg. https://doi.org/10.1007/978-3-540-48684-8_25

Tassara, A., Götze, H.-J., Schmidt, S., & Hackney, R. (2006). Three-dimensional density model of the Nazca plate and the Andean continental margin. *Journal of Geophysical Research: Solid Earth*, *111*(B9). https://doi.org/10.1029/2005JB003976

Whitman, D., Isacks, B. L., & Kay, S. M. (1996). Lithospheric structure and along-strike segmentation of the Central Andean Plateau: seismic Q, magmatism, flexure, topography and tectonics. *Tectonophysics*, *259*(1–3), 29–40. https://doi.org/10.1016/0040-1951(95)00130-1

Yuan, X., Sobolev, S. V., Kind, R., Oncken, O., Bock, G., Asch, G., et al. (2000). Subduction and collision processes in the Central Andes constrained by converted seismic phases. *Nature*, *408*(6815), 958–961. https://doi.org/10.1038/35050073

Chapter 6

3D data-derived lithospheric structure of the Central Andes and its implications for deformation: Insights from gravity and geodynamic modeling

A version of this chapter has been published on the journal *Tectonophysics* as Ibarra, F., Liu, S., Meeßen, C., Prezzi, C. B., Bott, J., Scheck-Wenderoth, M., Sobolev, S., Strecker, M.R., 3D data-derived lithospheric structure of the Central Andes and its implications for deformation: insights from gravity and geodynamic modeling. 766, 453–468. https://doi.org/10.1016/j.tecto.2019.06.025.

Abstract

This study was done in cooperation with another STRATEGY project. The principal aim of this study is to assess the link between heterogeneities in the lithosphere and different deformation patterns and styles in the orogen-foreland system of the Central Andes. Our cooperation partners performed a 3D integration of new geological and geophysical data with previous models through forward modelling of Bouguer anomalies. We have set-up a geodynamic model using the previously obtained 3D structure and composition. We do not find an unambiguous correlation between the resulting density configuration and terrane boundaries proposed by other authors. Our models reproduce the observed Bouguer anomaly and deformation patterns in the foreland. We find that thin-skinned deformation in the Subandean fold-and thrust belt is controlled by a thick sedimentary layer and coeval underthrusting of thin crust of the foreland beneath the thick crust of the Andean Plateau. In the adjacent thick-skinned deformation province of the inverted Cretaceous extensional Santa Barbara System sedimentary strata are much thinner and crustal thickness transitions from greater values in the Andean to a more reduced thickness in the foreland. Our results show that deformation processes occur where the highest gradients of lithospheric strength are present between the orogen and the foreland, thus suggesting a spatial correlation between deformation and lithospheric strength.

6.1 Introduction

In this study we address the impact of the lithospheric density configuration in the Central Andes and adjacent foreland basin (Figure 6.1) on the observed present-day deformation pattern. 3D density model is derived from lithology and seismic velocity, and main structural interfaces are based on independent datasets. The model is constrained through forward modelling of the Bouguer anomaly (Ibarra et al, 2019). Here we present a geodynamic model for continental intraplate present-day shortening using the interfaces and composition in that density model. Additionally, we compare our results with the existing terrane models (Ramos, 2008; Ramos et al., 2010) to test if there is any correlation.

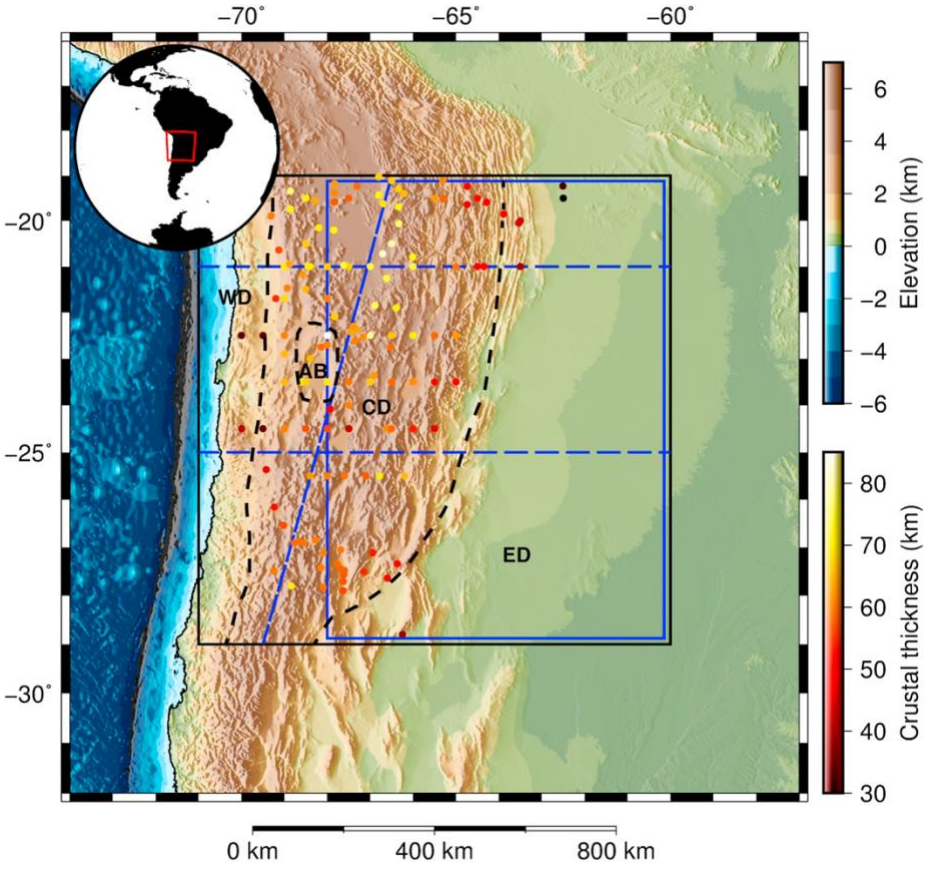

Figure 6.1. Elevation map of South America showing the location of the gravity modeling region (black rectangle) and the geodynamic modeling region (blue rectangle; Figure 6.2). Blue stippled lines show the location of three cross-sections across the models (Figure 6.3 and Figure 6.4b–c). Stippled black lines represent boundaries between crustal domains used in this study (WD: Western Domain; CD: Central Domain; ED: Eastern Domain; AB: Atacama Block). Color-coded points indicate crustal thickness constraints from seismic studies (Assumpção et al., 2013).

6.2 Geodynamic model description

The 3D density distribution (Ibarra et al., 2019) is used to perform a geodynamic simulation for continental intraplate shortening with application to the central Andes.

The geodynamic model is developed to assess the dynamic behavior of the density model (Ibarra et all., 2019) and the back-arc deformation patterns in the Central Andes. The deformation structural styles in the foreland are different between the Altiplano and the Puna regions. This heterogeneity in deformation is suggested to be related to different modes of the late Cenozoic shortening and distinct crustal structures in the plateau and its foreland (e.g., Allmendinger & Gubbels, 1996). Therefore, here we focus on the present-day shortening of the orogen-foreland system in the Central Andes by using the crustal structures from the density model as the initial configuration of the geodynamic model.

We use the highly scalable advanced geodynamic code LaMEM (Lithosphere and Mantle Evolution Model; Kaus et al., 2016) to develop the thermo-mechanical model. The model domain contains the orogen (Central Domain) and the foreland (Eastern Domain) in the back-arc region of the density model, spanning from 68° W to 60° W and from 19° S to 29° S (Figure 6.2). The lithosphere-asthenosphere boundary (LAB) defining the lithospheric mantle in the model was interpolated from the global model of (Koptev & Ershov, 2011) using the Moho as an upper boundary. The resolution of the model in the latitude and longitude directions is 7 km and 6 km per grid, respectively. Since the sedimentary layer is thin, sufficient grid points are required to track the deformation of sediments in the vertical direction; thus, we use a dense grid with 1.2 km vertical resolution covering the lithosphere down to 200 km depth. For the lower 200 km depth the vertical resolution is 7 km.

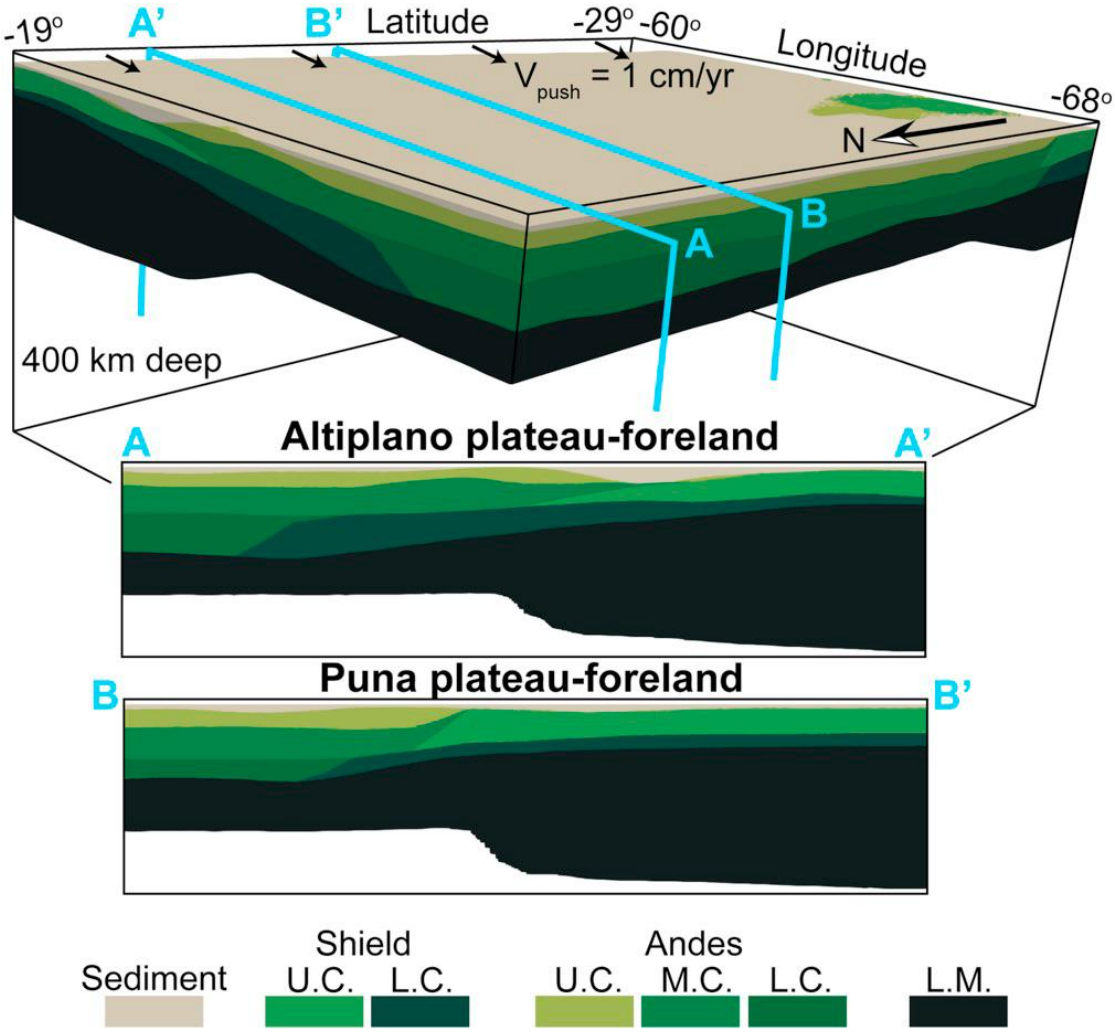

Figure 6.2. Initial setup of the 3D data-derived geodynamic model. The crustal structure is configured from the density model. U.C., M.C., L.C. and L.M. are upper crust, middle crust, lower crust and lithospheric mantle respectively.

For the parametrization of the geodynamic model, thermal properties are taken from average values for the lithological composition of each unit (Čermák & Rybach, 1982; Vilà et al., 2010) and mechanical properties from published experimental studies (Table 6.1). For all materials a fully visco-elasto-plastic rheology is considered, and the mechanisms of ductile deformation include diffusion, dislocation, and Peierls creep regimes (Table 6.1). The laboratory-derived viscous flow laws of wet quartzite (Ranalli & Murphy, 1987), dry granite, dry quartz diorite, dry felsic granulite (Wilks & Carter, 1990), and dry/wet olivine (Hirth & Kohlstedt, 2003) were implemented for the sedimentary cover, upper and middle crust in the Central Domain, upper crust in the Eastern Domain, lower crust in both domains, and lithospheric/sublithospheric mantle, respectively.

Materials in the upper-middle crust undergo frictional-plastic strain softening through a decrease in the friction coefficient from 0.5 to 0.1 over the accumulated strain of 0.5 to 1.5 based on the experience of previous geodynamic models (e.g., Sobolev et al., 2006; Liu & Currie, 2016). We consider that sediments with the friction coefficient value 0.05 are weaker than the crust below. The friction drop of sediments may be the result of the high pore-fluid pressure (lowering the effective confining stress) due to the local wet condition in the Andes (e.g., Strecker et al., 2007).

Table 6.1. Thermo-mechanical properties used in the geodynamic model.

Model unit	Type rheology	Power-law activation energy, Q (kJ mol^{-1})	Power-law strain rate, A (Pa^{-n}S^{-1})	Power-law exponent, n	Thermal conductivity, λ (W m^{-1}K^{-1})	Radiogenic heat production, S (W m^{-3})
Sediments	Wet quartzite	154	4.00E-18	2.3	2.4	0.9
Upper Crust Eastern Domain	Dry quartz diorite	219	5.02E-18	2.4	2.9	1.2
Upper Crust Central Domain	Dry granite	123	7.93E-29	3.2	2.9	1.8
Middle Crust Central Domain	Dry granite	123	7.93E-29	3.2	2.9	1.6
Lower Crust Eastern Domain	Dry felsic granulite	243	2.01E-21	3.1	2.6	0.6
Lower Crust Central Domain	Dry felsic granulite	243	2.01E-21	3.1	2.7	0.8
Lithospheric mantle	Dry olivine	375/530/540	1.50E03/1.10E-16/6.85E-67	1/3.5/-	3.1	0.02
Sublithospheric mantle	Wet olivine (Constant C_{OH})	335/480/540	1.00/9.00E-20/6.85E-67	1/3.5/-	3.1	0.02

The thermo-mechanical boundary conditions include a stress-free surface boundary with a 0 °C temperature at the top, and a closed free-slip boundary with a temperature of 1460°C at the bottom. The thermal gradient at the side boundaries is set to zero, which means no horizontal heat flux. The amount of intraplate shortening is imposed through a velocity of 1 cm/yr (Oncken et al., 2006) on the right-hand (East) side boundary. Mass balance is maintained using a uniform outflow through the left-hand (West) side boundary below the lithosphere of the Andes.

6.3 Results

6.3.1 Gravity-constrained model

The final 3D density structure is obtained from integrated forward gravity modelling reproduces the gravity anomalies well (Figure 3 and 8 in the Ibarra et al. (2019)). We also obtain the thickness distribution of surface sediments and underlying crust (Figure 5 and 7 in the Ibarra et al. (2019)). In Figure 6.3, we present cross sections perpendicular to the orogen across the model at 21°S (Altiplano; Figure 6.3a) and 26°S (Puna; Figure 6.3b), and an NNE-SSW striking cross section through the orogen from ~67°W in the north to ~69°W in the south (Figure 6.3c). The cross sections show the distribution of the domains through the model. There is a rough spatial correlation between the domains and the morphotectonic units; the Western Domain covers the Coastal Cordillera and part of the Chilean Precordillera, the Central Domain extents from the Chilean Precordillera to the deformed foreland and the Eastern Domain covers the foreland. Comparing the cross sections in the north and south (Figure 6.3a-b), we observe the trends described also in the thickness maps (Figure 5 in Ibarra et al. (2019)). The sediment thickness in the foreland and the thickness of the lower crust in the orogen are larger to the north. Figure 6.3c clearly shows the increasing Moho depth from south to north.

6.3.2 Geodynamic modeling

Figure 6.4 shows the distribution of strain rate norm (square root of the second invariant of the deviatoric strain rate) which characterizes the dynamics of changes in the internal deformation during compression. After 3.3 km shortening, the deformation zone is mainly localized in the eastern margin of the Subandean Ranges and the transition from the Eastern Cordillera to the Santa Barbara System (Figure 6.4a). As we are interested in crustal deformation, we plot our modelling results in a zoom-in area encompassing the top 90 km of the model along two cross-sections through the Altiplano and the Puna (Figure 6.4b-c). The horizontal distance in the plotted area is limited to 600 km to avoid the effect of lateral boundary conditions on the modelling results. The foreland crust underthrusts below the Altiplano plateau, resulting in the development of a thin-skinned structure in its thick and weak sediments (Figure 6.4b). In contrast, no crustal underthrusting beneath the Puna plateau is observed and a thick-skinned structure is formed (Figure 6.4c). Interestingly, in both cross-sections, the crustal thickening

due to the tectonic shortening occurs along the eastern edge of the plateau rather than inside the weak plateau crust.

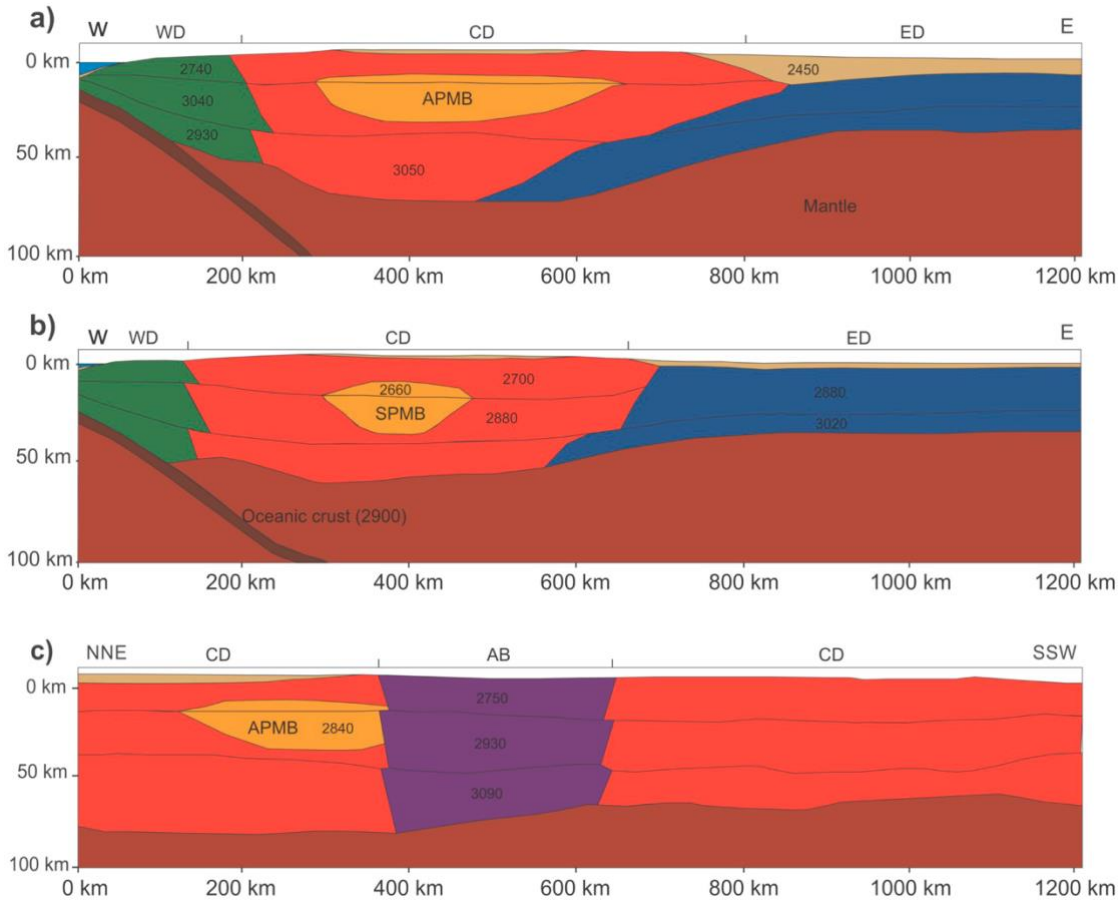

Figure 6.3. Cross-sections of the model, locations are depicted in Figure 1. WD: Western Domain; CD: Central Domain; ED: Eastern Domain; AB: Atacama Block; APMB: Altiplano-Puna Magma Body; SPMB: Southern Puna Magma Body. Densities are in kg/m3. **a)** Structure perpendicular to the orogen along the Altiplano transect (~21°S); **b)** structure perpendicular to the orogen along the Puna transect (~25°S); **c)** structure parallel to the orogen.

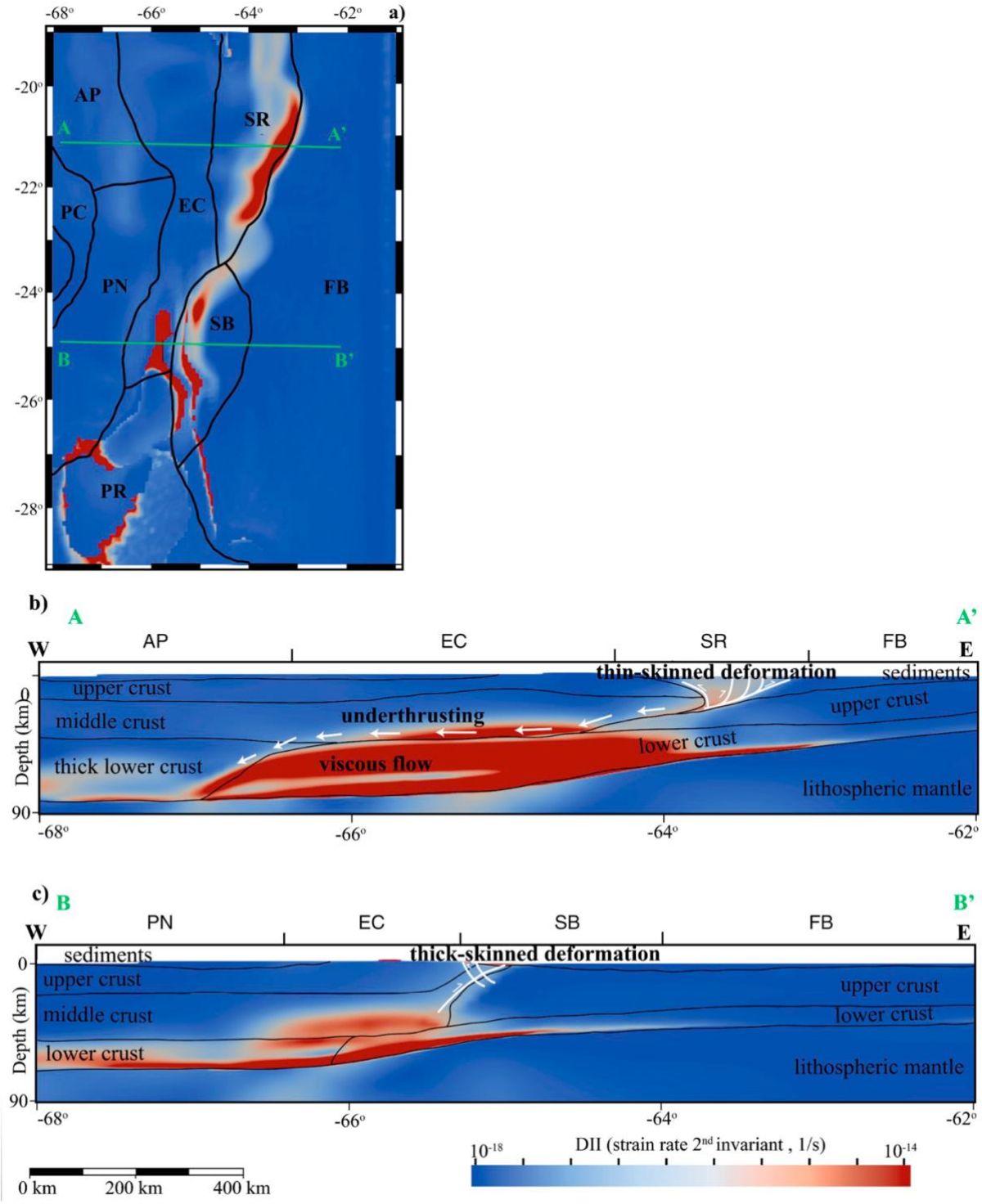

Figure 6.4. Deformation (i.e., the 2nd invariant of the strain rate) field of the geodynamic model after 3.3 km shortening. **a)** Distribution of deformation from top view of the 3D model; **b–c)** two cross-sections A-A' and B-B′, showing the deformation in the Altiplano-Puna plateau and its foreland area. The black lines are boundaries between different materials. AP: Altiplano; PN: Puna, PC: Chilean Precordillera; EC: Eastern Cordillera; SR: Subandean Ranges; SB: Santa Barbara System; PR: Pampean Ranges; FB: Foreland basin.

6.4 Discussion

The results of our geodynamic model considering the crustal structure and composition of the density model by Ibarra et al. (2019) reproduce well the deformation pattern in the foreland region of the Altiplano-Puna plateau (Figure 6.4a). In the Altiplano region, the model predicts underthrusting of the Brazilian shield beneath the plateau and thin-skinned deformation in the Subandean Ranges (Figure 6.4b), whilst to the south, in the Puna region, the model predicts thick-skinned deformation in the Santa Barbara System. In the cross section through the Altiplano, results of the density model show a sharp decrease of the crustal thickness from the Altiplano to the foreland and a thick sedimentary layer (Figure 6.3a). Our results suggest that the strong rheology in the Altiplano (more mafic when compared to the Puna) and the thick sedimentary layer in the north of the foreland favor the underthrusting of the shield.

Furthermore, we observe a spatial correlation between the localization of deformation in the foreland and the strength of the lithosphere, which highly depends on rock composition and the depth of the lithosphere-asthenosphere boundary (LAB). We find that the deformation focusses in the transition from the felsic and weak crust in the orogen to the more mafic and strong crust in the foreland. In addition, the lithosphere-asthenosphere boundary gets shallow from the foreland to the orogen, thus increasing the thermal gradient of the lithosphere and decreasing its strength (Tassara et al., 2006; Prezzi et al., 2009; Koptev & Ershov, 2011; Prezzi et al., 2014). As a result, deformation focusses where the highest gradients of lithospheric strength occur, in the transition from the weaker felsic and hot lithosphere in the plateau to the more mafic and colder strong lithosphere in the foreland.

If the lithospheric strength in the Altiplano-Puna plateau is low due to its thick felsic crust and thin lithosphere, then one may think that tectonic shortening should be accommodated inside the weak plateau. However, our geodynamic model shows that shortening is displaced to the eastern boundary of the Altiplano-Puna. Previous studies on gravitational potential energy have demonstrated that the potential energy of a mountain range grows with the square of the surface elevation and the thickness of the root, thus the forces required to produce deformation of a thickened crust exponentially increase (Molnar & Lyon-Caen, 1988; Stüwe, 2007). In addition, regions with high gravitational potential energy exert a net force on regions with low potential energy (Stüwe, 2007). Considering this, we infer that in addition to the strength of the lithosphere, the gravitational potential energy of the plateau also contributes to the localization

of shortening. The high gravitational potential energy of the plateau (due to its thick crust and high elevation) prevents internal deformation and imposes a stress field forcing lateral growth (in width) instead of vertical growth (e.g., (Molnar & Lyon-Caen, 1988). Consequently, when the plateau grows laterally, the work done by the compressive force will produce thickening of the crust along the edge of the plateau and its foreland.

6.5 Conclusions

The present-day geodynamic model constructed using the density model by Ibarra et al. (2019) reproduces well the observed deformation patterns in the Subandean Ranges and Santa Barbara System. Deformation processes preferably take place in those locations of the orogen-foreland pair, where the highest gradients of lithospheric strength occur.

There is no spatial correlation between the Pampia-Antofalla terrane boundary and either the density of the crust or the location of deformation suggesting that, if present, it does not exert control on deformation.

References

Allmendinger, R. W., & Gubbels, T. (1996). Pure and simple shear plateau uplift, Altiplano-Puna, Argentina and Bolivia. *Tectonophysics*, *259*(1), 1–13. https://doi.org/10.1016/0040-1951(96)00024-8

Assumpção, M., Feng, M., Tassara, A., & Julià, J. (2013). Models of crustal thickness for South America from seismic refraction, receiver functions and surface wave tomography. *Tectonophysics*, *609*, 82–96. https://doi.org/10.1016/j.tecto.2012.11.014

Čermák, V., & Rybach, L. (1982). Thermal conductivity and specific heat of minerals and rocks. In G. Angenheister (Ed.), *Physical properties of rocks. Landolt-Bornstein, New Series* (pp. 305–343). Springer Berlin Heidelberg New York.

Hirth, G., & Kohlstedt, D. (2003). Rheology of the upper mantle and the mantle wedge: A view from the experimentalists. *Washington DC American Geophysical Union Geophysical Monograph Series*, *138*, 83–105. https://doi.org/10.1029/138GM06

Ibarra, F., Liu, S., Meeßen, C., Prezzi, C. B., Bott, J., Scheck-Wenderoth, M., et al. (2019). 3D data-derived lithospheric structure of the Central Andes and its implications for deformation: Insights from gravity and geodynamic modelling. *Tectonophysics*, *766*, 453–468. https://doi.org/10.1016/j.tecto.2019.06.025

Kaus, B. J. P., Popov, A. A., Baumann, T. S., Pusok, A. E., Bauville, A., Fernandez, N., & Collignon, M. (2016). Forward and inverse modelling of lithospheric deformation on geological timescales. *NIC Symposium 2016 - Proceedings*, *48*, 299–307.

Koptev, A. I., & Ershov, A. V. (2011). Thermal thickness of the Earth's lithosphere: a numerical model. *Moscow University Geology Bulletin*, *66*(5), 323–330. https://doi.org/10.3103/S014587521105005X

Liu, S., & Currie, C. A. (2016). Farallon plate dynamics prior to the Laramide orogeny: Numerical models of flat subduction. *Tectonophysics*, *666*, 33–47. https://doi.org/10.1016/j.tecto.2015.10.010

Molnar, P., & Lyon-Caen, H. (1988). Some simple physical aspects of the support, structure, and evolution of mountain belts. *Geological Society of America Special Paper*, *218*, 179–208. https://doi.org/10.1130/SPE218-p179

Oncken, O., Hindle, D., Kley, J., Elger, K., Victor, P., & Schemmann, K. (2006). Deformation of the Central Andean Upper Plate System — Facts, Fiction, and Constraints for Plateau Models. In O. Oncken, G. Chong, G. Franz, P. Giese, H.-J. Götze, V. A. Ramos, et al. (Eds.), *The Andes* (pp. 3–27). Springer Berlin Heidelberg. https://doi.org/10.1007/978-3-540-48684-8_1

Prezzi, C., Iglesia Llanos, M. P., Götze, H. J., & Schmidt, S. (2014). Thermal and geodynamic contributions to the elevation of the Altiplano-Puna plateau. *Physics of the Earth and Planetary Interiors*, *237*, 51–64. https://doi.org/10.1016/j.pepi.2014.10.002

Prezzi, C. B., Götze, H. J., & Schmidt, S. (2009). 3D density model of the Central Andes. *Physics of the Earth and Planetary Interiors*, *177*(3–4), 217–234. https://doi.org/10.1016/j.pepi.2009.09.004

Ramos, V. A. (2008). The Basement of the Central Andes: The Arequipa and Related Terranes. *Annual Review of Earth and Planetary Sciences*, *36*(1), 289–324. https://doi.org/10.1146/annurev.earth.36.031207.124304

Ramos, V. A., Vujovich, G., Martino, R., & Otamendi, J. (2010). Pampia: A large cratonic block missing in the Rodinia supercontinent. *Journal of Geodynamics*, *50*(3–4), 243–255. https://doi.org/10.1016/j.jog.2010.01.019

Ranalli, G., & Murphy, D. C. (1987). Rheological stratification of the lithosphere. *Tectonophysics*, *132*(4), 281–295. https://doi.org/10.1016/0040-1951(87)90348-9

Sobolev, S. V., Babeyko, A. Y., Koulakov, I., & Oncken, O. (2006). Mechanism of the Andean Orogeny: Insight from Numerical Modeling. In O. Oncken, G. Chong, G. Franz, P. Giese, H.-J. Götze, V. A. Ramos, et al. (Eds.), *The Andes* (pp. 513–535). Springer Berlin Heidelberg. https://doi.org/10.1007/978-3-540-48684-8_25

Strecker, M. R., Alonso, R. N., Bookhagen, B., Carrapa, B., Hilley, G. E., Sobel, E. R., & Trauth, M. H. (2007). Tectonics and Climate of the Southern Central Andes. *Annual Review of Earth and Planetary Sciences*, *35*, 747–787.

Stüwe, K. (2007). *Goedynamics of the Lithosphere. An Introduction* (2nd ed.). Springer-Verlag Berlin Heidelberg. https://doi.org/10.1007/978-3-540-71237-4

Tassara, A., Götze, H. J., Schmidt, S., & Hackney, R. (2006). Three-dimensional density model of the Nazca plate and the Andean continental margin. *Journal of Geophysical Research: Solid Earth*, *111*(9), 1–26. https://doi.org/10.1029/2005JB003976

Vilà, M., Fernández, M., & Jiménez-Munt, I. (2010). Radiogenic heat production variability of some common lithological groups and its significance to lithospheric thermal modeling. *Tectonophysics*, *490*(3–4), 152–164. https://doi.org/10.1016/j.tecto.2010.05.003

Wilks, K. R., & Carter, N. L. (1990). Rheology of some continental lower crustal rocks. *Tectonophysics*, *182*(1–2), 57–77. https://doi.org/10.1016/0040-1951(90)90342-6

Chapter 7

Conclusions and future work

7.1 Conclusions

The detailed conclusions are presented at the end of each chapter. Here we summarize only the main points.

1. We have performed high-resolution 2D and 3D thermomechanical models of the orogen-foreland system. The high-resolution models demonstrate that three factors control the foreland-deformation patterns: (i) the strength difference in the upper lithosphere between the orogen and its foreland, rather than the difference in the entire lithospheric strength between them; (ii) gravitational potential energy (GPE) of the orogen that is in turn controlled by its crustal thickness and lithospheric thickness, and (iii) the strength and thickness of the deforming foreland sediments.

2. High resolution 2D models focused on the sections of the Altiplano and Puna in the Central Andes constrained by observed shortening rates (during last 10Myr) and lithospheric structures derived from seismic data reproduce well surface topography and deformation patterns in the Altiplano-Puna foreland. The models also suggest an important role of mantle corner flow below the plateau in defining the shortening mode and the dipping direction of faults at the edge of the foreland.

3. The 3D models of the Altiplano-Puna plateau and its foreland reproduce similar features as high-resolution 2D models and suggest that a higher shortening rate at the Altiplano foreland is related to the mechanically easier simple-shear shortening in presence of thick and mechanically weak sedimentary basins. The lower shortening rate in the Puna foreland implies that a significant part of shortening is likely accommodated by trench retreat.

4. The data-derived lithospheric structures were used as the initial configuration of the geodynamic model to study the formation of foreland-deformation patterns in short term

(few million years) model runs. The geodynamic model reproduces well the observed deformation heterogeneity in the foreland region of the Altiplano-Puna plateau.

7.2 Future work

This work is a systematic study of controls on the foreland-deformation patterns through geodynamic simulations of the orogen-foreland shortening system. However, our models did not consider how the subduction dynamics and other factors (e.g., sediment stratification, phase transition, surface processes) affect deformation processes. Below are some suggested directions for future work on foreland-deformation tectonics.

7.2.1 Influence of sediment stratification on the foreland deformation of the Altiplano-Puna plateau

In the foreland of the Altiplano-Puna plateau between 20°S and 28°S, the sedimentary basin stratifies from top young Tertiary and Upper Cenozoic units to old Mesozoic and Paleozoic units, and the longitudinal stratigraphic section shows an along-strike variation (Allmendinger & Gubbels, 1996; Pearson et al., 2013). In particular, the thickness of Upper Cenozoic units decreases from 5 km at 20-22°S to 1-2 km at 25-27°S. The thick Paleozoic units (i.e., Carboniferous, Devonian/Silurian, and Ordovician/Cambrian sections) pinches out southward. At 23-24°S, the boundary between the Subandean Ranges and the Santa Barbara System, Mesozoic strata of the Salta Rift underlie the thin Cenozoic strata and sit unconformably on a much thinner Siluro-Devonian section. At 26°S, Paleozoic-Mesozoic units disappear, and Cenozoic rocks lie directly on the Sierras Pampeanas basement.

Allmendinger & Gubbels (1996) noticed the striking correlation between the magnitude of shortening and geometries of Paleozoic and Mesozoic sedimentary basins and of Late Cenozoic foreland structures. Pearson et al. (2013) suggest that a wider distribution of Mesozoic rift basins in Bolivia may control the kinematics of shortening within the Altiplano and Eastern Cordillera. In our models, we consider these sedimentary covers as a whole and neglect the stratigraphy. Therefore, it is worth to use high-resolution 2D models inside the sediment cover of the Subandean ranges to test the candidates for the abrupt and strong strength reduction in Late Miocene. In particular, we can test the hypothesis if the hydrocarbon maturation within

the thick layer of the Subandean Paleozoic sediments might have triggered the failure of the foreland.

7.2.2 Orogen-foreland shortening models with western subduction dynamics in the Central Andes

The numerical models of the orogen-foreland compressional system in the Central Andes should be extended by including western subducting Nazca plate below South America plate. While causes of the change of deformation styles were successfully investigated in this thesis, causes of the lateral variation of shortening rates remain unclear. As we suggest in Chapter 5, one possibility is that lower shortening rate in Puna foreland is likely accommodated in the forearc by the slab retreat. To test this hypothesis and investigate other possibilities (e.g., the subduction-induced mantle flow under the plateau discussed in Chapter 4), the subduction is necessary to include in the orogen-foreland model.

Figure 7.1 shows a possible numerical example of such model computed using the code ASPECT. This model includes an oceanic plate (slab), which subducts below the continental plate like it happens in the central Andes. The model geometry is 2640*660 km. The model resolution is 1.28 km from the surface to the 70 km depth (0.64 km high at top 20 km) and 10 km for the rest of the model domain. Such high resolution ensures the precise modeling of crustal-scale and sediment-layer-scale deformation. The model also implements the adaptive mesh refinement with composition and temperature strategy, allowing changing model resolution in the upper mantle. The material has non-linear visco-plastic rheology, and the material properties follow previous subduction models (e.g., Sobolev & Babeyko, 2005; Liu & Currie, 2016) and previous compressional models in the above chapters. In this model, the Nazca oceanic plate subducts under the South America plate due to the imposed driving force that provides a constant convergence rate of 10 cm/yr. After 3.5 Myr, a normal-dip subduction forms, and the intraplate compression process will be started by imposing the shortening from foreland lithosphere at the right-side boundary. The model also shows a mantle flow in the mantle wedge above the slab.

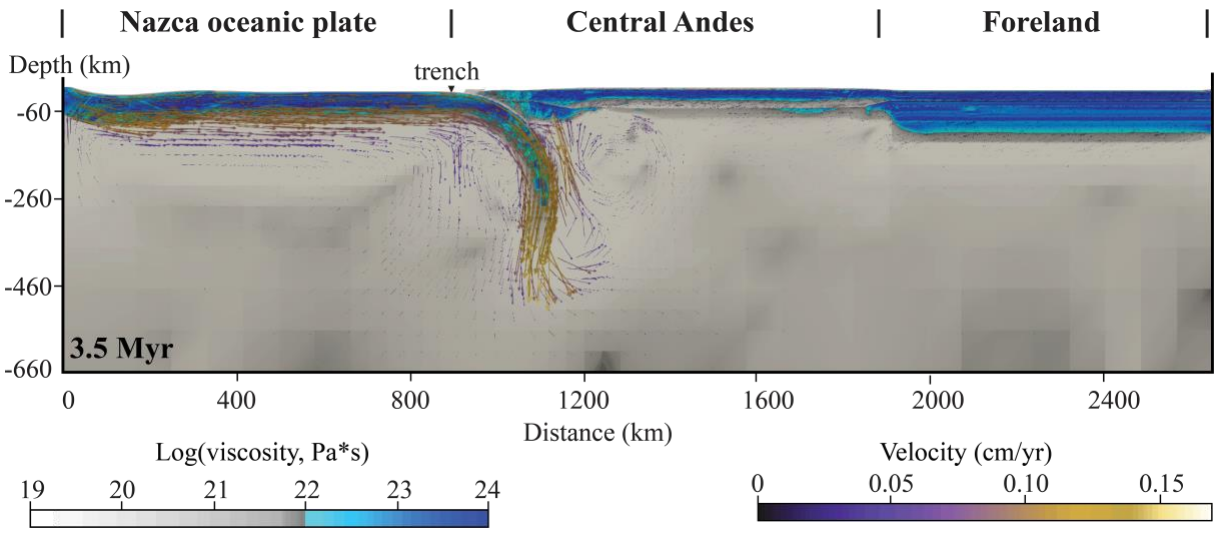

Figure 7.1. A 2D numerical model with the plateau-foreland shortening system and western oceanic plate subduction process after 3.5 Myr. This example applied to the Central Andes case.

7.2.3 Surface processes and phase transition in the geodynamic simulation

As discussed in Chapter 4, the Central Andean models with surface topography constraint produce a first-order fit of the elevation difference between the plateau and its foreland to the observation. However, the model ignores the surface processes (e.g., erosion and sedimentation), and thus show a poorly elevation fit of topography between Eastern Cordillera and Subandean-Santa Barbara system. In practice, the surface processes will smooth the topography possibly improving fit to observations. In the latest version of LaMEM, a surface function has been added to mimic the erosion and sedimentation. A new technique about coupling the advanced surface code FastScapeLib with ASPECT is under development. Both codes can be used to develop the model with surface processes in the future.

The geodynamic simulation should also consider the phase changes in the oceanic crust during subduction as well as in the continental mafic and felsic crusts during compression. In particular, during orogenic shortening, the mafic crust enters the eclogite stability field (generally temperature >600 °C and pressures >1.2 GPa) and may transfer to the dense eclogite, resulted in the process of phase transition (e.g., Babeyko et al., 2006; Sobolev et al., 2006; Wang et al., 2015; Liu & Currie, 2016). In the oceanic crust also occurs basalt-eclogite transformation when it subducts into the mantle (generally at a depth of ~50-70 km) (Hacker et al., 2003). Eclogitization may not immediately happen even when it is within the eclogite stability field (e.g., Austrheim et al., 1997; Leech, 2001; Jackson et al., 2004). The delay of phase

transformation appears to be related to the presence of hydrous fluids (Leech, 2001). If the crust is relatively dry, then the reaction is kinetically delayed, leading to metastability. The resulted density change in the crust can have a significant influence on topography evolution.

7.2.4 Data assimilation function in the geodynamic simulation

Recent progress in numerical modeling techniques allows for developing more realistic 3D geodynamic models with more constraints from geoscientific data. In order to construct the data-oriented model, the data assimilation approach should be implemented in the geodynamic codes. The idea of this approach is the following: a model starting from a poorly constrained initial state becomes progressively better trained using known observations, such that its integration from the remote past to the final state (i.e., present-day) could provide useful insights on the evolution of the relatively recent history of the mantle and surface geology. This approach takes full advantage of the specific constraints from a plate reconstruction. For example, it can incorporate into an evolutionary subduction model temporally and spatially by varying plate motion and slab age, both of which are shown to affect upper-plate deformation (e.g., Lallemand et al., 2005; Capitanio et al., 2011; Liu & Stegman, 2011). The data assimilation function has been successfully implemented into the code CitcomS (Zhong et al., 2008; Hu et al., 2016) and will also be added into ASPECT in near future.

Currently, the assimilation of plate motion from plate reconstruction data in GPlates (www.gplates.org; Gurnis et al., 2012) has been achieved in ASPECT by the developers Rene Gassmöller, Eva Bredow, and Juliane Dannberg. The implementation of the assimilations of the thermal lithosphere from plate age data and of plate boundaries in GPlates is under development. More details can be found at https://github.com/sibiaoliu/aspect.git.

References

Allmendinger, R. W., & Gubbels, T. (1996). Pure and simple shear plateau uplift, Altiplano-Puna, Argentina and Bolivia. *Tectonophysics*, *259*(1), 1–13. https://doi.org/10.1016/0040-1951(96)00024-8

Austrheim, H., Erambert, M., & Engvik, A. K. (1997). Processing of crust in the root of the Caledonian continental collision zone: the role of eclogitization. *Tectonophysics*, *273*(1), 129–153. https://doi.org/10.1016/S0040-1951(96)00291-0

Babeyko, A. Y., Sobolev, S. V., Vietor, T., Oncken, O., & Trumbull, R. B. (2006). Numerical Study of Weakening Processes in the Central Andean Back-Arc. In O. Oncken, G. Chong, G. Franz, P. Giese, H.-J. Götze, V. A. Ramos, et al. (Eds.), *The Andes* (pp. 495–512). Springer Berlin Heidelberg. Retrieved from http://link.springer.com/10.1007/978-3-540-48684-8_24

Capitanio, F. A., Faccenna, C., Zlotnik, S., & Stegman, D. R. (2011). Subduction dynamics and the origin of Andean orogeny and the Bolivian orocline. *Nature*, *480*(7375), 83–86. https://doi.org/10.1038/nature10596

Gurnis, M., Turner, M., Zahirovic, S., DiCaprio, L., Spasojevic, S., Müller, R. D., et al. (2012). Plate tectonic reconstructions with continuously closing plates. *Computers & Geosciences*, *38*(1), 35–42. https://doi.org/10.1016/j.cageo.2011.04.014

Hacker, B. R., Abers, G. A., & Peacock, S. M. (2003). Subduction factory 1. Theoretical mineralogy, densities, seismic wave speeds, and H2O contents. *Journal of Geophysical Research: Solid Earth*, *108*(B1). https://doi.org/10.1029/2001JB001127

Hu, J., Liu, L., Hermosillo, A., & Zhou, Q. (2016). Simulation of late Cenozoic South American flat-slab subduction using geodynamic models with data assimilation. *Earth and Planetary Science Letters*, *438*, 1–13. https://doi.org/10.1016/j.epsl.2016.01.011

Ibarra, F., Liu, S., Meeßen, C., Prezzi, C. B., Bott, J., Scheck-Wenderoth, M., et al. (2019). 3D data-derived lithospheric structure of the Central Andes and its implications for deformation: Insights from gravity and geodynamic modelling. *Tectonophysics*, *766*, 453–468. https://doi.org/10.1016/j.tecto.2019.06.025

Jackson, J. A., Austrheim, H., McKenzie, D., & Priestley, K. (2004). Metastability, mechanical strength, and the support of mountain belts. *Geology*, *32*(7), 625–628. https://doi.org/10.1130/G20397.1

Lallemand, S., Heuret, A., & Boutelier, D. (2005). On the relationships between slab dip, back-arc stress, upper plate absolute motion, and crustal nature in subduction zones. *Geochemistry, Geophysics, Geosystems*, *6*(9). https://doi.org/10.1029/2005GC000917

Leech, M. L. (2001). Arrested orogenic development: eclogitization, delamination, and tectonic collapse. *Earth and Planetary Science Letters*, *185*(1), 149–159. https://doi.org/10.1016/S0012-821X(00)00374-5

Liu, L., & Stegman, D. R. (2011). Segmentation of the Farallon slab. *Earth and Planetary Science Letters*, *311*(1–2), 1–10. https://doi.org/10.1016/j.epsl.2011.09.027

Liu, S., & Currie, C. A. (2016). Farallon plate dynamics prior to the Laramide orogeny: Numerical models of flat subduction. *Tectonophysics*, *666*, 33–47. https://doi.org/10.1016/j.tecto.2015.10.010

Pearson, D. M., Kapp, P., DeCelles, P. G., Reiners, P. W., Gehrels, G. E., Ducea, M. N., & Pullen, A. (2013). Influence of pre-Andean crustal structure on Cenozoic thrust belt kinematics and shortening magnitude: Northwestern Argentina. *Geosphere*, *9*(6), 1766–1782. https://doi.org/10.1130/GES00923.1

Sobolev, S. V., & Babeyko, A. Y. (2005). What drives orogeny in the Andes? *Geology*, *33*(8), 617–620. https://doi.org/10.1130/G21557AR.1

Sobolev, Stephan V., Babeyko, A. Y., Koulakov, I., & Oncken, O. (2006). Mechanism of the Andean Orogeny: Insight from Numerical Modeling. In O. Oncken, G. Chong, G. Franz, P. Giese, H.-J. Götze, V. A. Ramos, et al. (Eds.), *The Andes* (pp. 513–535). Springer Berlin Heidelberg. https://doi.org/10.1007/978-3-540-48684-8_25

Wang, H., Currie, C. A., & DeCelles, P. G. (2015). Hinterland basin formation and gravitational instabilities in the central Andes: Constraints from gravity data and geodynamic models. In *Geological Society of America Memoirs* (Vol. 212, pp. 387–406). Geological Society of America. https://doi.org/10.1130/2015.1212(19)

Zhong, S., McNamara, A., Tan, E., Moresi, L., & Gurnis, M. (2008). A benchmark study on mantle convection in a 3-D spherical shell using CitcomS: BENCHMARKS OF 3-D SPHERICAL CONVECTION MODELS. *Geochemistry, Geophysics, Geosystems*, *9*(10), n/a-n/a. https://doi.org/10.1029/2008GC002048